Unveiling inundations

Inundation mapping in a dynamic, data-scarce environment using Ka-band passive microwave radiometry. Ouémé Delta, Benin.

W.W.J. Neisingh
20-12-2018

TU Delft

Royal HaskoningDHV
Enhancing Society Together

The picture on the cover was taken near Aguégués, Benin during fieldwork in July 2018. It captures the essence of this thesis motivation in showing the role that water plays in Beninese life. Despite the colourfully dressed occupants showing no apparent doubts about the vessel's safety, many would be jeopardised if directly exposed to water. Besides locals basing their knowledge on experience and local tradition, many questions remain about inundations. At the same time these inundations are difficult to analyse due to the typical thick cloud cover.

Master
Thesis

Unveiling inundations

Inundation mapping in a dynamic, data scarce environment using Ka-band passive microwave radiometry and Extreme Value time-series analysis

W.W.J. Neisingh

Student number 4101839

Defense December 20th 2018

Thesis commitee

Prof. dr. ir. N.C. van de Giesen	TU Delft
Prof. dr. ir. S. C. Steele-Dunne	TU Delft
Prof. dr. ir. M. Kok	TU Delft
Ir. M. R. Tonneijck	Royal HaskoningDHV

Synthèse

Une grande partie de la population mondiale vit dans les deltas ou à proximité d'une rivière qui offre de nombreux avantages, tels que l'accès aux transports, à la nourriture et à l'eau potable. L'inondation des plaines inondables est un phénomène naturel et récurrent qui irrigue par exemple des sols fertiles, mais présente des inconvénients lorsque des inondations (graves) affectent les personnes ou les infrastructures. Les pays en développement d'Afrique et d'Asie sont les régions qui connaîtront la plus forte augmentation de l'impact des inondations au cours des prochaines décennies.

Les études conventionnelles sur les risques d'inondation peuvent analyser efficacement les inondations (fluviales), mais exigent des données et des logiciels considérables et parfois complexes, qui ne sont pas toujours disponibles, en particulier dans les régions susmentionnées d'Afrique et d'Asie. De plus, ces études s'appuient sur des données d'écoulement, qui ne sont pas toujours disponibles et deviennent moins précises pour l'écoulement extrême lorsque les rives du fleuve débordent. En outre, même lorsque les données sont disponibles, des procedures longues et bureaucratiques peuvent être necessaires pour obtenir les données. Les données d'élévation sont souvent disponibles seulement à partir de modèles disponibles au public. Par conséquent, il y a un besoin pour une méthode alternative pour analyser des inondations fluviales qui soit plus indépendante et qui utilise des données et des logiciels open source. De plus, cette méthode doit fournir des informations sur une résolution temporelle élevée (quotidienne), car les inondations peuvent changer rapidement. La résolution spatiale doit être aussi élevée que possible, dans les limites de la résolution temporelle.

Cette recherche se concetre sur la détection, l'estimation et la cartographie des inondations dans le delta de l'Oueme (Bénin, Afrique de l'Ouest) afin de obtenir des informations sur l'étendue et le moment des inondations et d'analyser l'évolution de ces inondations au cours de temps à l'aide d'images de télédétection par satellite et de données et logiciels en open source. En outre, il vise à étudier comment les précipitations en amont (causant des inondations fluviales) et la population de la delta de l'Ouémé (soumise aux effets des inondations) se sont développées au cours des dernières décennies pour faire un premier pas dans la direction de l'analyse de l'impact des inondations.

Pour répondre aux questions de recherche, un modèle de cartographie de l'étendue de l'inondation (IEMM) est développé pour détecter les inondations, estimer l'échelle d'inondation et ensuite allouer la fraction d'eau de surface estimée dans une zone d'intérêt (la cellule de la grille de mesure). Premièrement, une méthode de détection d'inondation est développée (CMC-ratio) et testée qui consiste à mettre à l'échelle une cellule de mesure entre une cellule de la grille de calibration (sèche) et une cellule de grille de calibration supplémentaire (humide). Deux-

ièmement, l'estimation de l'échelle d'inondation (CMC-ratio) est validée à l'aide d'images de télédétection optique et améliorée par le développement de diverses méthodes d'estimation à l'échelle. Troisièmement, l'échelle estimée est attribuée en comparant différentes cartes d'altitude (modèle numérique de terrain (MNT): MERIT DEM et HAND) et des méthodes de cartographie. Les résultats de l'IEMM sont comparés à l'écoulement pour obtenir des informations sur le moment des inondations et confirment que l'IEMM fonctionne mieux pour les inondations plus grandes, alors que les mesures de l'écoulement montrent l'inverse. Cela montre qu'en termes d'impact (personnes touchées et décès), l'échelle maximale des inondations a probablement un effet plus important que le nombre de jours d'inondations extrêmes. Le délai est calculé et indique avec quelle vitesse les inondations se propagent dans le delta de la Ouémé.

Les images hyperfréquences passives (c'est à dire micro-ondes) en bande Ka sont disponibles dans le jeu de données MEaSUREs de 1978 à 2017, ce qui permet des comparaisons pluriannuelles et multi-systèmes pour analyser le comportement des inondations au cours de temps. Cependant, dans la pratique, les variations du capteur, par example la bande passante, de l'angle d'incidence et de la sensibilité du capteur entraînent des modifications qui doivent être prises en compte pour l'analyse de série chronologique intersystème.

L'analyse des précipitations quotidienne dans les des stations situées dans les bassins versants moyen et supérieur d'Oueme montre une tendance à la baisse des précipitations extrêmes, compatible avec des observations en le region entière d'Afrique de l'Ouest.Fondé sur des catastrophes signalées et de la croissance démographique, un lien est suggéré entre les zones peuplées et l'impact en termes de personnes affectées et de décès causés par les inondations fluviales. En particulier, cela indique des zones urbanisées au sud du delta de la Ouémé, telles que So-Ava et Aguegues.

Ceci on amène à la conclusion qu'avec la méthode actuelle, il est effectivement possible de déployer la télédétection par satellite optique et passive par micro-ondes pour détecter les inondations, estimer l'échelle, qui peut ensuite être cartographiée dans un modèle d'altitude pour déterminer l'étendue de l'inondation. Cependant, une meilleure compréhension des effets de réduction d'échelle, de la végétation et du contenu en eau de surface est nécessaire. Pour le moment, il est donc recommandé d'utiliser la méthode d'échelle Hybride d'inondation, qui utilise une température de luminosité de calibration artificielle humide basée sur le ingénierie inverse à partir d'imagerie optique. De plus, des recommandations sur l'utilisation de méthodes de validation supplémentaires devraient être incluses dans les recherches futures. La population présente dans les zones exposées aux inondations a un impact plus important sur l'impact des inondations que la simple survenue d'inondations. Compte tenu de la croissance démographique attendue au Bénin, il est recommandé d'examiner supplémentaire comment cette évolution se développera à l'avenir.

Abstract

A large part of the world population lives in deltas or in the vicinity of a river which provides many advantages, such as access to transportation, food and drinking water. Inundating floodplains are a natural and recurring phenomenon which is for instance a way to irrigate soils, but drawbacks occur when people or infrastructure are harmed by (extreme) inundations. Developing countries in Africa and Asia are the regions expected to experience the largest increase in impact of inundations in the coming decades.

Conventional flood risk studies can effectively analyse (fluvial) inundations, but require considerable and sometimes complex data and software, which is not always available, in particular in the aforementioned regions in Africa and Asia. Additionally, these studies often rely on discharge data, which is not always available and becomes less accurate for extreme discharge when the river banks overflow. Furthermore, even when data is available, this might only be granted after long, bureaucratic procedures. Elevation data is available from publicly available models, but the horizontal and vertical resolution often does not suffice. Therefore, there is a need for an alternative method to analyse fluvial inundations that is more independent and uses open source data and software. Moreover this method needs to provide information on a high temporal resolution (daily) because of the dynamic behaviour of inundations. The spatial resolution should be as high as possible, given the limitations of temporal resolution.

This research focuses on detecting, estimating and mapping inundations in the Ouémé delta (Benin, West-Africa) to retrieve information about extent and timing of inundations and analyse how inundations developed over time by means of satellite remote sensing imagery and open source data and software. Furthermore, it aims to investigate how upstream precipitation (causing fluvial inundations) and population in the Ouémé delta (subjected to the effects of inundations) developed over the past decades to make a first step towards analysing the impact of inundations.

To answer the research questions an Inundation Extent Mapping Model (IEMM) is developed to detect inundations, estimate the inundation scale and subsequently allocate the estimated surface water fraction in an area of interest (the measurement cell). First an inundation detection method is developed and tested (CMC-ratio), which relies on scaling a measurement cell between a (dry) calibration cell and an additional (wet) calibration cell. Second, the inundation scale estimate

of the CMC-ratio is validated with MODIS optical remote sensing imagery and improved by developing and testing various scale estimation methods. Third, the estimated scale is allocated by comparing different elevation maps (MERIT DEM and HAND) and mapping methods. The outcome of the IEMM is compared to discharge to obtain information about timing of inundations and confirms that the IEMM is increasingly sensitive to larger inundations whereas discharge measurements are reported to show the opposite. This shows that in terms of impact (i.e. affected people and deaths), the maximum extent of inundations likely has a larger effect than number of days of extreme inundations. The lead time is derived showing the speed at which inundations propagate through the Ouémé delta. Ka-band passive microwave imagery is available in the MEaSUREs dataset from 1978 - 2017, which enables multi-annual and multi-system comparisons to analyse inundation behaviour over time. In practice, however, variations in bandwidth, incidence angle, sensor sensitivity cause changes that need to be accounted for when conducting inter-system time series analysis. Precipitation analysis of daily rainfall of rainfall stations in the middle and upper Ouémé catchment show a decreasing trend in extreme rainfall, in line with the trend across West-Africa. Based on reported disasters and population growth a link is suggested between populated zones and impact in terms of affected people and deaths caused by fluvial inundations. In particular this sheds light on urbanized zones in the South of the Ouémé delta, such as Sô-Ava and Aguégués.

This leads to the conclusion that with the current method it is indeed possible to deploy optical and passive microwave remote sensing to detect inundations, estimate the scale, which can subsequently be mapped to an elevation model to find an inundation extent. However, improved understanding of downscaling and re-gridding effects, vegetation and surface water content is required. For now, the Hybrid inundation scale method is therefore recommended, which uses an artificial wet calibration brightness temperature based on reverse engineering from optical imagery. Furthermore, recommendations to use additional validation methods should be included in further research. Population present in inundation prone areas has a larger effect on the impact of inundations than the mere occurrence of inundations. Considering the expected population growth in Benin, it is recommended to further investigate how this will develop in the future.

Preface

This thesis forms the final step of my Master Watermanagement at Delft University of Technology. Although Watermanagement is the official title, frankly I was quite close to choosing Hydraulic Engineering. I think this twofold interest is still very much visible in the topic of my thesis.

The motivation for this research is in line with in a broader global trend of using open source data and software to enable a larger impact. Despite the advanced technologies available nowadays and the numerous studies and models delivered about floods and inundations, the countries where the impact of these inundations is expected to increase the most do only partially benefit from these developments, due to a discrepancy between the required and available technological, financial and human resources.

Satellite imagery is one of the technologies which is increasingly available for public use. For instance, NASA granted public access of the Landsat series in 2009, which caused various other satellite missions and agencies to follow. Recent developments such as the Google Earth Engine can be seen in line with this development. Passive microwave radiometry forms the backbone of this study and although it was never particularly developed to study inundations, forms a very valuable source of information. Especially the Ka-band imagery which has been part of satellite missions for the past 40 years and benefits from the nearly daily overpasses and its cloud-free properties turned out to be an excellent source of information.

I am very glad that the research yielded in interesting results that directly contribute to topical challenges, both in technical as well as social terms. More importantly than the results, I have really enjoyed the process and I am thankful for the support that I received from people in every stage of this thesis. I find it astonishing to see how much I have learned over the course of the past months, both personally and professionally.

Starting at the same point where this research commenced exactly a year, I would like to thank Michel Tonneijck for the freedom and support I have received from him and Royal HaskoningDHV for the opportunity to work on this project which even provided me the chance to visit Benin. I have felt privileged throughout the entire process and I genuinely hope the project can benefit in

from the insights that we gained with this research.

I am sincerely thankful for the TU Delft supervisors Susan Steele-Dunne, Nick van de Giesen and Matthijs Kok whom formed a superb team of and helped me with their abundance of knowledge and expertise, which was very inspiring, and made me look more critical at my own work. Besides, Susan has been a great daily supervisor, with spot-on, constructive and humorous remarks, at first bamboozling me with the overwhelming amount of terms, theories and concepts on remote sensing, that later on I made myself acquainted with.

Having visited the Ouémé delta in Benin helped to put the project in perspective, but also enabled building a network with local scientists whom I hope may benefit from this research. Especially Rita Houngue (whom I got introduced to by Hans van der Kwast) and Gildas Guidigan have been great research partners and got us to interview locals in Fon, the native language. Félicien Badou and Jean Hounkpè have provided me with discharge data from the Bonou station, which turned out to be crucial in later stages of the research. Mama Daouda and Blaise Houenoukpo supported me by all means to submerge in UAC, INE and the Beninese academic life in general. Marc van Liere and Grégoire helped me with more local contacts. The team of DG-Eau and SAP provided me to present and improve the research objectives.

By reaching out I also got in contact with Hessel Winsemius, who officially was not my supervisor, but could have been considering his continuous enthusiasm and support, among others by introducing me to an inspiring group of researchers at Deltares and IHE working on similar concepts.

Compared to other Masters I have always cherished the freedom that we as students Watermanagement have and I am aware that this is a privilege for TU Delft standards, which I hope will stay for a long time to come. Studying together in 4.84 is one of these privileges from Watermanagement that I am thankful for. Not only because it comforts knowing that you can share practical or content related questions, but above all because the of the positive vibe of being surrounded by students being in the same boat. I am convinced it fosters our academic development and makes each of our research stronger.

Wouter Neisingh
Delft, December 2018

Contents

List of Figures

Nomenclature

0.1 Glossary

Flood

The process of overflowing of water onto land that is normally not covered by water. Floods can be caused by (a combination of) rainfall, fluvial discharge or tidal processes. Floods can transform into inundations if they stay in place for a longer time.

Impact

Commonly refers to the product of probability and the consequences of the flood. In this research impact refers to the term used by the International Emergency Database (EM-DAT) and relates to total number of affected people and deaths caused by fluvial inundations.

Inundation

The process of (sometimes intentionally) rising and spreading of water over land usually normally not covered by water, both referring to the act of inundating as well as the state of being submerged in water. This research distinguishes inundation from floods, because of the long time scales (seasonal behaviour) and (to a certain extent) the intentional nature. This research studies fluvial (originating from a river), but not pluvial inundation (originating from direct precipitation).

Mapping

The process of making a map, in this research refers to allocating a surface water fraction by filling an elevation map till a given level. This research distinguishes 'coordinates' and 'seed' mapping. The former is based on filling a contiguous water-body from a given certain location within the area of interest till a given water level. The 'seed' mapping method also allocates water till a certain water level, but lacks the contiguity constraint.

Ka-Band

Microwave band with a frequency range of 26.5 - 40 GHz and a wavelength range of 5.0 - 11.3 mm. The passive microwave sensors used in this research are interchangeably referred to by their frequency (usually 36.5 - 37 GHz) or their band.

0.2 Acronyms

AMSR2	Advanced Microwave Scanning Radiometer 2
AMSR-E	Advanced Microwave Scanning Radiometer - Earth Observing System
ANPC	L'Agence Nationale de Protection Civile de la République du Bénin
CETB	Calibrated Passive Microwave Daily EASE-Grid 2.0 Brightness Temperature
CMC-ratio	Calibration - Measurement - Calibration - ratio
CM-ratio	Calibration - Measurement - ratio
DEM	Digital Elevation Model
DG-Eau	Direction Générale de l'Eau (Water Directory)
DMSP	Defense Meteorological Satellite Program
EASE-Grid 2.0	Equal-Area Scalable Earth Grid Version 2.0
EM-DAT	The International Emergency Database
ESA	European Space Agency
GCOM-W1	Global Change Observation Mission - Water Satellite 1
GFRM	Global Flood Risk Model
GRD	(Drop-in-the-bucket) Gridding Method
HAND	Height Above Nearest Drainage
ICESat	Ice, Cloud and land Elevation Satellite
IEMM	Inundation Extent Mapping Method
INE	Institut National de l'Eau (National Water Institute)
JAXA	Japan Aerospace Exploration Agency
MEaSUREs	Making Earth System Data Records for Use in Research Environments
MERIT DEM	Multi-Error-Removed Improved-Terrain Digital Elevation Model
MNDWI	Modified Normalized Difference Water Index
MODIS	Moderate Resolution Imaging Spectroradiometer
NASA	National Aeronautics and Space Administration
NCDC	National Climate Data Center
NDMI	Normalized Difference Moisture Index
NDWI	Normalized Difference Water Index
NOAA	National Oceanic and Atmospheric Administration
NNDC CDO	NOAA National Data Center, Climate Data Online
NSIDC	National Snow and Ice Data Center
ODK	Open Data Kit
PDF	Probability Distribution Function
SAP	Système d'Alerte Précoce (Flood Early Warning System)
SIR	Scatterometer Image Reconstruction
SNV	Stichting Nederlandse Vrijwilligers (Netherlands Development Organisation)
SSM/I	Special Sensor Microwave Imager
SSMIS	Special Sensor Microwave Imager/Sounder
SSMR	Scanning Multi-channel Microwave Radiometer
UAC	Université d'Abomey Calavi (University of Abomey Calavi)
NIR	Near-infrared
SWIR	Short-wave infrared

0.3 Symbols

T_B	[K]	Brightness Temperature
T_{B_C}	[K]	Brightness Temperature - Calibration cell
$T_{B_{CD}}$	[K]	Brightness Temperature - Dry calibration cell
T_{B_M}	[K]	Brightness Temperature - Measurement cell
$T_{B_{CW}}$	[K]	Brightness Temperature - Wet calibration cell
r_{CMC}	[-]	CMC-ratio
r_{CM}	[-]	CM-ratio
Q	[m^3/s]	Discharge
HR_{CM}	[-]	Discharge estimator (same as CM-ratio)
ϵ_r''	[-]	Electric permittivity - Imaginary part
ϵ_r'	[-]	Electric permittivity - Real part
ϵ_0	[-]	Electric permittivity in vacuum
ϵ	[-]	Emissivity
f, v	[Hz]	Frequency
θ	[deg]	Incidence angle
LST	[K]	Land Surface Temperature
μ	[-]	Mean
δ	[m]	Penetration depth
P	[-]	Population
P	[mm]	Precipitation
B_v	[W m^{-2} sr^{-1} $Hz{-}1$]	Spectral radiance of a body (Planck Function)
c	[m/s]	Speed of light in vacuum
σ	[-]	Standard deviation
σ, κ	[W $m^{-2}K^{-4}$]	Stefan-Boltzmann constant
T	[K]	Temperature
λ	[m]	Wavelength

Introduction 1

A large part of the world population lives in deltas or in the vicinity of a river which provides many advantages, such as access to transportation, food and drinking water. Inundation of floodplains is a natural and recurring phenomenon which is for instance a way to irrigate soils, but drawbacks occur when people or infrastructure are harmed by (extreme) inundations. Floods and inundations globally cause severe economic damage and human losses: an estimated 2,3 billion people were affected by flood inundations between 1995 and 2015, with a record 157.000 loss of lives and estimated minimum economic losses worth $ 662 billion (Wahlstrom and Guha-Sapir, 2015, Kabenge et al., 2017). Nowadays over 50 % of the world population lives within 3 km of a surface water body, making fluvial inundations in deltas particularly important due to population density and economic activity in these regions (Kummu et al., 2011).

1.1 Conventional Flood Risk studies

Although flood risk studies have proven to be very useful in some of these areas, studies are data intensive and often require proprietary software. Even publicly available global flood risk models (GFRM's) face similar limitations (Ward et al., 2015). Especially in data scarce environments of Africa and Asia the impact of inundations is expected to increase, where these flood risk models face limited feasibility (Wahlstrom and Guha-Sapir, 2015). For instance, conventional flood risk studies tend to focus on estimating the water depths, which requires (at least) discharge and elevation data. The former is not always available and can be subject to data gaps and (bureaucratic) authorisation procedures. The latter is available in various global open source models, but lacks the required vertical accuracy to be effectively deployed in deltas, where elevation changes are small, thus making vertical resolution critical. Fluvial inundation is normally related to extreme discharge and over-bank flow, which from an impact and disaster perspective is the most important (discharge) regime, but true discharge rates in this regime are difficult to estimate due to limited calibration data. Despite these limitations, decision-making often still relies on hydrological and hydraulic studies, and is impeded by the lack of such studies. Even if such a study is delivered, the legacy of a project can be smaller than expected, since after completion local authorities and institutions do not have the means to carry on the process. Therefore, there is a need to increase knowledge about (fluvial) inundations as conventional models do not meet the requirements to be applied in data-scarce environments due to the lack of required data and software and the mismatch between the conventional approach and the applicability in local systems.

1.2 Optical and Passive Microwave remote sensing

Over the past decades, satellite remote sensing has become increasingly important amongst Integrated Water Resource Management (IWRM). Flood and inundation management in particular have benefited from the increased availability and accessibility of remote sensing data, the improved spatial and temporal resolution, improved software and the trend towards publicly available data and software (Lakshmi, 2017; Cazenave et al., 2016; Shang, 2017; Aggarwal et al., 2009; Al-Tahir et al., 2014). Remote sensing serves as a relatively independent source of information to produce consistent and coherent datasets. In some cases daily data since the 1970's is available, enabling relatively high (temporal and spatial) resolution analyses and time series analyses. However, developing regions can only benefit to a certain degree from this development, as remote sensing is often used as a secondary source to validate existing models (Marx, 2004). Despite its potential, remote sensing is rarely used as a primary data source for the analysis and decision-making in IWRM projects. Since satellite remote sensing fulfils the requirements to provide daily data on fluvial inundation detection, this research aims to deploy satellite remote sensing to study fluvial inundation characteristics. Two types of satellite remote sensing are particularly relevant: optical and passive microwave imagery.

Optical imagery consists of sensors capturing the (near) visible spectrum and can detect surface water by means of several water retrieval indices, such as NDWI, MNDWI and NDMI, and is available on relatively high spatial (10-30 m) and temporal resolutions (0.5-1 daily). The predominant disadvantage is the noise caused by cloud cover and cloud shadows, which has a significant impact in regions like the tropics. Optical missions include the Landsat series (NASA), Aqua and Terra (NASA) and Sentinel 2 (ESA).

Passive microwave radiometers capture the energy from the microwave domain of the electromagnetic spectrum, expressed as brightness temperature (T_B). Previous research has shown satisfactory results for surface water detection with Ka-band (36.5 - 37.0 GHz; descending node) passive microwave radiometers (Brakenridge et al., 2007; Ticehurst et al., 2009), which is available since 1978 on a (near) daily basis. The satellites providing this data are (ordered by agencies; sensors, respectively): Nimbus-7 (NASA; SMMR), DMSP F08-F18 (NASA; SSM/I, SSMIS), Aqua (NASA; AMSR-E), GCOM-W1 (JAXA; AMSR2), SMAP (NASA; SMAP) and SMOS (ESA; MIRAS). A major disadvantage of this type of imagery is the low spatial resolution (order of magnitude of 10 x 10 km), hence visual interpretation and inundation extent analysis are only possible with sub-pixel analysis.

1.3 CM - Ratio

Inundation detection by means of passive microwave radiometry was presented in previous research conducted by Brakenridge and commonly referred to as the CM-ratio (Brakenridge et al., 2007). This method uses Ka-band radiometry (36,5 GHz AMSR-E, horizontal polarised on the descending node), to analyse the ratio of brightness temperature originating from a measurement area (T_{B_M}) and a calibration target area ($T_{B_{CD}}$), which is included to account for

daily and seasonal variation in the measurement area. The resulting CM-ratio is used to compare normalized brightness temperature with discharge from gauging stations nearby. Despite the good results, there are two shortcomings of the CM-ratio. First, it aims to mimic discharge patterns, but does not explicitly distinguish the differences between inundation extent and discharge. Second, the CM-ratio shows an inundation pattern, but is difficult to interpret in order to retrieve the inundation extent for instance. Hence there is a need to adapt the CM-ratio in a way that it can be interpreted spatially and that the inundation pattern is deliberately distinguished from discharge patterns.

1.4 Inundations in Benin

Benin (West-Africa) is an example of a developing country experiencing recurring inundations. In 2010, vast parts of the Ouémé delta were inundated as a result of heavy precipitation upstream and subsequent high discharges from the Ouémé river, causing the largest fluvial inundations since 1963 (IFRC, 2013; Smith, 2010). This research focuses on fluvial inundations, naturally distinguished from pluvial inundations due to the dominant African Monsoon (Bourles et al., 2007). Approximately 70 % of Benin is part of the Ouémé catchment, hence extreme events and disasters in this catchment have a substantial impact on the country in terms of disturbed livelihoods (IRIN, 2008), public health (Du et al., 2010), disrupted infrastructure (Ouikotan et al., 2017) and food security and prices (Hounkpè et al., 2016). The Ouémé delta has experienced strong population growth over the past decades and predictions on future population growth tend to show an increase in population exposed to fluvial inundations. However, like many developing countries, Benin is lacking the required technical, financial and human resources to conduct a comprehensive flood risk analysis.

Hence, little is known about the exact flood risk in the Ouémé delta. Research by Hounkpè et al. (2015a) does not draw a unequivocal conclusion on the shifting trend in flood frequency over the past years, but this is only analysed for the middle and northern catchment. Research on the more densely populated Ouémé delta is difficult due to the lack of long time series of discharge and the lack of high resolution elevation data. The latter is also problematic for ongoing studies, such as research on hydrodynamic models for the Ouémé delta by Houngue. The government's Flood Early Warning System (SAP) relies on discharge data, which still requires a laborious procedure to operate. The exact locations that are exposed to inundations belonging to the corresponding discharge rate are only known empirically.

Cloud cover dominates the region, like many places near the equator, especially during the inundation season, making optical imagery less suited for inundation analysis. Furthermore, despite (previous) international studies, such as AMMA-Catch (French), IMPETUS (German) and OmiDelta (Dutch), government officials and organisations are reluctant about data sharing (e.g. discharge data), often impeding the spread of knowledge on inundation management. Therefore there is a need to obtain information independently.

1.5 Research objective

The purpose of this study is to investigate an alternative method of inundation mapping in data-scarce environments by developing an inundation extent mapping model (IEMM), which will be tested and applied in the Ouémé delta, Benin. Various methods for using (optical and passive microwave) satellite remote sensing data will be explored, but passive microwave imagery forms the backbone of the data collection. Interviewing over 40 locals and experts indicated a need for improved understanding of timing and extent of inundations, which therefore will be the main focus of the IEMM. The model requires a high temporal resolution to capture the dynamic inundation behaviour, hence daily monitoring is recommended. The spatial resolution needs to be as high as possible, within the possibilities of given temporal resolution. By studying long term behaviour, trends in inundations can be investigated and compared to related processes, such as precipitation and population growth. The outcome aims to support various stakeholders, such as researchers, government officials and IWRM decision-making parties. The potential impact of the study is increased by developing the IEMM in collaboration with local inhabitants and experts, using open source data and software and making the model complementary to conventional flood risk studies. This results in the following research question:

How can optical and passive microwave satellite remote sensing be used for fluvial inundation mapping in data scarce environments like the Ouémé Delta, Benin?

The following sub-questions aim to make answering the research question more tangible.

- *How can fluvial inundations be detected by means of optical and passive microwave imagery in the Ouémé delta, Benin?*
  A seemingly self-explanatory, but important question: the applicability is dependent on local circumstances (e.g. cloud cover, inundation scale) and satellite characteristics (e.g. revisit time, spatial resolution) which need to be well understood before developing an Inundation Extent Mapping Model (IEMM).

- *How can the inundation extent be derived from the inundation detection method?*
  An important step in inundation mapping is to obtain an estimate for the size of inundation and subsequently allocate it to a designated area accordingly. This research aims to do so by solely relying on publicly available remote sensing imagery and elevation data. Generating information about the inundation extent also directly contributes to the needs of locals and experts.

- *How can information about timing of fluvial inundations be derived from the inundation detection method?*
  Timing was also explicitly indicated as an important objective, hence the IEMM focuses on generating timing related outputs, such as start and duration of inundation and lead time of inundation between different regions.

- *Can trends in extreme inundation patterns be observed by multi-annual, multi-system time series analysis?*
  By applying time series analysis of several satellite missions, long-term inundation trends can be studied.

- *How do precipitation and population growth relate to the impact of fluvial inundations in the Ouémé delta?*
  A first attempt to understand the cause of inundations leads to studying precipitation patterns of the middle and upper Ouémé catchment. Upstream precipitation is namely supposed to be responsible for downstream fluvial inundations and subsequent trends could be used to explain fluvial inundation behaviour. The 'impact' of inundations, in terms of affected people and deaths, is supposedly related to the population present in inundation prone areas. Therefore, population growth and registered disasters over time are used to investigate the reported and future impact.

1.6 Reading guide

For the readers who are less familiar with Benin and the Ouémé catchment, Chapter 2 provides a concise description of the study area. Likewise, for the readers less acquainted with remote sensing and (passive) microwave imagery in particular, Chapter 3 provides the required information which is used extensively throughout the rest of the report. Appendix B can be consulted for more specific background on this matter. In Chapter 4, the methods and approach of the research are discussed, comprising an overview of the research structure, a list of the used data and an explanation on the way the Inundation Extent Mapping Model (IEMM) is composed. Furthermore, Appendix C gives an impression of the fieldwork, which was part this research and contributed in defining the objectives for the IEMM. Chapter 5 presents the most important outcomes of this research. Appendices about the CMC-ratio (D), the accounting factors, such as precipitation (**??**) and the 'impact' of inundations (F). The evaluation of the results is presented in Chapter 6 and conclusions and recommendations for further research are presented in Chapter 7.

2 Benin and the Ouémé catchment

The following sections present general information about Benin and the Ouémé River (Section 2.1) and more specifically about past inundations in the Ouémé catchment (Section 2.2). More spatial information on flood prone areas in Benin and the 2010 inundations can be found in Appendix A.

2.1 General information

Benin is a small West-African country (112.622 km^2), bordering Nigeria (809 km), Togo (651 km), Burkina Faso (386 km) and Niger (277 km). It has a narrow coastline in the south (121 km). The total population count is 11 million people, many of whom living in the urban agglomeration in the South, of which the three most important cities are Cotonou (685.000), Porto-Novo (285.000) and Abomey-Calavi (928.000) (The Central Intelligence Agency, 2018). Figure 2.1 depicts a schematic representation of Benin, the Ouémé catchment and the Ouémé delta. A large part of the research is based on the inundations near Bonou, where the only discharge dataset for this research is available.

2.1.1 The Oueme River

The Ouémé catchment is the largest (50.000 km^2) and most important of six catchments located in Benin and partially in Togo (West of Benin) and Nigeria (East of Benin) (Figure 2.1). The Ouémé river is about 500 km long, typically rain-fed, has strongly varying discharges ($Q_{mean} = 170m^3$, $Q_{max} = 1175m^3$ - $Q_{min} = 0m^3$). The Lower Ouémé is characterized by delta-like features, with little elevation, wetlands and lagoons. The aforementioned urban agglomeration is located in this delta, built adjacent to the lagoon (Lake Nokoué). The primary wet season (April - July) generally causes pluvial inundations in the urban areas, whereas the second wet season causes fluvial inundations in the entire delta (September - November). This research focuses primarily on the recurring fluvial inundations, which have a large impact on the society in terms of public health, safety and economical damage (Du et al., 2010; Hounkpè et al., 2015b; IRIN, 2008; Ouikotan et al., 2017).

2.1.2 Climate

The climate is predominantly tropical, hot and humid, except for Northern Benin, which has a semiarid climate. The Ouémé catchment can be subdivided into three rainfall regimes: (1) the uni-modal rainfall regime in North Ouémé comprising two seasons, i.e., the rainy season from May to October, and the dry and hot season; (2) the bimodal rainfall regime in South Ouémé comprising two wet seasons, i.e., a long season between March and July and a short season

between September and mid-November, and a long dry season between November and March; and (3) the transitional rainfall regime in Central Ouémé comprising a rainy season between March and October, with or without a short dry season in August (Hounkpè et al., 2015a). The rain mostly originates from the Guinean Coast. The average annual precipitation varies between 960 mm in the north and 1340 mm in the south. Thus, the rainfall decreases northward and results in a strong natural vegetation gradient (Hounkpè et al., 2015a). Important to note for this research is that inundations in the delta are usually not caused by local heavy rainfall (i.e. pluvial inundations), but merely by excessive river discharge.

2.1.3 Economy

Benin's economy is relatively underdeveloped and dependent on subsistence agriculture and cotton. The GDP is $ 2.200 (The Central Intelligence Agency, 2018). The main export partners are Bangladesh, India, Ukraine, Niger, China, Nigeria and Turkey. The main import partners are Thailand, India, France, China, Togo, the Netherlands and Belgium. Although 86 % of the population has a cellphone subscription, only 12 % of the population has access the slow state-owned internet, which is a burdain for efficient digital communication (The Central Intelligence Agency, 2018).

2.1.4 Population

A significant population growth has taken place over the past decades (Figure 2.5). An urban agglomeration developed encircling lake Nokoué, causing a larger number of people to reside in inundation prone areas. The towns Sô-Ava and Aguégués are two examples of towns that have been hit repeatedly by past inundations. The urbanization rate (3,89 %) is outgrowing the population growth grate (2,71 %), indicating a net internal migration towards the (southern) cities. (The Central Intelligence Agency, 2018). Nevertheless, Benin is politically stable and different religions peacefully coexist (48,5 % Christian, 27,7 % Muslim, 14,2 % Voudoun or other traditional religions)(The Central Intelligence Agency, 2018). Demographically Benin is characterized by a youthful age structure; almost 65 % of the population is under the age of 25 and the life expectancy is only 62,3 years (Figure 2.2)(The Central Intelligence Agency, 2018). The high fertility rate (4,8 children per woman in 2016) is in part due to the low contraceptive use (17,9 %). 40 % of the population lives below the poverty line (The Central Intelligence Agency, 2018). A large part of the population has no access to improved drinking water or sanitation facilities (22,1 % and 80,3 %, respectively), even in urban areas (14,8 % and 64,4 %, respectively)(The Central Intelligence Agency, 2018).

2.1.5 Governance

Benin is governed as a presidential republic since 1990 and has been politically stable over the past years. Under the current president, Patrice Talon (since 2016), the action plan "Bénin Révélé" (2016-2021) has been launched, aiming to implement 45 high priority projects in 9 sectors, of which several are related to delta planning. The organizational structure of water related activities is weak and intertwined. The most important organisations for this study are listed in figure 2.3.

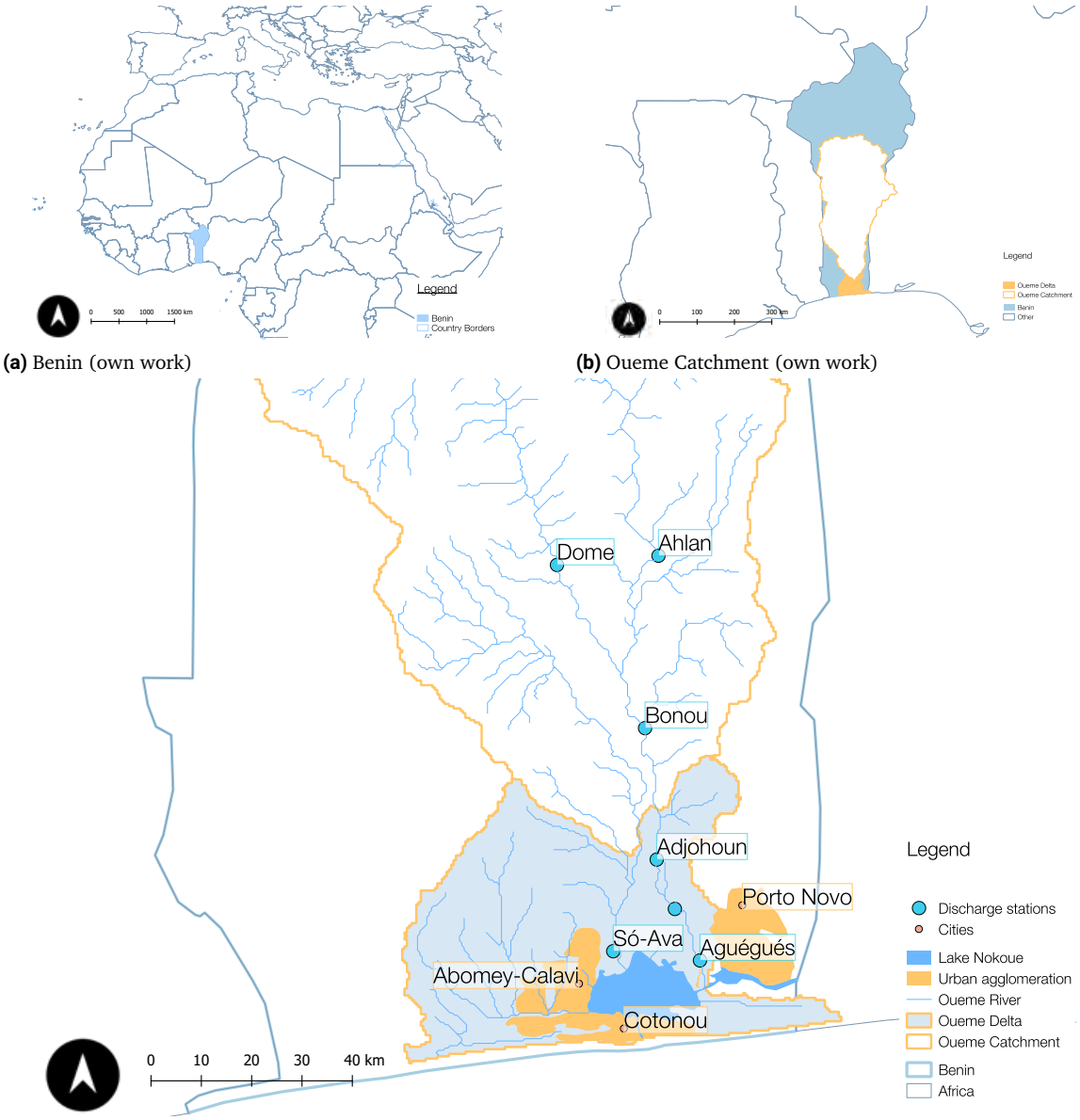

(a) Benin (own work)

(b) Oueme Catchment (own work)

(c) Oueme Delta (own work)

Figure 2.1. Schematisation of Benin, the Ouémé catchment and the points of interest in the Ouémé delta. Sô-Ava and Aguégués are both discharge location as well as urban areas. The urban areas are built around lake Nokoué (which is actually a lagoon), marked blue in the center (own work).

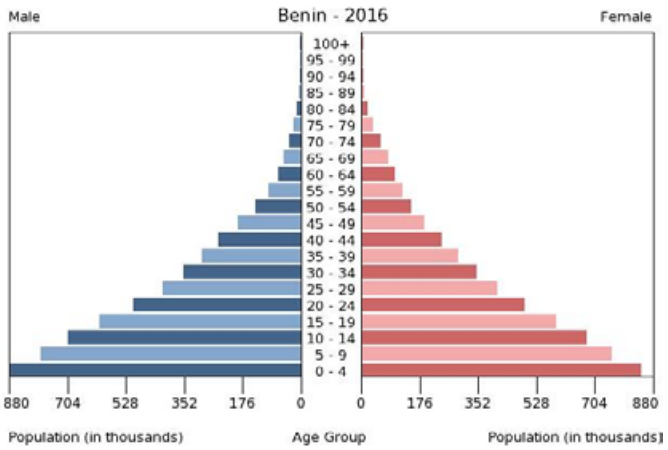

Figure 2.2. Population pyramid of Bénin

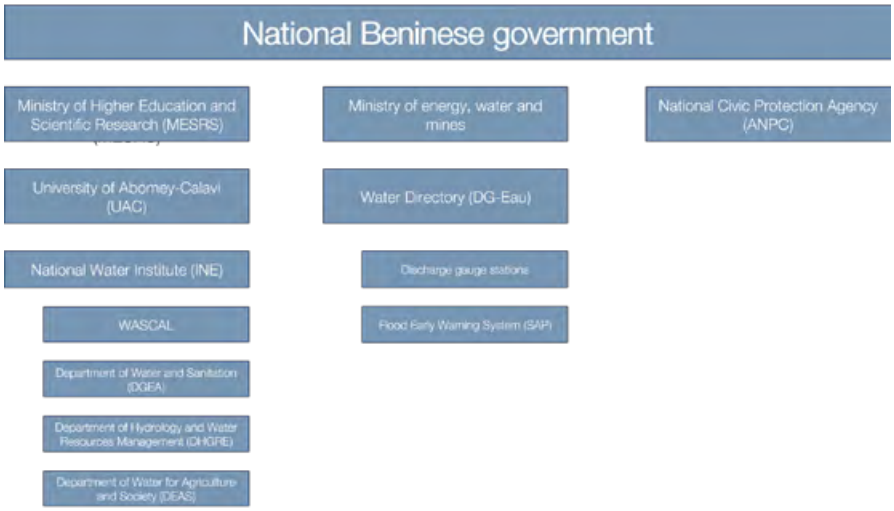

Figure 2.3. Overview of stakeholders in Benin relevant for inundation research (own work)

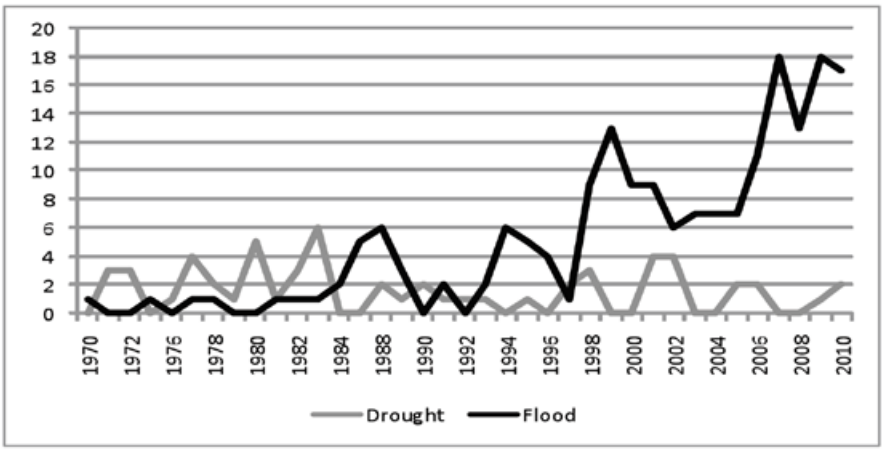

Figure 2.4. Registered flood and drought disasters in West-Africa 1970 - 2010 (adapted from World Bank, 2011; Universite catholoique de Louvain (UCL) et al., 2018)

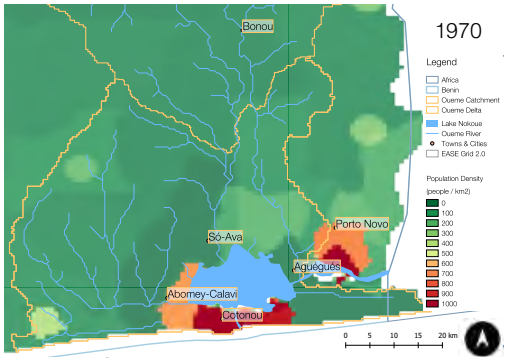

(a) Population density 1970

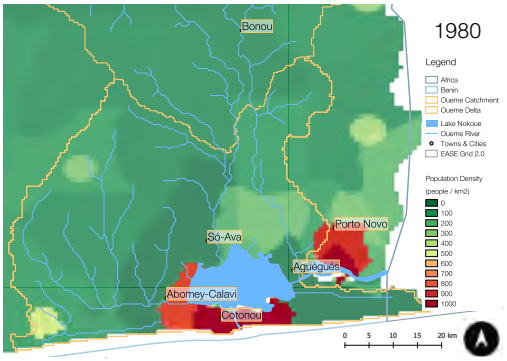

(b) Population density 1980

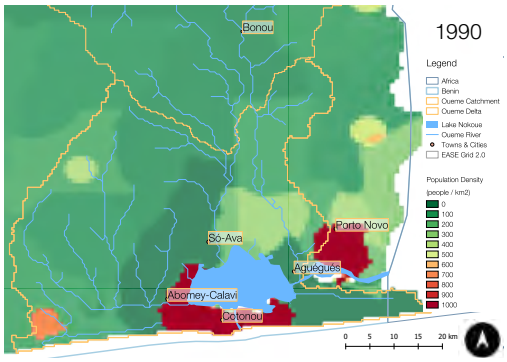

(c) Population density 1990

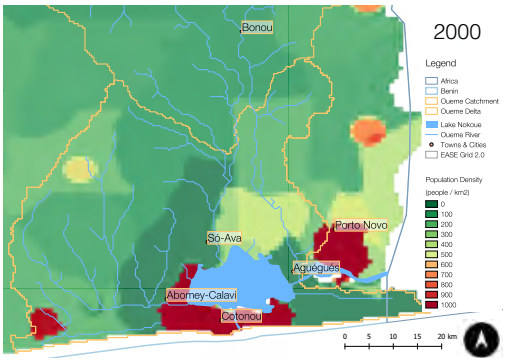

(d) Population density 2000

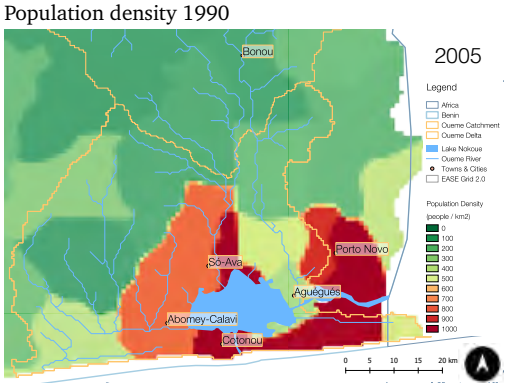

(e) Population density 2005

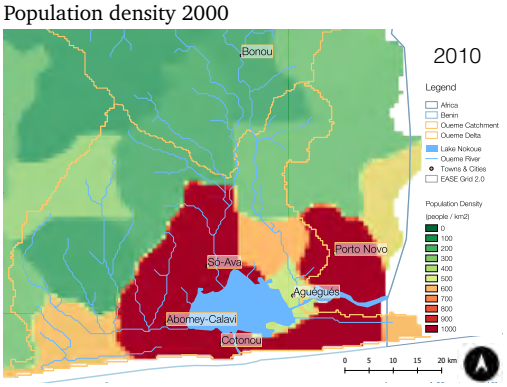

(f) Population density 2010

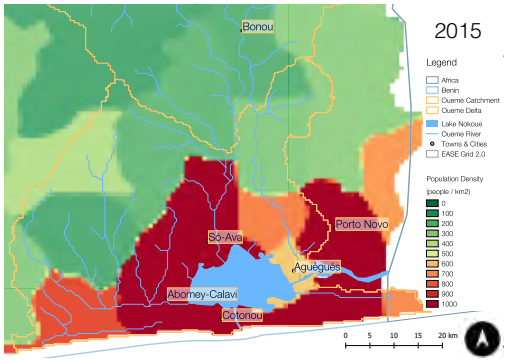

(g) Population density 2015

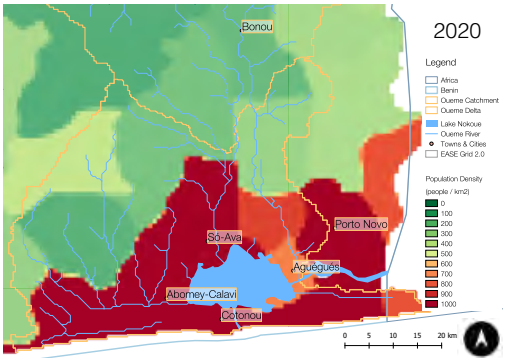

(h) Population density 2020

Figure 2.5. Population growth in the Ouémé Delta 1970 - 2020 (data from Center for International Earth Science Information Network - CIESIN, 2016; Center for International Earth Science Information Network - CIESIN, 2017)

2.2 Inundations in Benin

In West-Africa the past decades have been dominated by inundation disasters, whereas disasters by drought have played a smaller role. Inundations in Benin occur both because of local excess rainfall (pluvial inundations) and excess surface water originating from the Ouémé river or a tributary (fluvial inundation). Towards the South of the Ouémé catchment, the Ouémé delta starts (approximately near Bonou), characterised by wide floodplains and little elevation. Although inundations are a natural process in these type of regions, in 2010 severe inundations hit the Ouémé delta causing over 800.000 affected people and 46 deaths (Universite catholoique de Louvain (UCL) et al., 2018). This formed the start of several studies and projects to improve understanding of inundations and take mitigative measures. Figure 2.6 gives an impression of the 2010 inundations. For this research the most important developments are the flood early warning system (SAP) operated by DG-Eau (Section 2.2.1) and the hydrodynamic model of the Ouémé delta by Rita Houngue (Section 2.2.2) both directly or indirectly connected to the OmiDelta programme (Section 2.2.3).

2.2.1 Flood Early Warning System (SAP)

The flood early warning system (officially called "Système d'Alerte Précoce" (SAP)), was launched in 2013 and is operated by the water directory (DG-Eau) and the National Civic Protection Agency (ANPC) (United Nations Development Program (UNDP), 2013; DG-Eau, 2014). The system relies on near-real-time discharge data from various discharge stations in the Ouémé catchment and other atmospheric conditions, such as rainfall. The lead time of inundations and the emergency threshold per station are known. Processing the data is still a laborious procedure and suffers from data gaps and power or internet cuts, which occur regularly. DG-Eau is therefore in need of additional methods that can work independently of and complementary to the current SAP.

2.2.2 Hydrodynamic flood model

Researcher Rita Houngue, affiliated with the research the University of Abomey Calavi (UAC) develops a MIKE hydrodynamic model of the Ouémé delta to estimate water depths based on river discharge at the Bonou station. Due to the lack of a high resolution DEM, accurate water level estimation in the Ouémé delta is difficult. Fieldwork showed that in some cases the 2010 flood level marks are still visible on buildings and constructions. However, since the model still relies on the aforementioned DEM, and the required differential GPS devices are not always available, the added value of such measurements diminishes.

2.2.3 OmiDelta

Between December 2016 and June 2021 the Dutch government funds the OmiDelta programme which will be carried out by SNV, comprising a WASH and IWRM program (SNV Netherlands Development Organisation, 2016). NGO's, CSO's and private sector parties are among the participating parties. The IWRM programme consists of the technical assistance of Beninese governments and organisations and this research aims to support the available knowledge of the IWRM programme.

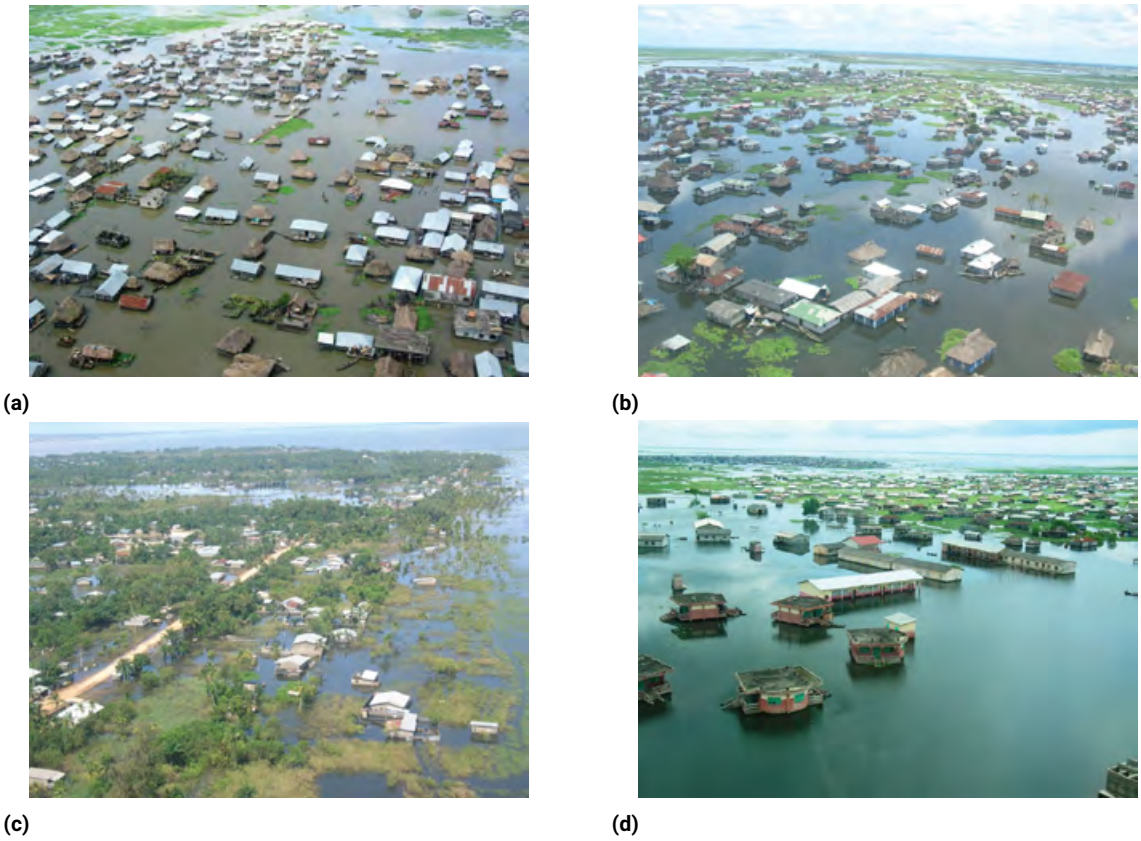

Figure 2.6. Impression of inundations in the Oueme delta in 2010 (World Bank, 2011)

Theoretical Background

3

This chapter provides relevant background information for this research. This research is based on the use of optical (Section 3.1.1) and passive microwave (Section 3.1.2 - 3.3) remote sensing, in particular to retrieve information about surface water. For those interested, this chapter provides a short introduction to the physical basics of microwave remote sensing, which serves as the main data provider for the inundation extent mapping model (IEMM). A considerable share of information presented in this chapter is based on the reference work by Iain Woodhouse, which is recommended for further reading (Woodhouse, 2006). The aim of this chapter is furthermore to present the limitations of current methods.

3.1 Remote Sensing

Remote sensing is officially defined as "*the process of acquiring information about an object or phenomenon without making actual physical contact with it, as opposed to on-site observation or on-site sensing. This often requires the use of aerial sensor technologies such as those used in reconnaissance airplanes and satellites in order to detect and analyse objects on the Earth, usually on the surface*" Technopedia, 2018. In this research (also common in colloquial language), the term remote sensing is used short for the official "satellite remote sensing".

Both optical and (passive) microwave remote sensing sensors make use of capturing electromagnetic radiation from the solar or microwave spectrum (Figure 3.1). An important characteristic of remote sensing sensors is the four types of resolution: spectral, radiometric, spatial and temporal (Figure 3.2). Note that sensors are a trade-off between resolutions, especially between spatial and temporal resolution.

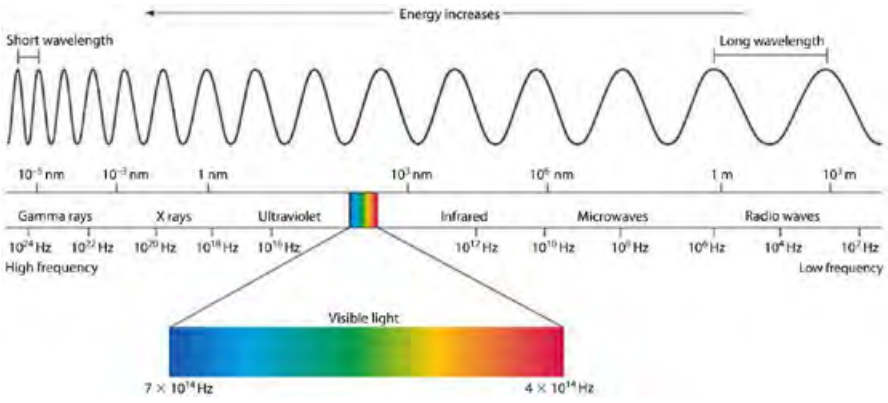

Figure 3.1. The electromagnetic spectrum (Mini Physics, 2018)

Images obtained by remote sensing can contain various types and intensities of noise. To increase the quality of the image, various types of radiometric, topographic and atmospheric corrections can be applied. However, since the focus of this thesis lies merely in the interpretation of imagery, detailed information on (post-)processing remote sensing imagery is omitted.

- **Spectral resolution**
  Spectral resolution refers to the number of wave bands and the bandwidth of wavelengths which can be captured by a sensor. If this bandwidth is very narrow, it might capture some very specific wavelengths, but the energy intensity is low. However, if the bandwidth of the sensor is too large, it loses its ability to capture specific wavelengths. Taking the same example of the visible spectrum, many satellites carry blue, green and red optical sensors. Landsat sensors have between 4-7 bands, MODIS 36 and nowadays, hyper-spectral sensors (Hyperion; 242 bands) can capture a continues range of wavelengths, which allows the user to select nearly the exact wavelength.

- **Radiometric resolution**
  The sensors receive radiation and transform that to a digital intensity scale. The radiometric resolution determines how many levels of intensity a pixel can have. Typical values range from 8 to 14 bits, corresponding to 256 till 16.384 levels, respectively.

- **Spatial resolution**
  Spatial resolution refers to the size of pixel that is recorded in a raster image, usually square areas ranging from 1 to 10.000 meter side lengths. High spatial resolution imagery can nowadays be less than a meter. Working with publicly available data, 10 meter is the highest possible resolution for optical imagery, whereas some microwave imagery comes at 25 or 50 kilometer resolution. The recorded spatial resolution greatly determines which information one can distinguish from the displayed pixel output as seen in.

- **Temporal resolution**
  Revisit time of a satellite (hence the frequency of overpasses) determines how often a certain image is recorded. High temporal resolution is required for studying dynamic processes. For this thesis diurnal (i.e. daily) imagery is preferred, which is already a very high frequency. When combining identical satellites, such as the Terra and Aqua series by NASA, even higher temporal resolution can be achieved (namely, semi diurnal). Well-known satellite missions like Sentinel and Landsat provide temporal resolutions ranging from 10 - 18 days.

3.1.1 Optical remote sensing

Optical satellite remote sensing refers to the visible ($\lambda = 400 - 700nm$), near-infrared (NIR; $\lambda = 750 - 1400nm$) and short-wave-infrared (SWIR; $\lambda = 1400 - 3000nm$) domain of the electromagnetic spectrum. Optical sensors usually carry several bands in the visible spectrum (e.g. Red, Green, Blue) and one (or more) for the NIR and SWIR spectra. Optical remote sensing can be used to analyse surface water by making use of the characteristic of low spectral radiance of surface water, especially pronounced near the NIR and SWIR end of the spectrum. The most

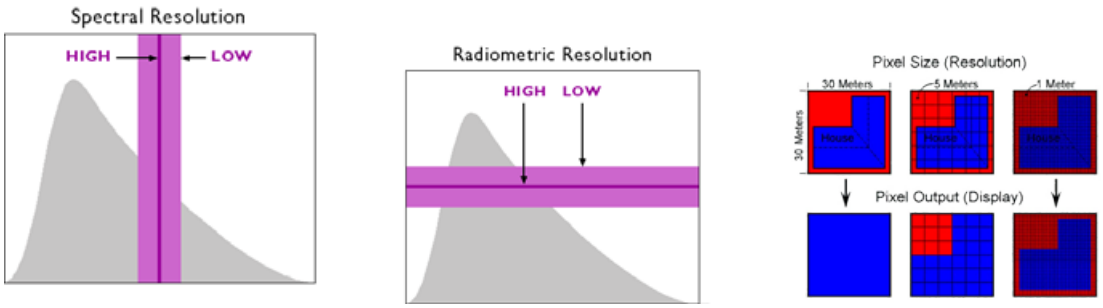

(a) Spectral resolution **(b)** Radiometric resolution **(c)** Spatial resolution

Figure 3.2. Spectral, radiometric and spatial resolution (own work)

common methods to analyse surface water by means of optical remote sensing are by spectral thresholding or through one of the three indices: Normalized Difference Water Index (NDWI; Equation 3.1 (McFeeters, 1996)), Modified Normalized Difference Water Index (MNDWI; Equation 3.2 Xu, 2006) and Normalized Difference Moisture Index (NDMI; Equation 3.3 Wilson and Sader, 2002).

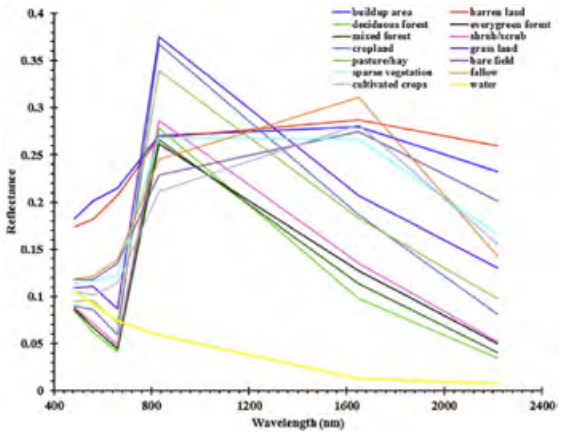

Figure 3.3. Spectral profiles of different land covers (NASA, 2018)

$$NDWI = \frac{Green - NIR}{Green + NIR} \tag{3.1}$$

$$MNDWI = \frac{Green - SWIR}{Green + SWIR} \tag{3.2}$$

$$NDMI = \frac{Red - NIR}{Red + NIR} \tag{3.3}$$

The radiation intensity in the visible spectrum is high, resulting in potentially high spatial resolution imagery (Figure 3.6). However, the visible domain suffers from noise caused by atmospheric haze, cloud cover and cloud shadows. Several cloud-removal techniques exist, such as compositing one artificial cloud-free image based on several partially cloud-free images. The

downside of this technique is that it takes away any temporally important information if the compositing time-frame becomes too large. It is not exceptional that clouds dominate certain regions and seasons, leaving very few suitable images.

Optical satellites					
Name	Launch	End	Spatial resolution (m)	Revisit time (days)	Sensors
Landsat 8	2013	active	30	16	OLI/TIRS
Landsat 7	1999	active	30	16	ETM+
Landsat 5	1984	2013	30	16	MSS/TM
Landsat 4	1982	1993	30	16	MSS/TM
Landsat 3	1978	1983	80	18	MSS/RBV
Landsat 2	1975	1983	80	18	MSS/RBV
Landsat 1	1972	1978	80	18	MSS/RBV
Terra	1999	active	250	1	MODIS
Aqua	2002	active	250	1	MODIS
Sentinel 2	2015/2017	active	10	10	MSI

Figure 3.4. Overview of current and previous optical satellite missions (own work)

3.1.2 Microwave remote sensing

Microwave remote sensing measures spectral radiance in the microwave spectrum and exists in two forms: passive and active. The former uses a radiometer to observe energy that is radiated (or reflected) by the Earth's surface or the atmosphere. The latter, of which radar (radio detection and ranging) is an example, generates its own illumination and measures the subsequent scattered energy. Microwave wavelengths lie between 0.1 and 1 m and are more commonly referred to by their frequency (300 GHz – 0.3 GHz). Most radiometers operate in the range 0.4-35 GHz ($\lambda = 0.8 - 75cm$). Microwave systems can operate day and night, even under clouded conditions. Furthermore it can be complementary to other forms of remote sensing, such as the optical imagery. Passive microwave sensing is well calibrated and nowadays, due to its record of service, long time series datasets exist, which in some cases provide us with 40 years of (near) daily data. Although both the active and passive form benefit from these characteristics, passive microwave imagery is available on longer time-scales with more consistent sensor characteristics, hence this research focuses on passive microwave. For a more fundamental background on the origin of microwave radiation, the propagation and atmospheric attenuation, Appendix B provides a concise overview.

3.2 Microwave Brightness Temperature

Bypassing the fundamentals of microwave remote sensing, the relevant concept for this research comes down to microwave brightness temperature (Equation 3.4), described as a linear relation as a result of the Rayleigh-Jeans approximation. The received spectral radiance is referred to

(Dis)advantages of optical remote sensing imagery	
+	-
High spatial resolution	Dependent on cloud cover
Temporal resolution	Intra-system variations

Figure 3.5. Limitations of optical remote sensing imagery (own work)

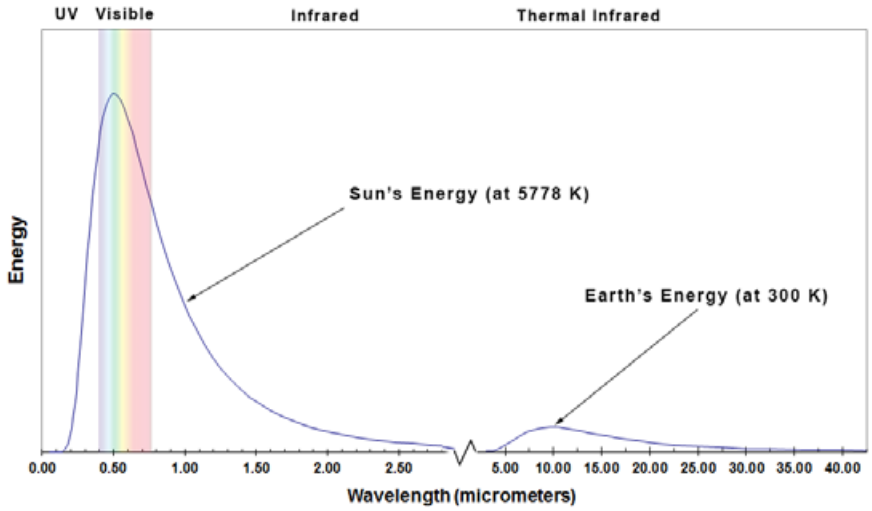

Figure 3.6. Theoretical blackbody radiation curves for the Sun and Earth. Notice the large energy differences for the visible and microwave domain. Microwave frequencies studied in this research (37 GHz $\equiv$ 8.0 mm = 800 μm) have very low radiative energy (Humboldt State University, 2014)

.

Microwave satellites (Ka-Band; 37GHz)										
Name	Sensor	Launch	End	Frequency (GHz)	Earth inclination angle (degrees)	Sensitivity (K)	Swath width (km)	Spatial resolution (km)	Polarisation	Revisit time (days)
Nimbus 7	SMMR	1978	1988	37.0	50.3	unkown	800	14 x 14	V,H	2
DMSP - F08	SSM/I	1987	1991	37.0	53.0	0.4	1400	28 x 37	V,H	1
DMSP - F10	SSM/I	1990	1997	37.0	53.1	0.4	1400	28 x 37	V,H	1
DMSP - F11	SSM/I	1991	2000	37.0	53.2	0.4	1400	28 x 37	V,H	1
DMSP - F13	SSM/I	1995	2009	37.0	53.3	0.4	1400	28 x 37	V,H	1
DMSP - F14	SSM/I	1997	2008	37.0	53.4	0.4	1400	28 x 37	V,H	1
DMSP - F15	SSM/I	1999	active	37.0	53.5	0.4	1400	28 x 37	V,H	1
DMSP - F16	SSMIS	2003	active	37.0	53.1	0.22	1700	28 x 37	V,H	1
DMSP - F17	SSMIS	2006	active	37.0	53.1	0.22	1700	28 x 37	V,H	1
DMSP - F18	SSMIS	2009	active	37.0	53.1	0.22	1700	28 x 37	V,H	1
Aqua	AMSR-E	2002	2015	36.5	54.8	0.3-1.1	1450	8 x 14	V,H	1
ADEOS-II (Midori)	AMSR(-J)	2003	2003	36.5	55.0	unkown	1600	8 x 14	V,H	1
GCOM-W1	AMSR2	2012	active	36.5	55.0	0.45	1450	7 x 12	V,H	1

Figure 3.7. Overview of current and previous passive microwave missions for Ka-band (own work)

as brightness temperature (T_B) and should be interpreted merely as an observational quantity rather than a physical quantity: T_B does not explicitly imply any assumption about the physical properties of objects. Brightness temperature (T_B) can be used to either monitor (surface) temperatures as well as emissivity properties. The latter is used extensively in microwave studies as (natural) materials have large variations in emissivity. Therefore it is important to understand the effect of underlying materials or processes on the measured T_B .

$$T_B = \epsilon T \qquad [K] \tag{3.4}$$

Note that equation 3.4 is for unpolarised measurements and after single polarisation loses a factor of two (Equation 3.5).

(Dis)advantages of passive microwave remote sensing imagery	
+	-
Temporal resolution	Low spatial resolution
Independence of clouds	
Intra-system consistency	

Figure 3.8. Limitations of passive microwave remote sensing imagery (own work)

$$T_{B(\nu,p)} \equiv \left(\frac{\lambda^2}{\kappa}\right) B_\nu \qquad [K] \tag{3.5}$$

To understand the role of emissivity, one needs to understand the concept of blackbody radiation, as emissivity is defined as the relative brightness of an object compared to the (theoretical) brightness at the same temperature T (Equation 3.6). Natural materials do not behave like blackbodies, but their emissivity properties differ. These varying properties can be used to distinguish materials or processes.

$$\epsilon \equiv \frac{\text{brightness of an object at temperature } T}{\text{brightness of a blackbody at temperature } T} \qquad [-] \tag{3.6}$$

3.2.1 Propagation of Microwaves

Before describing microwaves in the real world, it is important to understand the concept of propagation of microwaves. Microwaves are a form of electromagnetic waves and pass through some medium, for instance the atmosphere or the Earth's soil. Describing the electromagnetic material properties is therefore important, because this interaction is the reason why we can retrieve useful information, or why noise is disturbing our signal. Three terms are used to characterise electromagnetic material properties: electric permittivity (ϵ), magnetic permeability (μ) and electric conductivity (g). For remote sensing, only the first term is of interest, which describes the ability of a substance to store electrical energy in an electric field.

3.2.2 Dielectric constant

The electric permittivity (also known as dielectric constant) is compared to the permittivity of free space (in vacuum): ϵ_0 and is 8.8542 x $10^{-12} C^2 N^{-1} m^{-2}$. The permittivity of a material is the product of this free space permittivity and relative permittivity, defined as $\epsilon = \epsilon_r \epsilon_0$. The relative permittivity has a real and complex part (Equation 3.7)

$$\epsilon = \epsilon_r^{'} - i\epsilon_r^{"} \qquad [-] \tag{3.7}$$

The real part ($\epsilon_r^{'}$) corresponds to a lossless dielectric constant and the imaginary part ($i\epsilon_r^{"}$) to energy losses, or attenuation by the medium the microwave travels through. This might seem rather strange, but for now it is important to keep in mind that most solid materials (found

on Earth) are non-conducting (also known as 'dielectric') and can be described by the relative permittivity, or "dielectric properties". Water (i.e. in the form of surface water, soil moisture, vegetation moisture) has a much higher relative permittivity than most materials, because it is a good conductor. This is the result of the ability of the water molecule of free rotation and the molecule's alignment of its permanent electric dipole in response to an applied electromagnetic field. Therefore, when water is added the effective dielectric constant of the soil increases strongly. Since the emission and scattering properties of the soil are strongly influenced by the soil dielectric constant, both active and passive microwave measurements are highly sensitive to soil moisture (De Jeu et al., 2008). These are the properties that are studied extensively in microwave remote sensing research. The reason for giving attention to describe relative permittivity is that it enhances understanding the subsequent concept of 'penetration depth', which is an important characteristic of microwaves.

3.2.3 Penetration depth

Penetration depth is, as the name suggests, the depth in the material from where the microwave signal can be observed (Equation 3.8). For microwaves, a higher frequency (i.e. smaller wavelength) means a lower penetration depth than a lower frequency (i.e. higher wavelength). For example, for soil moisture studies, L or P-band can be used and have a few meters of penetration depth in dry soil. In the case of this research, the point of interest is fluvial inundations, hence very superficial (or, low-penetrative) surface characteristics are required.

$$\delta_p \approx \frac{\lambda\sqrt{\epsilon_r^{'}}}{2\,\pi\,\epsilon_r^{''}} \qquad [m] \tag{3.8}$$

3.3 Microwaves in the real world

Microwaves have to pass two 'layers' before they are observed by a satellite sensor: the atmosphere and Earth's soil. In either medium, radiation will be attenuated to some extent and more effects need to be included when studying microwaves interacting with real objects than the theoretical concepts as described in earlier sections. Emissivity plays an important role in the interaction with real objects. Figure B.1 explains a part of the atmospheric attenuation. Specific literature on microwave Ka-band characteristics might be limited, but soil moisture studies for lower frequencies form an excellent source of information. Although this study does not focus on soil moisture, higher frequency microwaves have a small penetration depth, hence the term "soil moisture" should be interpreted as surface water. Therefore, it is useful to study soil moisture retrieval concepts for this research.

3.3.1 Atmosphere

The following section follows De Jeu in describing the atmospheric contribution to the observed T_B as described by equation 3.9, with T_u and T_d as the up-welling and down-welling atmospheric emissions respectively, τ_a as atmospheric opacity, r_p as surface reflectivity and T_{bp} as surface

brightness temperature (De Jeu et al., 2008). The subscript p denotes the polarisation (either horizontal (H) or vertical (V)).

$$T_{Bp} = T_u + \exp(-\tau_a) T_{bp} + r_p T_d \qquad [K] \tag{3.9}$$

The surface brightness temperature is a function of the physical temperature of the radiating body and its emissivity as described by equation 3.10, where T_s is the thermodynamic temperature of the emitting layer and e_{sp} is the smooth-surface emissivity (De Jeu et al., 2008).

$$T_{Bp} \cong e_{sp} T_s \qquad [K] \tag{3.10}$$

The latter is defined in equation 3.11, with R_s as the smooth-surface reflectivity (De Jeu et al., 2008).

$$e_{sp} = (1 - R_{sp}) \qquad [-] \tag{3.11}$$

One of the advantages of microwaves is that under certain conditions the atmosphere is completely transparent, which in the case of microwaves is for frequencies less than 10 GHz (Woodhouse, 2006). For frequencies near 100 GHz, the atmosphere is nearly completely opaque, and for intermediate frequencies it is important to understand the effect of the atmosphere and atmospheric constituents on the measured T_B (or more specifically emissivity). Generally, for frequencies below 50 GHz there is little or no effect from clouds, but heavy thunderstorms or rain events can influence the T_B. The radiative transfer equation describes the intensity of radiation propagating in a media that simultaneously absorbs, emits and scatters the radiation. In practice, this means that scattering arising from water droplets (hydrometeors) needs to be accounted for when analysing higher frequency microwave temperatures. The absorption over a path between s' and s is the optical depth or opacity.

3.3.2 Soil

Soil emissivity properties rely heavily on the aforementioned dielectric constant and in particular the contrast between water ($\tilde{8}0$) and dry soil ($\tilde{3}$). Combinations of soil and water result in soil-water mixtures (4-40), which is used for soil moisture studies (De Jeu et al., 2008) (figure 3.9a). As section 3.2.2 describes, the real part of the dielectric constant determines the propagation characteristics of the energy as it passes upward through the soil and the imaginary part determines the energy losses (figure 3.9b). Soils are commonly described as a heterogeneous mixture of air, water, soil, clay, etc.. Many other influencing factors of soil emissivity exist such as temperature, vegetation, salinity, soil texture and wavelength (De Jeu et al., 2008). Dielectric constant is difficult to measure outside controlled laboratory environments, and therefore mixing models exist, which estimate a dielectric constant based on the given percentage of rock/water/air present in the soil.

3.3.3 Polarisation

Microwaves are electromagnetic radiation composed of electric and magnetic parts, which propagate perpendicular in free space. The polarisation generally deals with the electric field of

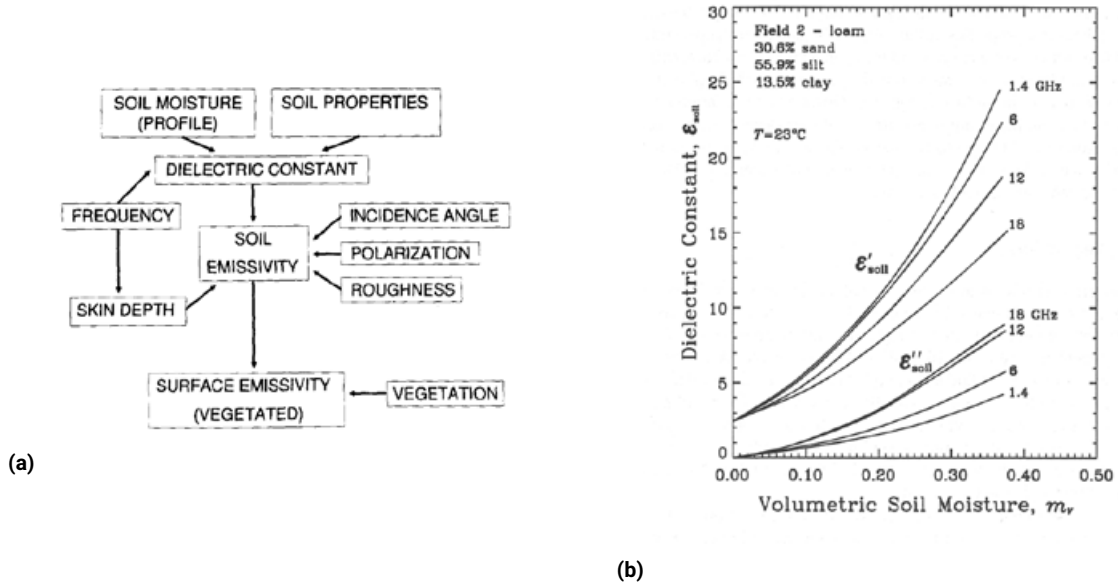

Figure 3.9. (a) The interdependencies of emissivity on a surface covered by vegetation (Van de Griend and Owe, 1994) (b) The real and imaginary parts of the dielectric constant as function of soil moisture. Notice how the real part ($\epsilon^{'}$) representing the energy propagation is larger for low frequency microwaves. The opposite holds for the imaginary part ($\epsilon^{"}$), which represents the energy losses. Lower frequency microwaves are therefore appropriate for soil moisture studies and higher frequency (e.g. 37 GHz) are suited for studies interested in more superficial soil characteristics (Woodhouse, 2006)

the radiation and for terrestrial passive microwave antennas exists in two forms: horizontal (H) and vertical (V). For smooth surfaces the theoretical Fresnel relationship applies. Figure 3.10a shows the smooth surface emissivity and the soil dielectric constant with an incident angle of 55 degrees for horizontal and vertical polarization, similar to the AMSR-E constellation. Horizontally polarised images are preferred for soil moisture measurements, because the range in smooth surface emissivity (e_s) is larger. The non-linearity for $|\epsilon|$ at lower soil moistures is due to water being tightly bound in the soil matrix, which limits the particles' ability of free rotation. With more water, the soil exerts less force on the additional water, which is able to rotate freely again (free water phase). The reason why this is relevant to note is that soils with a high clay content, generally have a lower dielectric constant than sandy soils at the same water content (De Jeu et al., 2008).

3.3.4 Surface roughness

Roughness decreases the surface reflectivity, thereby increasing the emissivity. Surface roughness determines the degree of scattering and emission caused by the relative size of objects and is therefore a relative concept depending on both the size of an object as well as the incoming wavelength. The definition of a smooth surface for microwave scattering from natural surfaces is usually defined by the Fraunhoffer criterion (alternatively the Rayleigh criterion can be used) (Equation 3.12). For a 37 GHz frequency, corresponding to roughly 8.0 mm wavelength, and with 55 degree incidence angle, this means that $h_{smooth} < 0.4mm$, telling us that practically any

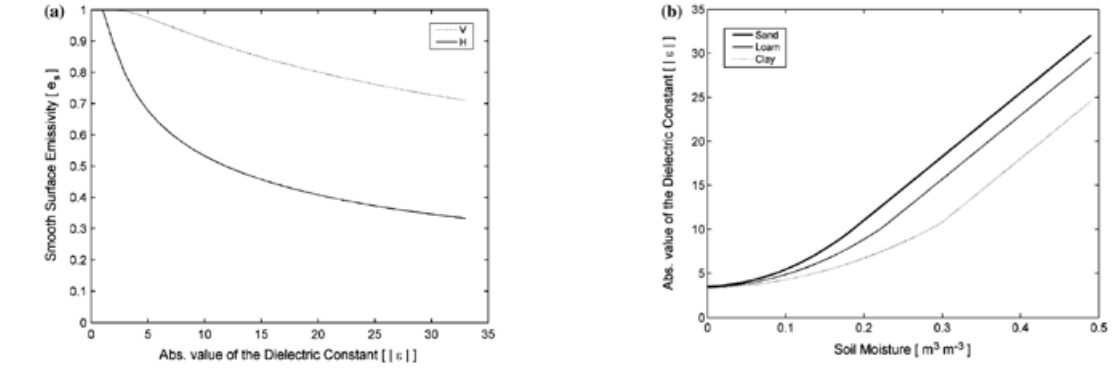

(a) (b)

Figure 3.10. (a) Differences in smooth surface emissivity for vertical and horizontal polarised microwaves, under 55 degrees incident agnle, based on the Fresnel equations (De Jeu et al., 2008). (b) Comparison of the soil dielectric constant and soil moisture for typical sand, loam and clay soils (De Jeu et al., 2008)

signal picked up by the passive microwave sensor will always be considered a rough surface condition.

$$h_{smooth} < \frac{\lambda}{8 \cos \theta_i} \qquad [m] \tag{3.12}$$

3.3.5 Vegetation

The low penetration depth of higher frequency microwaves causes a strong influence of vegetation. There are two ways how the observed microwave emission above the canopy are affected by vegetation. First, vegetation absorbs or scatters radiation emanating from the soil. Second, vegetation also emits its own radiation. These are opposing effects, meaning that with the soil emission increases for increased vegetation, while emissions from vegetation will increase De Jeu et al., 2008.

$$T_{bp} = T_s e_{rp} \Gamma_p + (1 - \omega_p) T_c (1 - \Gamma_p) + (1 - e_{rp})(1 - \omega_p) T_C (1 - \Gamma_p) \Gamma_p \qquad [K] \tag{3.13}$$

Equation 3.13 describes radiative brightness temperature T_{bp} as a function of the thermodynamic temperatures of soil and canopy, T_S and T_C, respectively, the single scattering albedo ω_p and the transmissivity Γ (De Jeu et al., 2008). The first term of the above equation defines the radiation from the soil as attenuated by the overlying vegetation. The second term accounts for the upward radiation directly from the vegetation, while the third term defines the downward radiation from the vegetation, reflected upward by the soil and again attenuated by the canopy. The transmissivity is further defined in terms of the optical depth, τ, and incidence angle, u (Equation 3.14).

$$\Gamma = exp(\frac{-\tau}{\cos u}) \tag{3.14}$$

Optical depth is a measure for the opacity given by the absorption between an arbitrary point $s^{'}$ and the instrument location at s (equation 3.15). Vegetation attenuation and emission can be accounted for by the vegetation optical depth (VOD).

$$\tau_{\upsilon}(s', s) = \int_{s'}^{s} \kappa_{\upsilon}(s")ds" \tag{3.15}$$

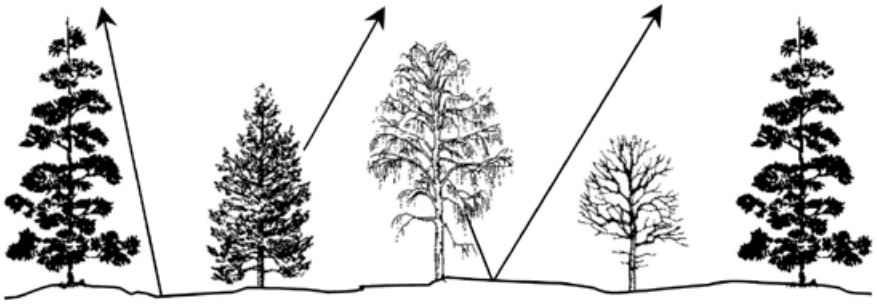

Figure 3.11. Influence of vegetation on microwave radiation (De Jeu, 2003)

3.3.6 Salinity

Since this research focuses on higher frequency passive microwave signals, influence of salinity is neglected, since this reportedly only has a significant influence for frequencies smaller than 6 GHz (Woodhouse, 2006).

3.4 CM-ratio

Previous research by Brakenridge presents the CM-ratio: an inundation detection method using a Calibration (C) and Measurement (M) cell (Brakenridge et al., 2007), and a subsequent discharge estimator (HR) (Equation 3.16). The measurement cell brightness temperature (T_{B_M}) is obtained by selecting a region where inundations can occur. With 'calibration cell' (T_{B_C}) Brakenridge refers to a cell unaffected by (fluvial) surface water, which corrects for daily and seasonal variation of the emissivity and land surface temperature in the measurement cell signal.

$$HR_{CM} = r_{CM} = \frac{T_{B_C}}{T_{B_M}} \qquad [-] \tag{3.16}$$

The concept is optimised for measuring river discharge and uses an emission model developed under the fluctuation-dissipation theory, using a certain silt-loam soil type with a given soil dielectric constant as a function of volumetric soil moisture. The traditional polarisation ratio (PR) is defined in equation 3.17.

$$PR = (T_{bV} - T_{bH}/(T_{bV} + T_{bH})) \tag{3.17}$$

(Dis)advantages of the CM-ratio	
+	-
Cloud-independence	Does not present spatial info
Proven inundation detection results	Does not use differences between discharge and inundation
Temporal resolution	

Figure 3.12. Limitations of CM-ratio (own work)

The "paired measurement method" uses a ratio of brightness temperature for horizontal and vertical polarisation (Equation 3.18), where C is the calibration target area and M the area of interest (measurement area).

$$HR = T_{bH}(C)/T_{bH}(M), VR = T_{bV}C/T_{bV}(M) \tag{3.18}$$

Substituting equation 3.4 in 3.18 gives equations 3.19 and 3.20, which holds when the physical temperatures in each location are similar (i.e $T(C) \approx T(M)$).

$$HR = [T(C)/T(M)] * [e_H(C)/e_H(M)] \equiv e_H(C)/e_H(M) \tag{3.19}$$

$$VR = [T(C)/T(M)] * [e_V(C)/e_V(M)] \equiv e_V(C)/e_V(M) \tag{3.20}$$

The calibration measurement pair should be chosen such that:

- They are located within the correlation length scale of physical temperature T and thus T is approximately cancelled in the paired ratio.
- C and M are measured in the same time-frame (a few minutes difference is allowed).
- C is selected as a relatively stable calibration target unaffected by river change.
- M is selected such that its area contains the largest change in reach water surface area with discharge change.

The shortcomings of the CM-ratio are (i) that it is difficult to spatially interpret the inundation detection signal and furthermore (ii) that it does not deliberately use the differences between discharge and inundation. Instead, it aims to find a discharge estimator (HR_{CM}) to mimic river discharge. The CM-ratio makes use of level 3, 37 GHz brightness temperature data from the AMSR-E passive microwave radiometer on the descending node with horizontal polarisation.

.


DONA-CHRIST-GJ Phot, Vidéo & CD

Methods and Approach 4

This chapter provides an overview of the research structure and the data, tools and methods that were used. Figure 4.1 depicts how the different research components relate to each-other and subsequently discusses the different stages: input (Section 4.1), methods (Section 4.2) and results. The proposed method to estimate the inundation extent, i.e. Inundation Extent Mapping Model (IEMM), is presented in section 4.3. Methods to obtain information on timing of inundations are explained in section 4.4. The approach to study related processes of inundation, such as precipitation and population growth, are presented in section 4.5.

4.1 Research Structure - Input

Figure 4.1 shows the three data sources that are used for this research: fieldwork (figure 4.2), satellite imagery (Figure 4.3 and 4.4) and additional databases (Figure 4.2).

4.1.1 Fieldwork

Defining the research objectives benefited from conducting fieldwork, which included interviewing over 40 ((inter)national) experts and interviewing local inhabitants at several locations in the Ouémé Delta. It is worthwhile to mention that the latter do not necessarily experience inundations as an inconvenience. In fact, farmers in the delta consider it an important source of irrigation and soil fertilizer which has been part of the culture of local communities for a long time. The most important points of interest for local inhabitants and experts, which helped to define the objectives of this research are:

- **Inundation Extent**
  Local inhabitants suggest that annual inundations are intensifying and the inundation extent is not always known among the population, nor by government officials. The flood early warning system in place (SAP) only works with empirical relations between extreme discharge and affected regions. Improved understanding about vulnerable zones is desirable.

- **Timing**
  People need time to harvest their crops, prepare their dwelling and shelter their cattle and families. Sometimes, fluvial inundations occur rapidly, leaving insufficient time for people to take damage control measures. Although predictive inundation detection goes beyond the scope of this research, gaining knowledge on the timing of inundations is important.

Discharge data at Bonou (1952-2011) was provided by Beninese researchers. The Water Directory (DG-Eau) operates discharge stations and collects data at more stations, depicted in figure 2.1 and this research approach could be expanded when data from more stations is granted.

Flood-mark inspection throughout the catchment showed that the record 2010 flood-marks are still visible on buildings and constructions throughout the Ouémé delta. Water levels from previous year are usually also visible or remembered by the local community, but besides that no information on (record) water levels were collected. However, due to the lack of high (vertical) resolution elevation data, the added value of these water level estimates is limited.

A conventional inundation model namely requires at least discharge data, elevation data and preferably some validation data on water levels, which is exactly the type of data that is (apparently) lacking in data-scarce environments. The notion that in some cases inundation extent models are preferred over water level models was confirmed by locals stating that detailed information on water levels is usually not their primary concern: both 10 cm and 50 cm of inundation could cause cattle or children to drown and prevent crops from being harvested.

More information about these fieldwork interviews, the site analysis and the inundation extent survey can be found in Appendix C.

4.1.2 Satellite Imagery

Optical and passive microwave satellite imagery, in particular brightness temperature from passive microwave radiometers, forms the core of the data used for this research (Figure 4.3). Satellite imagery from the Aqua and Terra satellites (2003 - 2010; NASA) are used for model testing, because both the optical MODIS sensor and AMSR-E are mounted on Aqua (MODIS also Terra) satellites, resulting in coinciding overpass times of optical and passive microwave measurements as well as the period of data coverage. Furthermore, the record 2010 inundations are captured in this time-frame. Especially passive microwave radiometry forms the backbone of data collection in this research and therefore the radiometric characteristics are investigated prior to IEMM development.

Passive microwave imagery is applied in the CM-ratio as developed by Brakenridge and later adapted into a new method for inundation scale estimation, referred to as the CMC-ratio. Information on the CMC-ratio presented in section 4.2.

4.1.3 Databases

Additional databases are consulted for collecting environmental validation data for the CMC-ratio and for the analysis of accounting factors and impact of inundations, which in practice comes down to rainfall data. The disaster event database EM-DAT provides an overview of reported inundation disasters and the subsequent health and economic impact. Past and expected population growth is included to make a first step towards investigating inundation impact.

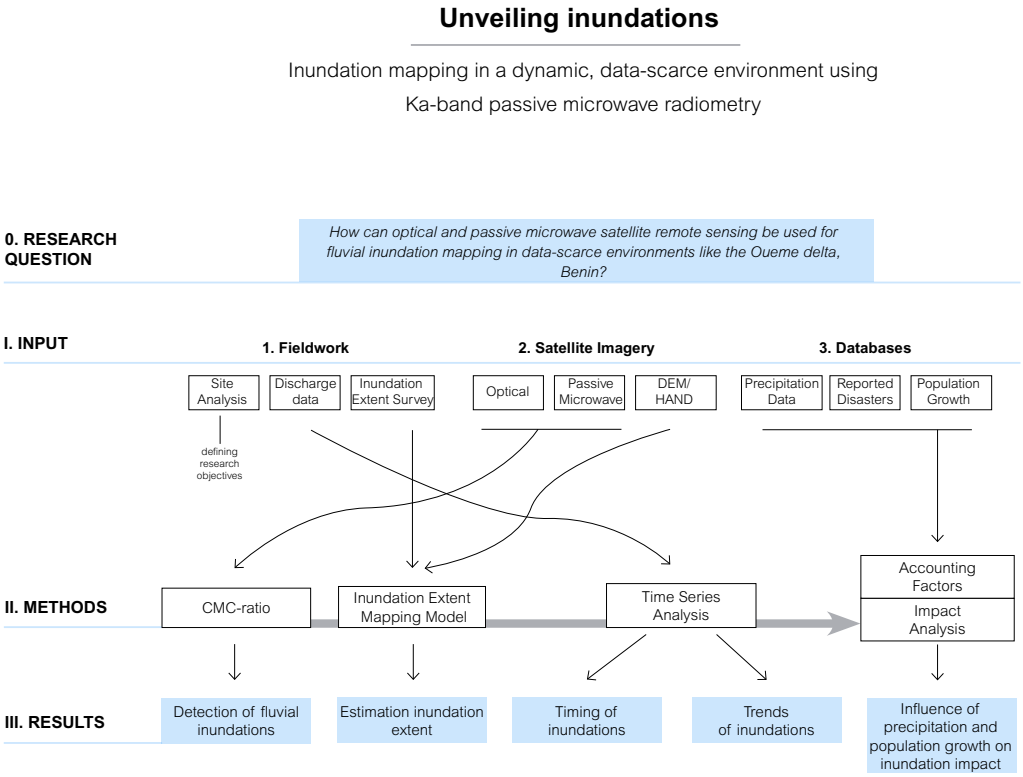

Figure 4.1. Schematic overview of the research (own work)

Fieldwork	
Description	Specification
Discharge data	Bonou (1952-2011)
Interviews	>40 national and international experts
Survey system (ODK-Collect)	Open source data collection system for validation of inundation extent 2018

Additional databases	
Description	Specification
Precipitation	NOAA NNDC CDO - Daily global summary of station rainfall data - 1950 - 2014
Disasters	EM-DAT Emergency Database 1970 - 2018
Population	Gridded Population Count 1970-2000 (SEDAC v1) Gridded Population Maps 2000-2020 (CIESIN GPWv4); U.S. CENSUS Population data

Other databases	
Description	Specification
Digital Elevation Model (DEM)	MERIT: Multi-Error-Removed Improved-Terrain DEM

Figure 4.2. Overview of data collection during fieldwork and additional databases (Yamazaki et al., 2017; Universite catholoique de Louvain (UCL) et al., 2018; Funk et al., 2015; Center for International Earth Science Information Network - CIESIN, 2016; Center for International Earth Science Information Network - CIESIN, 2017; U.S. Census Bureau, 2018; NOAA, 2018)

Remote Sensing Data Overview							
Satellite	Sensor	Spatial resolution	Bands	Temporal resolution	Availability	Level	Access
Terra/Aqua	MODIS	250 m (B01-02) 500 m (B03-06)	B01 (Red) B02 (NIR) B03 (Blue) B04 (Green) B05 (NIR 2) B06 (SWIR)	0.5 -1 day	2002 - present	L3	Google Earth Engine: MOD09GQ.006 MOD09GA.006 MYD09GQ.006 MYD09GA.006
Nimbus-7	SMMR	3.125 km - 25 km	37 GHz	1-2 days	1978 - 1988	L3	NSIDC: Calibrated Enhanced-Resolution Passive Microwave Daily EASE-Grid 2.0 Brightness Temperature ESDR
DMSP F08/10/13/15	SSM/I	3.125 km - 25 km	37 GHz	1-2 days	1987 - 2017	L3	
Aqua	AMSR-E	3.125 km - 25 km	37 GHz 89 GHz	1-2 days	2002 - 2011	L3	
GCOM-W1	AMSR2	10 km - 25 km	36.5 GHz	1-2 days	2012 - present	L3	G-Portal JAXA

Figure 4.3. Remote sensing data used for this research (Vermote and Wolfe, 2015c,Vermote and Wolfe, 2015a,Vermote and Wolfe, 2015b,Vermote and Wolfe, 2015d,JAXA EORC, 2013,JAXA, 2018,Brodzik et al., 2016)

4.2 Presenting the CMC-ratio

From the input data the CM-ratio - an existing passive microwave inundation detection method - is transformed to the CMC-ratio: an inundation detection method estimating a surface water fraction used for spatial interpretation. When the CMC-ratio is developed and tested, it will be applied in the following sections to answer the research questions: the Inundation Extent Mapping Model (IEMM; Section 4.3) to provide information about inundation extent; Time series analysis (Section 4.4) to provide information on timing of inundations and observations in inundation trends; Accounting factors (Section 4.5) to analyse trends in extreme daily precipitation and the Impact analysis (Section 4.6) to provide a first step towards analysing the impact of inundations focusing on population growth and affected people by disasters.

The CM-ratio presents a method to generate an inundation detection signal by means of a Calibration (M) and Measurement (M) cell taken from AMSR-E 37 GHz passive microwave radiation. The aim of the CM-ratio is to analyse and mimic river discharge. Discharge and inundation are clearly related, but it should be noted that different processes are measured,

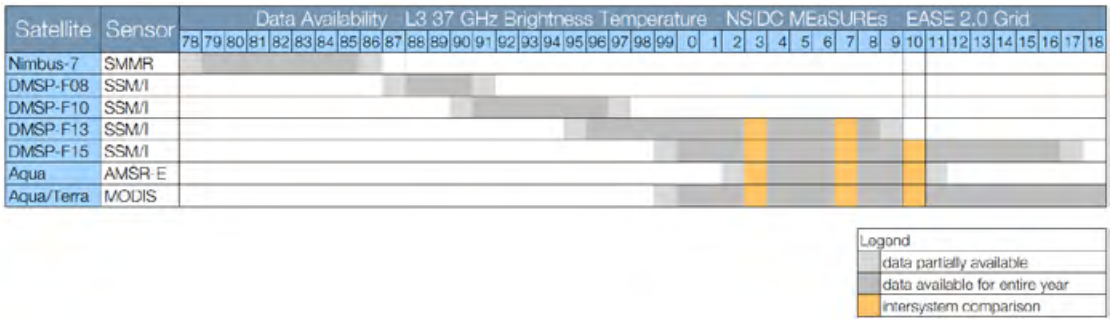

Figure 4.4. Available data for 37 GHz passive microwave radiometry. The first and last year of the missions are often not fully available, hence these are indicated differently. The most important sensor for this research is AMSR-E, the most important year is 2010 (Vermote and Wolfe, 2015c; Vermote and Wolfe, 2015a; Vermote and Wolfe, 2015b; Vermote and Wolfe, 2015d; Brodzik et al., 2016)

which should be dealt as such accordingly. Therefore in this study, the CMC-Ratio is presented (Equation 4.1), which also uses a measurement cell (T_{B_M}), a dry calibration cell ($T_{B_{CD}}$) and introduces an additional (wet) calibration cell ($T_{B_{CW}}$) to find a (daily) fraction of surface water in the measurement cell caused by fluvial inundation (Figure 4.6). The system is tested for a 25 km measurement cell 6 (Bonou), a 25 km dry calibration cell 60 and the 3.125 km wet calibration cell at lake Nokoue (cell 0). The smaller wet calibration cell is due to the limited size of lake Nokoue.

$$r_{CMC} = \frac{T_{B_{C_D}} - T_{B_M}}{T_{B_{C_D}} - T_{B_{C_W}}} \qquad [\%] \tag{4.1}$$

Other measurement cells are studied with the same wet calibration cell, but with different dry calibration cells. The reason why the measurement cell and the dry calibration cell are chosen next to each other is based on the assumption that heavy rainfall might disturb the brightness temperature measurements. Considering that dominant rainfall is caused by the (West-)African Monsoon, which moves from South to North, selecting cells on the same latitude is preferable (Bourles et al., 2007). Brakenridge states that the calibration cell must be taken as close to the measurement cell as possible and the large grid cells from the EASE Grid 2.0 (i.e. the grid providing brightness temperature data) leave no further option but locating the dry calibration cell right besides the measurement cell. NSIDC MEaSUREs dataset offers T_B with different sensor settings. The CM and CMC-ratio are tested on the following settings:

- **Polarisation**
  Images are available with single horizontal or vertical polarisation (Figure 4.5). More information about polarisation is available in Appendix B.

- **Ascending and Descending node**
  Aqua ascending node has overpasses between 13:00-14:00 LT (= 1:00-2:00 PM) and the descending node between 00:30-01:30 LT (= 12:30 - 1:30 AM). The night-time overpasses are supposed to measure more constant land surface temperatures (LST), hence emissivity differences can be distinguished better.

- **Cell Size**
  Available cell sizes are 3.125 km and 25 km. Because of the limited vertical resolution in the MERIT DEM (or HAND) and the need to map a given fraction of surface water as inundation extent, a larger cell is preferable for the measurement cell. Variation in cell response between 3.125 and 25 km signal is also investigated.

- **Noise filter**
  The Savitzky-Golay filter is applied to increase the signal-to-noise ratio in the brightness temperatures and account for missing days. The filter's adjacent data points (i.e. days in this case) and the order-degree polynomial must be uneven and the former must exceed the latter. For instance, a filter of 5 adjacent days can be used up to a 3rd order polynomial, but with 3 adjacent days only to the 1st order (i.e. linear). In this research little data for validation is available, making the estimation of the preferred conditions more subjective than desired. More research should be directed towards the implications of this filter in further research in more data-rich environments.

Brakenridge uses 37.0 GHz H(orizontal)-D(escending) brightness temperature. Vertical polarisation is recommended for measuring land surface temperatures (Brakenridge et al., 2007; De Jeu et al., 2008).

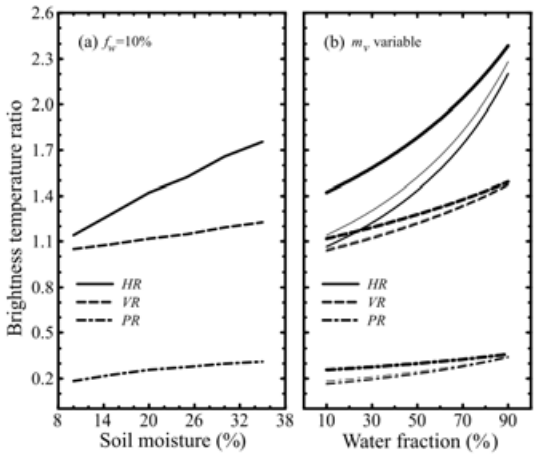

Figure 4.5. Change in brightness temperature ratio HR, VR and PR at 36.5 GHz for a given silt-loam soil type. The thin lines indicate dry conditions (m_v = 10 %) and thick lines indicate wet condition (m_v = 35 %). The dry HR brightness temperature is more sensitive to soil moisture changes than wet conditions. Therefore horizontal polarized imagery seems preferable. (Brakenridge et al., 2007)

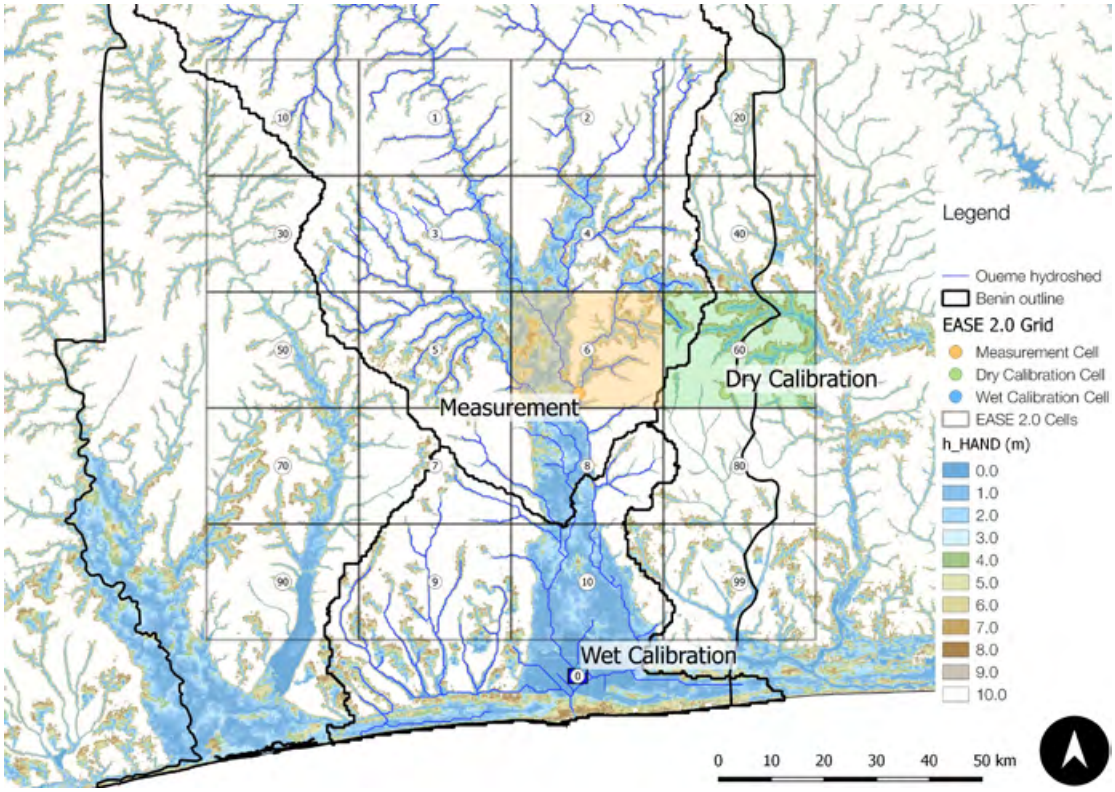

Figure 4.6. MEaSUREs EASE-Grid 2.0. The Measurement and Dry Calibration cells make use of a 25 km grid. A 3.125 km grid is used for the Wet Calibration cell due to the limited size of the lake. Measurements cell are labeled 1-10, the Dry Calibration cells 20 - 100. Cell 6 is the test site, since discharge data is available for this location. Cells 4, 6, 8 and 10 are most important for studying inundation behaviour. Cells 7 and 9 are not used. The units (1-10) are the measurement cells, the tens are the dry calibration cells belonging to the respective measurement cell. For example: cell 60 is the dry calibration cell belonging to measurement cell 6. The wet calibration cell (0) remains the same for all cells. (own work).

4.3 Presenting the Inundation Extent Mapping Model (IEMM)

The Inundation Extent Mapping Model (IEMM) is a collective term for the consecutive steps to obtain information on timing and inundation extent based on satellite remote sensing imagery (Figure 4.7). Cloud-free optical imagery (Section 4.3.1) and passive microwave imagery form the input data for the CMC-ratio, which is the inundation detection method and is tested on several components. The CMC-ratio, gives an inundation scale estimate which can be validated by means of optical imagery. To improve the inundation scale estimate, several inundation scale methods are considered: the 'original' method: Baseline (Section 4.3.3), the Fixed Wet Cell method (Section 4.3.4), the Full method (Section 4.3.5) and the Hybrid method (Section 4.3.6). The inundation scale (i.e. surface water fraction) is then mapped on an elevation map and validated once more with cloud-free MODIS optical imagery (Section 4.3.7). When satisfactory results are produced the inundation extent estimation is ready. The IEMM is set up with 37 GHz passive microwave imagery and tested for 2010 when record inundations took place. The test location is cell 6 including Bonou; the only discharge station with available data.

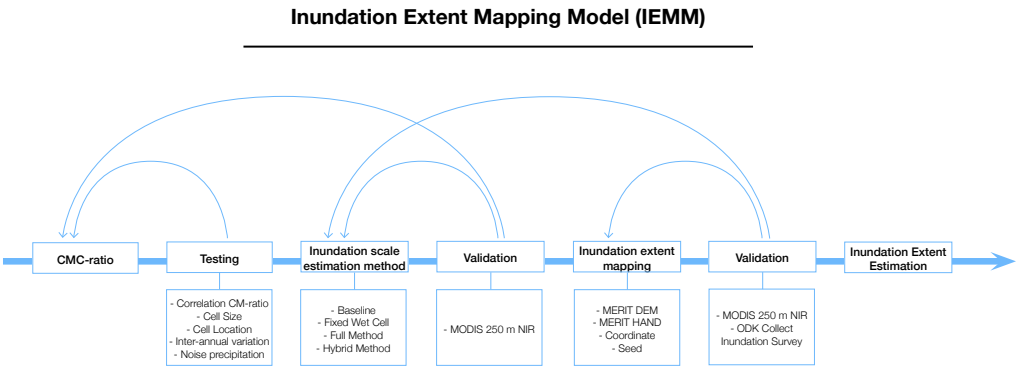

Figure 4.7. Schematic overview of the Inundation Extent Mapping Model (IEMM) (own work)

4.3.1 Optical Imagery

Optical remote sensing has been around since the late 1970's and the temporal and spatial resolution have been improving rapidly. Water bodies can be distinguished by their low surface reflectance properties (Figure 3.3). Regarding inundation analysis however, optical imagery has the disadvantage of sensitivity to clouds and cloud shadows, which especially in the tropics, causes limitations in the applicability during the wet season (Wilson and Jetz, 2016). To what degree optical imagery can be used directly for inundation extent analysis is dependent on the number of cloud-free days during the inundation season.

Besides direct analysis with optical imagery, validation of passive microwave imagery by means of optical imagery on cloud-free days is also possible (Figure 4.8). This again depends on the amount of cloud-free days available during inundations seasons, but requires less cloud-free days

than direct analysis. The validation points will be analysed for 2003, 2007 and 2010, each years with discharge data available and reported severe fluvial inundations.

Using optical imagery to retrieve the size and location of surface water (i.e. inundation extent) is considered with the following methods or indices: NDWI (McFeeters, 1996), MNDWI (Xu, 2006), NDMI (Wilson and Sader, 2002) and setting a threshold on the MODIS NIR surface reflectance band (250 m | 841 - 876 nm) and the MODIS SWIR surface reflectance band (500 m | 1628-1652 nm).

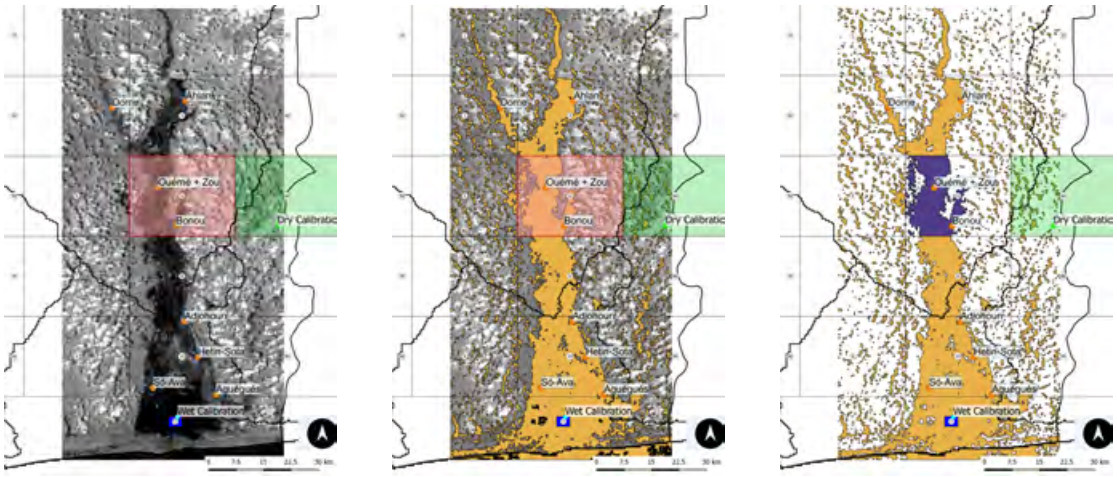

(a) MODIS surface reflectance **(b)** Threshold **(c)** Clipping

Figure 4.8. Process of Optical Imagery validation. (a) MODIS NIR-band surface reflectance - 29-09-2010. (b) Manual threshold to obtain inundation extent. (c) Clipped inundation extent after corrections for cloud (cover and shadows) for Measurement cell 6. The inundated surface area can be compared with the CMC-ratio for the same day. (own work)

4.3.2 Testing CMC-ratio

The CMC-ratio is validated with the following points. Special attention is directed to investigating the behaviour of the additional $T_{B_{CW}}$.

- **Correlation with CM-ratio** - This research relies on the proven method of the CM-ratio for inundation detection and aims for a high correlation (> 90 %) with the method based on the Spearman rank test.

- **Cell size** - The cell size is especially important for the wet calibration cell due to the limited size of lake Nokoue; the largest water body in the Ouémé catchment. Therefore, additional comparisons for the wet cell are done in lake Volta. The measurement and dry calibration cells are kept at 25 km cells exclusively.

- **Location of Dry Calibration cell** - Different locations are considered for both wet and dry calibration cell. It is noted that (i) local precipitation can cause noise in the T_B signal and that (ii) the most dominant precipitation comes from the Monsoon, which propagates northbound over a (latitudinally) straight line. Therefore, dry calibration cells are considered preferably at the same latitude.

- **Discharge intensity** - The Flood Early Warning (SAP) flood thresholds for the Bonou discharge station are compared with the corresponding r_{CMC} signal. These thresholds are >550, >700 and >800 m^3/s for medium to extreme alerts respectively. These different stages indicate how well different stages of inundation can be distinguished by the CMC-ratio.

4.3.3 Method - Baseline

The CMC-ratio is used to approximate the scale of inundation at a given day, for a given location. The method as presented in equation 4.1 is referred to as the baseline method. This consists of the level 3 MEaSUREs T_B data as input and a Savitzky-Golay filter to reduce signal noise and account for missing values. This filter is used as an alternative for the rolling average because it does not require temporal correction for the backward of forward fill method that a rolling average method does. The number of days and order polynomial included in the Savtizky-Golay filter will be tested. The length and the use of the wet cell signal has not been applied in research. The following three alternative methods are considered, varying the role of the wet cell and measurement cell (Sections 4.3.4, 4.3.5, 4.3.6).

4.3.4 Method - Fixed Wet Cell

The wet calibration cell signal shows little seasonality, but a very noisy signal. Therefore this method includes a fixed wet cell ($T_{B_{CW-fix-wet}}$), equal to the (multi-)annual mean wet calibration brightness temperature, thereby omitting the wet calibration cell dynamics and relying on the CM-ratio to accurately mimic inundation patterns (Equation 4.2). Furthermore, it is investigated with which factor $T_{B_{fix-wet}}$ should be adjusted to optimise results, based on MODIS optical validation.

$$r_{CMC\,fixed} = \frac{T_{B_{CD}} - T_{B_M}}{T_{B_{CD}} - T_{B_{CW\,fix-wet}}} = \% \tag{4.2}$$

4.3.5 Method - Full model

The full method relies on including related physical characteristics to improve the resulting r_{CMC} (Equation 4.3). The characteristics considered in this research are: surface roughness, local precipitation, vegetation, distance from wet cell and salinity. Including more physical characteristics (in the Equation referred to as a, b, c, d) can improve results, but also results in enhanced comprehension of related physical processes. This requires full understanding of the influencing characteristics. Since for the time being full comprehension of these processes goes beyond the scope of this research, two adjustments are investigated: (i) adjusting $T_{B_{CW}}$ with a factor ($f_{T_{B_W}}$) (Equation 4.4), or (ii) adjusting $T_{B_{CW}}$ with an offset ($T_{B_{W_{offset}}}$) (Equation 4.5).

$$r_{CMC\,full} = \frac{T_{B_{CD}} - T_{B_M}}{T_{B_{CD}} - T_{B_{CW}}(a, b, c, d)} = \% \tag{4.3}$$

$$r_{CMC\ full-factor} = \frac{T_{B_{CD}} - T_{B_M}}{T_{B_{CD}} - (T_{B_{CW}} * f_{T_{B_W}})} = \% \tag{4.4}$$

$$r_{CMC\ full-offset} = \frac{T_{B_{CD}} - T_{B_M}}{T_{B_{CD}} - (T_{B_{CW}} + T_B W_{offset})} = \% \tag{4.5}$$

4.3.6 Method - Hybrid

The hybrid method makes use of brightness temperature for the measurement and dry calibration cell, but omits the wet calibration cell (Equation 4.6). Instead, it makes use of MODIS cloud-free optical imagery to determine a constant required "wet cell" signal. This wet cell signal is obtained by manually determining the percentage of surface water in a certain cell on these cloud-free days. Then, by reverse engineering, a required wet cell temperature is found, which is kept constant over the entire year. The advantage of this method is that it can be deployed in locations without permanent water bodies of sufficient size in the vicinity of inundated areas. However, it depends on the availability of cloud-free days if this method is applicable.

$$r_{CMC\ hybrid} = \frac{T_{B_{CD}} - T_{B_M}}{T_{B_{CD}} - T_{B_{W\ cloud-free}}} = \% \tag{4.6}$$

4.3.7 Inundation Mapping

The CMC-ratio gives an estimate for percentage of surface water, hence inundated area, per cell. This percentage is subsequently mapped on an elevation map (MERIT DEM or HAND) map by assigning surface water as the corresponding percentile of lowest pixels within the cell. The corresponding h_{HAND} or $h_{DEM}$is found by plotting the cumulative distribution of the percentiles of the elevation map for the given measurement cell (Figure 4.9). Consecutively the measurement cell is filled up (i.e. assigned as surface water) till the corresponding elevation. For cloud-free days, a comparison can be made between the inundation extent given by the IEMM and the true inundation extent found by optical remote sensing imagery. In this research the MODIS NIR (250 m) band is used to set a manual threshold (Figure 4.10).

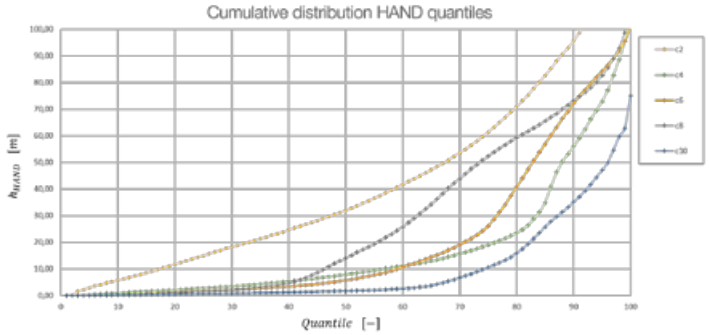

(a) MERIT HAND quantiles

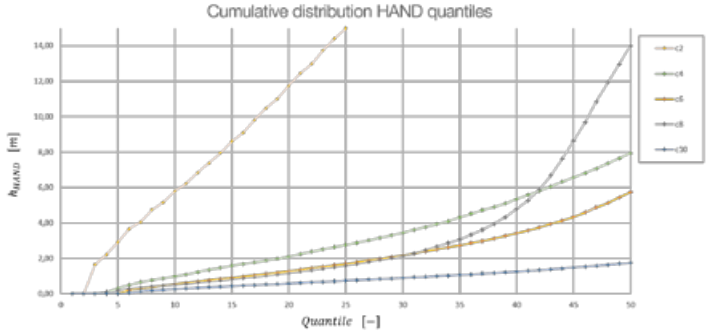

(b) MERIT HAND quantiles - close-up

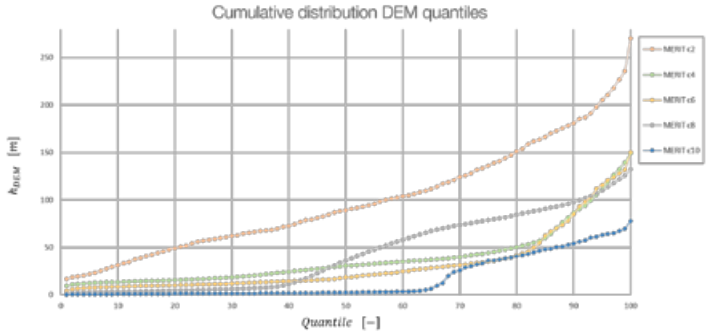

(c) MERIT DEM quantiles

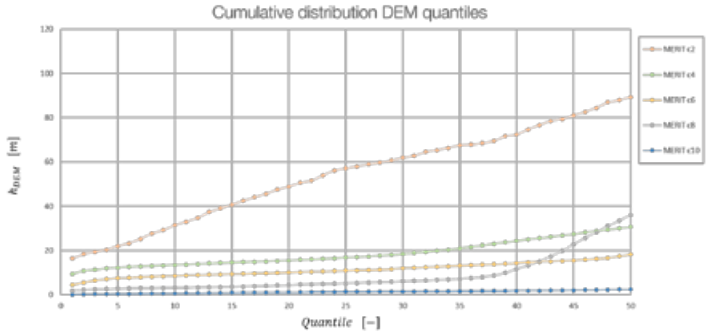

(d) MERIT DEM quantiles - close-up

Figure 4.9. (a) Cumulative distribution of MERIT HAND quantiles in cells 2, 4, 6, 8 and 10. Characteristic for deltas is the relatively large quantity of lower HAND values. (b) Close-up of the lower percentiles. Similarly figure (c) and (d) depict the cumulative distribution of the MERIT DEM. (own work)

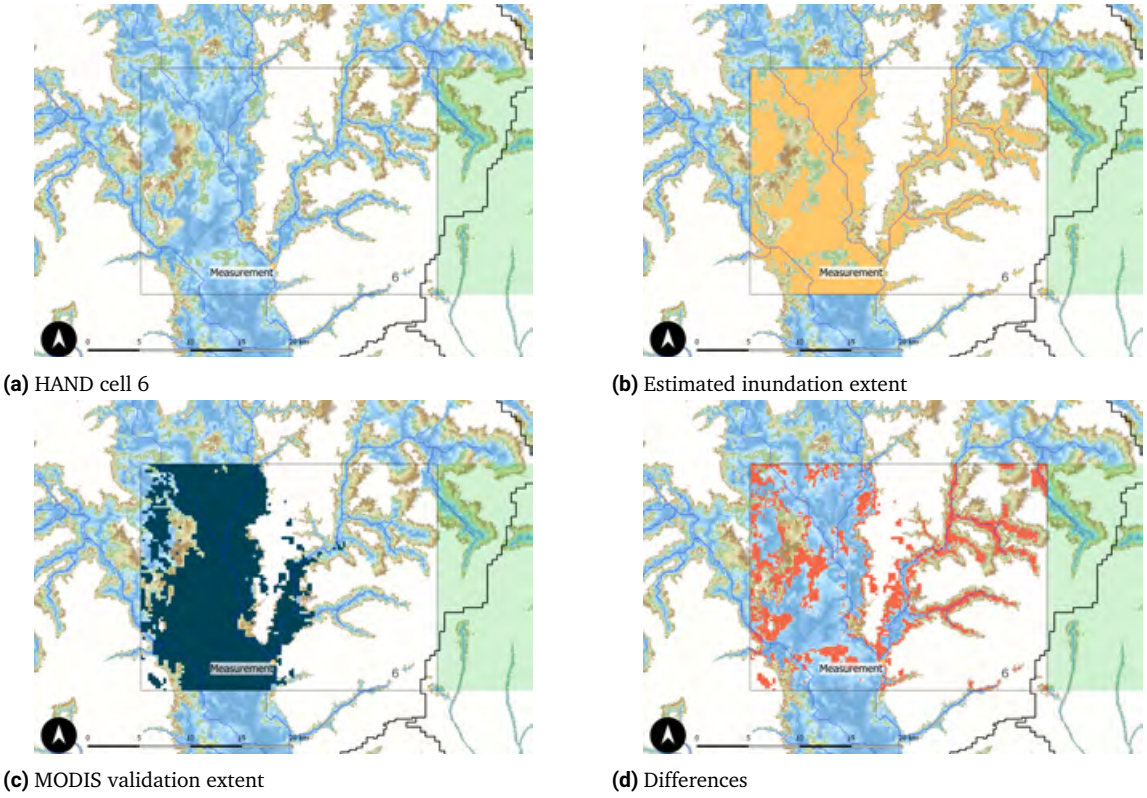

(a) HAND cell 6

(b) Estimated inundation extent

(c) MODIS validation extent

(d) Differences

Figure 4.10. Process of inundation mapping on 29-09-2010. (a) Visualisation of HAND map derived from the MERIT DEM for cell 6 - Bonou Yamazaki et al., 2017 (b) Given a value for r_{CMC} the corresponding lowest quantile in the HAND map is assigned as surface water (In this case quantile 42, see Figure 4.9) (c) Clipped flood extent for the same day, based on MODIS NIR band thresholding (see Figure 4.8. (d) The differences between (b) and (c) (or vice versa) are mapping errors. In the method, false positive and false negative errors are distinguished. (own work)

4.3.8 Inundation Extent Survey

An alternative to inundation extent validation by means of optical imagery was developed by settin up an inundation extent survey in collaboration with Beninese researcher, Rita Houngue, and local university students (UAC) whom collected data on the location of the 2018 inundation extent (Figure 4.11). This survey is based on open source ODK-collect software and has a location accuracy of 5-10 m. The system also works under cloudy conditions and due to the high accuracy can capture inundation extent in tributaries. The survey system has only been modestly deployed in this research because the MEaSUREs dataset is not available for 2018. More information about these fieldwork interview, the site analysis and the inundation extent survey can be found in appendix C.

4.4 Time Series Analysis

The objective of the time series analysis is to investigate (i) how information on timing of inundations, such as start and duration of certain stages of inundation (e.g. inundating floodplains, bank over-topping, maximum inundation) can be obtained (Section 4.4.1), (ii) what multi-annual

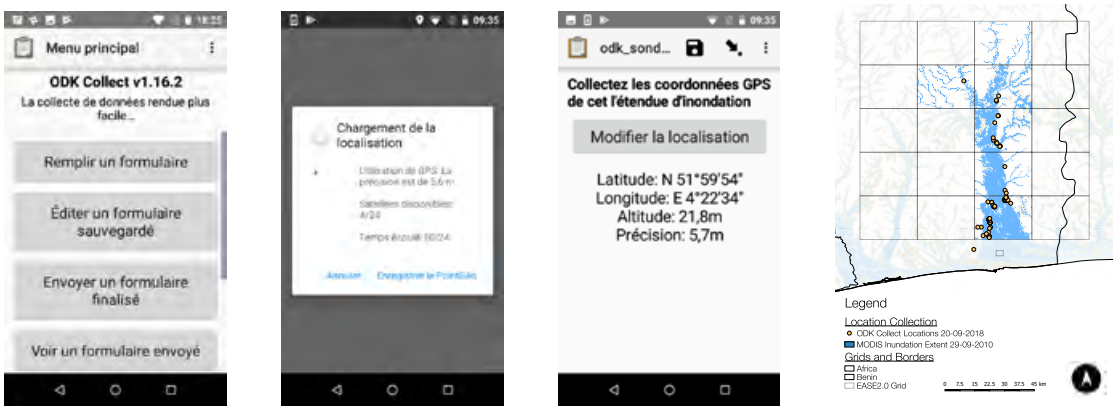

(a) Survey 2018

Figure 4.11. Screenshot of the location collection part of the ODK survey. The system, collected with cell phones, is less suited to collect accurate altitude measurements, but does well in providing the location by means of GPS coordinates (own work).

analyses (e.g. 2004 - 2010) shows about the duration and intensity of maximum inundations (Section 4.4.2) and (iii) if trends in inundation can be observed through multi-system analyses (e.g. AMSR-E - DMSP-F15) (Section 4.4.3).

4.4.1 Timing of Inundations

This section relies on comparisons with discharge data, which is only available for Bonou (1952 - 2011), located within measurement cell 6. As a consequence this entire analysis is only available for cell 6, but could be expanded in further research when more discharge data is granted. Where the CM-ratio makes comparisons to discharge to mimic river discharge, this research uses the CMC-ratio to highlight the differences between (extreme) inundation and discharge. Additionally, empirically defined emergency discharge thresholds by the Flood Early Warning System (SAP) are included ($Q > 550$, 700 and 800 m^3/s). This combination provides information about how different inundation stages can be distinguished from the CMC-ratio and what these thresholds are. This research aims to study the extreme discharge regime particularly.

4.4.2 Multi-annual Analysis

Multi-annual analysis is in the first place executed within the ASMR-E timeframe (2003 - 2010). Goal of this section is to obtain information on the duration and intensity of maximum inundation and to test how well the corresponding inundation stages hold for other years (i.e. dryer, wetter). Days of maximum inundation are compared with the scale of the annual maximum inundation. Differences in timing of maximum inundation in cells 2, 4, 6, 8 and 10 can reveal information about the lead time, which is the speed at which inundations propagate throughout the delta.

4.4.3 Multi-system Analysis

In the time-frame with AMSR-E coverage (2003 - 2010) comparisons between discharge data in cell 6 can reveal information about which surface water fraction corresponds to a certain inundation regime as defined by SAP. This research is especially studying the maximum regime ($Q > 800m^3/s$). Furthermore the timing of maximum inundations is compared to inundations, to show if and how these processes are related.

For trend analysis the available data from AMSR-E is too short, but an advantage of passive microwave radiometry, especially the Ka-band, is that it has been part of satellite missions for the past 40 years in a very similar setting, possibly enabling multi-system comparisons. The full list of satellite missions aimed to include in this thesis is presented in figure 4.4, but fully merging this nearly 40 years of data will require additional researched aimed at data fusion. This research therefore in the first place aims to include the DMSP F13 and F15 missions, because these have overlapping imagery available at the validation years (2003, 2007 and 2010). The incoming brightness temperature signal and the CMC-ratio will be corrected on mean, standard deviation and variance in these overlapping years, to subsequently apply these settings for the entire time-frame. Local population suggests that inundation has been increasing although frequency analysis of discharge station in the Ouémé catchment did draw such clear conclusions on the existence of such a trend (Hounkpè et al., 2015b). Since the CMC-ratio is supposed to be optimized for inundation analysis, it is worthwhile to test if inundation analysis is in accordance with the aforementioned research by Hounkpe.

4.5 Accounting Factors - Precipitation Analysis

With accounting factors, this research refers to the causes of fluvial inundation in the Ouémé delta in the broadest sense of the word such as land use changes, constructions in or close to the Ouémé river or tributaries and upstream precipitation. However, there has been found no literature on large scale constructions or land use changes over the past decades in the middle and upper Ouémé catchment which could influence river runoff and there is no further reason to assume other significant changes influencing runoff patterns. This is how the scope of this section is directly reduced from 'accounting factors' to 'upstream precipitation'. Clearly, it would be too short-sighted making a one-to-one comparison between upstream precipitation and downstream inundations, this exact relation could be better understood by means of, for instance, a hydrological model, but changes in upstream precipitation could have a large effect on downstream inundations. If a trend in upstream precipitation could be observed, this would help to better understand the reported downstream inundations. This research uses daily precipitation measurements between 1950 - 2014 from 5 rainfall stations in the middle and upper Ouémé catchment (Save 1, Save 2, Tchaourou, Parakou, Bohicon) for trend analysis, focusing on finding changes in extreme precipitation characteristics before and after 2000.

4.6 Impact Analysis - Population growth and Disaster analysis

Impact in this research is defined as the number of deaths and people affected by (reported) inundations, which are the two most constant registered categories in the EM-DAT database. Similar to the accounting factor analysis, a comprehensive impact analysis goes beyond the scope of this research. However, considering that past inundations have had a large impact in terms of deaths, homeless, injured and otherwise affected people, it is important to understand what may have caused these large consequences of inundations. This section therefore makes the assumption that the largest influence on the impact side of inundations is the population present in inundation prone areas, suggesting that population growth might have had an influence on the impact of inundations. The consulted datasets are presented in figure 4.2. As stated before, the impact in this research is not related to water levels of inundation, since the scope of the research is different and interviews with locals suggested that water depth is sometimes of minor importance to water presence (i.e. inundations).

Past, present and expected population is studied through population density maps between 1970 - 2020 (i.e. predictions). Population growth will be compared for Benin, cell 2, 4, 6, 8 and 10 and a the sum of these cells referred to as 'delta'. Although the delta comprises large urbanized areas outside of the appointed grid cells (Figure 4.6), cell 10 includes urbanized regions and can thereby be used as a proxy for the entire urban agglomeration in the South.

Disaster reports from the Emergency Database (EM-DAT) exist since approximately 1970 in Benin. Although the database is supposed to contain registrations from disasters since 1900, news articles suggest that heavy floods occured in 1963, which are not registered in the database (Smith, 2010). Therefore, it is assumed that since 1970 the database contains all past (significant) inundation disasters that occured in the Ouémé delta.

.

Results

5

This chapter presents the main results which are relevant to the research questions. Additional results can be consulted in Appendices D, E and F.

5.1 Optical Imagery

The usability of optical imagery depends on cloud cover, which in the Ouémé delta is severe. In this research optical imagery will therefore only be deployed on cloud-free days for validation of passive microwave imagery.

5.1.1 Cloud cover

During the inundation season in the Ouémé delta, daily cloud cover is high (some months and locations > 90%), resulting in few cloud-free images suited for analysis with optical imagery (figure 5.1). On average, in 2003, 2007 and 2010, three cloud-free images per inundation season were available.

Location	Annual mean	January	February	March	April	May	June	July	August	September	October	November	December
Lake Nokoué 6.433°N, 2.461°E	61.5%	39.4%	58.2%	65.8%	72.7%	78.1%	79.9%	74.6%	71.9%	71.9%	65.7%	34.2%	27.3%
Floodplains 6.621°N, 2.450°E	75.3%	47.00%	67.3%	76.2%	78.3%	80.5%	89.2%	93.1%	84.8%	84.8%	77.1%	68.4%	47.7%

Figure 5.1. Average monthly cloud cover based on 15-years, semi-diurnal data obtained by 1-km resolution MODIS satellite images. Notice the high cloud cover during the inundation season (orange) in the floodplains (Wilson and Jetz, 2016).

5.1.2 Surface water retrieval

Analysing MODIS imagery, the best results were obtained setting a threshold on the incoming NIR 250 m surface reflectance band (figure 5.2). NDWI, NDMI and MNDWI have also been tested, but did not improve results, due to the lower spatial resolution of the bands (500 m) and slight noise in the SWIR band.

5.1.3 Validation points

Nine (partially) cloud-free images from the MODIS NIR-band were obtained in 2003, 2007 and 2010, enabling optical validation. These images are manually corrected for cloud-shadows, based on the optical image, HAND and DEM maps. Exceptionally cloud-free conditions were obtained on 29-09-2010, which therefore will be used as reference throughout the rest of this report.

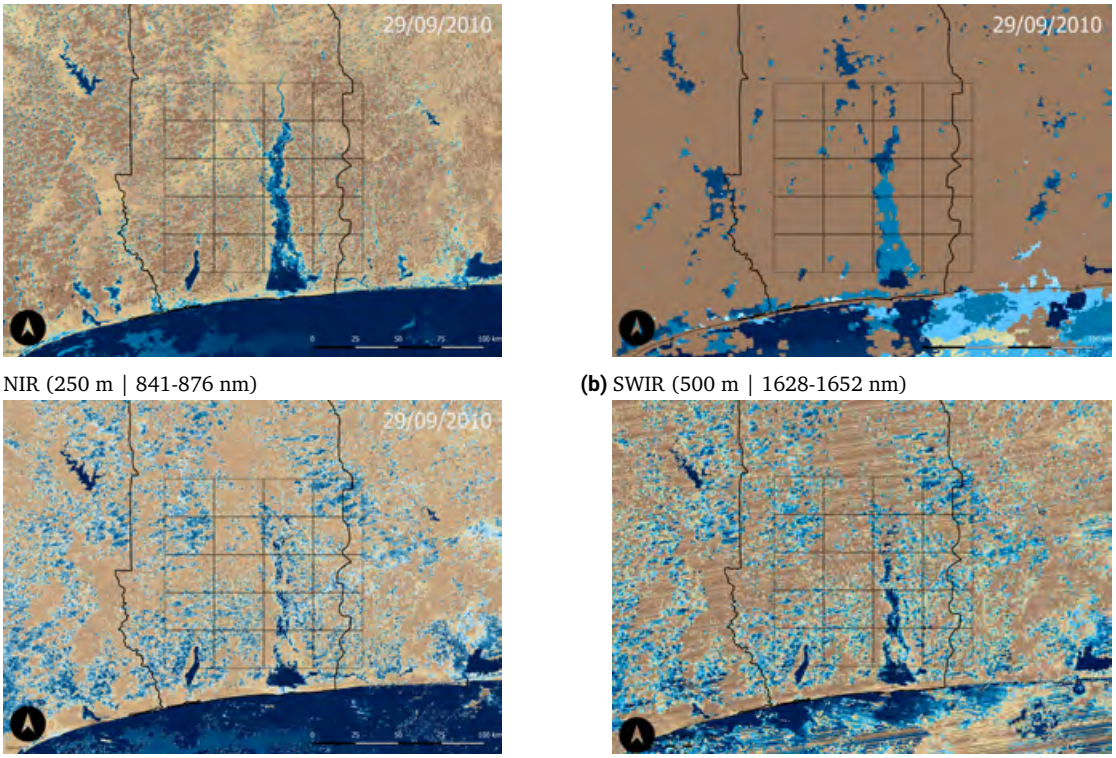

(a) NIR (250 m | 841-876 nm)

(b) SWIR (500 m | 1628-1652 nm)

(c) NDWI (500 m)

(d) MNDWI (500 m)

Figure 5.2. Optical imagery for 29th of September 2010. For optical surface water extent validation, cloud free images from the NIR band are most suitable. (own work)

5.2 Radiometric Characteristics

The CMC-ratio is based on the input of brightness temperature obtained from passive microwave radiometers. This section presents the results of tests done with the incoming brightness temperature signal in terms of band, polarisation (Section 5.2.2), node (Section 5.2.3), cell size (Section 5.2.4), cell location (Section 5.2.6), Savitzky-Golay filter (Section 5.2.5) and local precipitation (Section 5.2.8). The various radiometric settings are available from the MEaSUREs level 3 data.

5.2.1 Band

Band comparison between 37 and 89 GHz shows a preference for the former (figure 5.3). As expected, 89 GHz suffers from noise from atmospheric constituents, especially the oxygen window. When working with the original footprint data, the spatial resolution of the footprint of the 89 GHz channel would be higher (hence preferable), but due to the use of level 3 re-gridded data, both data is available on 3.125 and 25 km cell products, hence this advantage diminishes (although 89 GHz is therefore supposed to suffer less from downscaling results to the 3.125 km EASE-Grid 2.0).

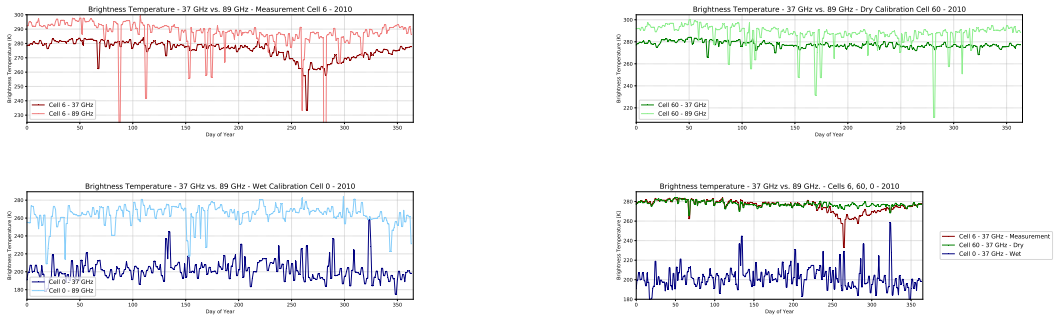

Figure 5.3. Brightness temperature for 37 GHz and 89 GHz AMSR-E bands (horizontal polarisation, descending node) in 2010 for Cell (a) 6, (b) 60 and (c) 0 (own work).

5.2.2 Polarisation

Horizontal polarisation is preferred over vertical polarisation, although differences are small (figure 5.4). Especially the deviation of the measurement cell signal during the inundation season is noteworthy. For the wet cell signal, vertical polarisation seems preferable due to the higher and more constant brightness temperature. When combining horizontal (M, D) and vertical (W) polarised signals, the wet cell signal exceeds the measurement signal, resulting in estimated surface water percentages of > 100 %, which is physically impossible. Vertical polarised brightness temperature is furthermore supposed to be favoured setting when measuring land surface temperature. Since Brakenridge's research also uses the horizontal polarisation, this research adopts the same settings (Brakenridge et al., 2007).

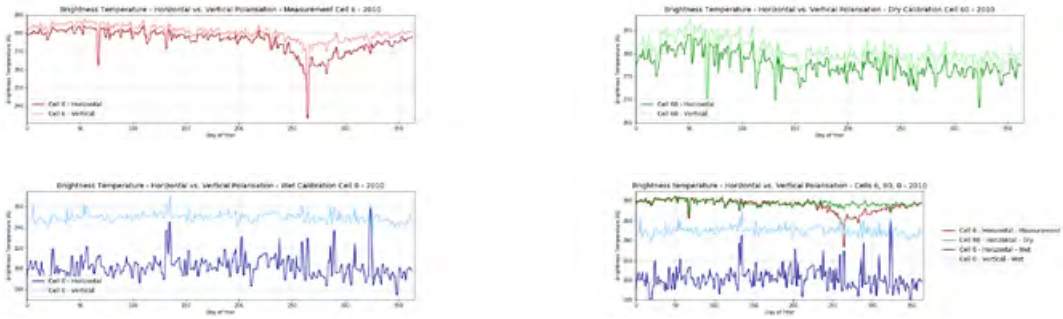

Figure 5.4. Brightness temperature for horizontal and vertical polarisation of 37 GHz AMSR-E bands (descending node) in 2010 for Cell (a) 6, (b) 60 and (c) 0 (own work).

5.2.3 Node

Imagery from the descending node is preferable over the ascending node (figure 5.5). As expected, the descending node (00:30 - 01:30 local night-time overpass) is accompanied with more constant land surface temperatures, which leave a more pronounced role for changes in emissivity to detect the presence of surface water.

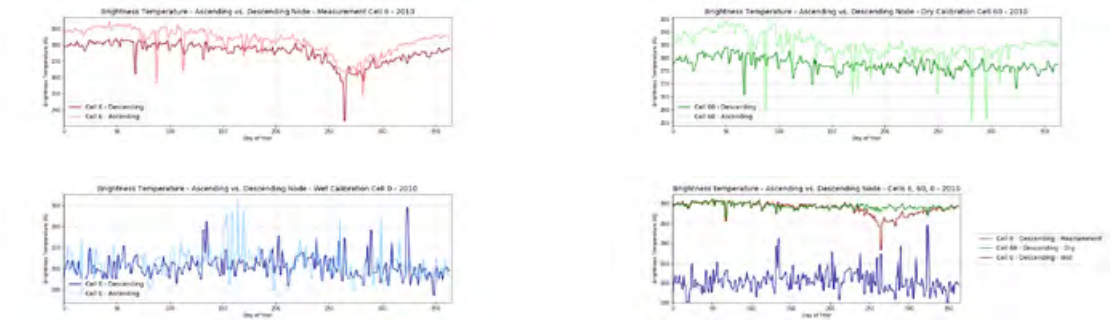

Figure 5.5. Brightness temperature for ascending and descending node of the 37 GHz AMSR-E band (horizontally polarised) in 2010 for Cell (a) 6, (b) 60 and (c) 0 (own work).

5.2.4 Cell Size

Both the 3.125 km and 25 km cell sizes show acceptable outcomes, but the preferred size depends on the objective of the analysis. In this research, where the focus lies on inundation mapping of an entire delta, 25 km tiles are preferred for the measurement and dry calibration cells (Figure 5.6). Problems with the 3.125 km cells also give a practical problem because of the wide floodplains. The dry calibration cell would need to be located (too) far from the measurement cell and might not comply with the requirements of locations of the cells as stated in section 3.4. The wet calibration cell is bound to a 3.125 km cell due to limited size of lake Nokoué.

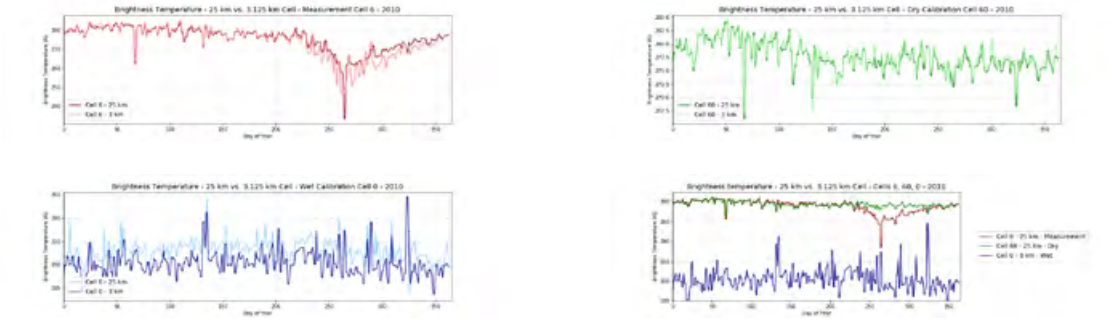

Figure 5.6. Brightness temperature for 3.125 km tiles and 25 km tiles for Cell (a) 6, (b) 60 and (c) 0 (own work).

5.2.5 Savitzky-Golay filter

Both number of adjacent data points (i.e. days) and order polynomial have been tested. For the wet calibration cell a 15 day filter seems preferable, but observations of the measurement and dry calibration cell require a shorter time period (figure Appendix D.13). A higher order polynomial makes the signal more sensitive (figure Appendix D.14). In the end this comes down to a consideration between days and order polynomial of the filter that in this data-scarce environment is difficult to test and thereby becomes somehow subjective. More research should be conducted in data-rich environments, so it can be subsequently applied in other data-scarce

environments. Summarizing, a 15 day, 3rd order filter is used for each brightness temperature cell (figure 5.7).

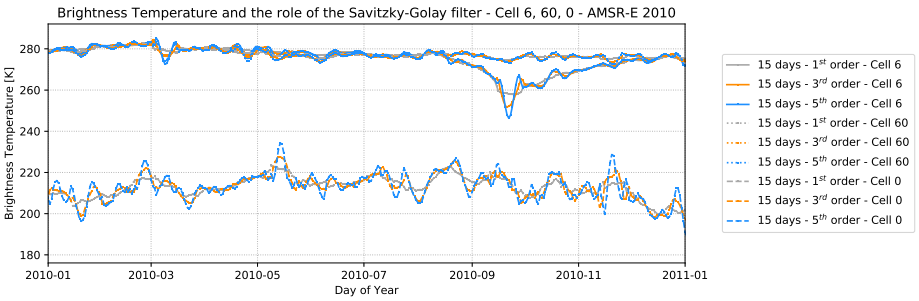

Figure 5.7. Brightness temperatures with the Savitzky Golay filter for a 15-day filter and varying (1st, 3rd, 5th) order polynomials (own work).

5.2.6 Cell Location

The locations are organised in upstream - downstream order (i.e. 2 = upstream, 10 = downstream). The uneven numbers (1 - 9) only contain smaller tributaries giving little information about inundations. In the location comparison an increasing shift in timing (i.e. start date of inundation) and intensity is visible (figure 5.8). Furthermore, location 2 seems subject to hardly any inundations. Only when the two tributaries merge in location 4 (Zou + Ouémé), inundations appear. Due to the limited size of lake Nokoué, the wet calibration cell location was compared to lake Volta (figure 5.9). Interestingly, in this case is that the 3.125 km is constant, but the 25 km signal (which also includes some land surfaces in the cell) shows a similar signal as found for 3.125 km and 25 km cell singals in lake Nokoué. Brightness Temperature on the sea (Gulf of Guinea) shows a similar but lower brightness temperature as lake Nokoué, possibly influenced by the former.

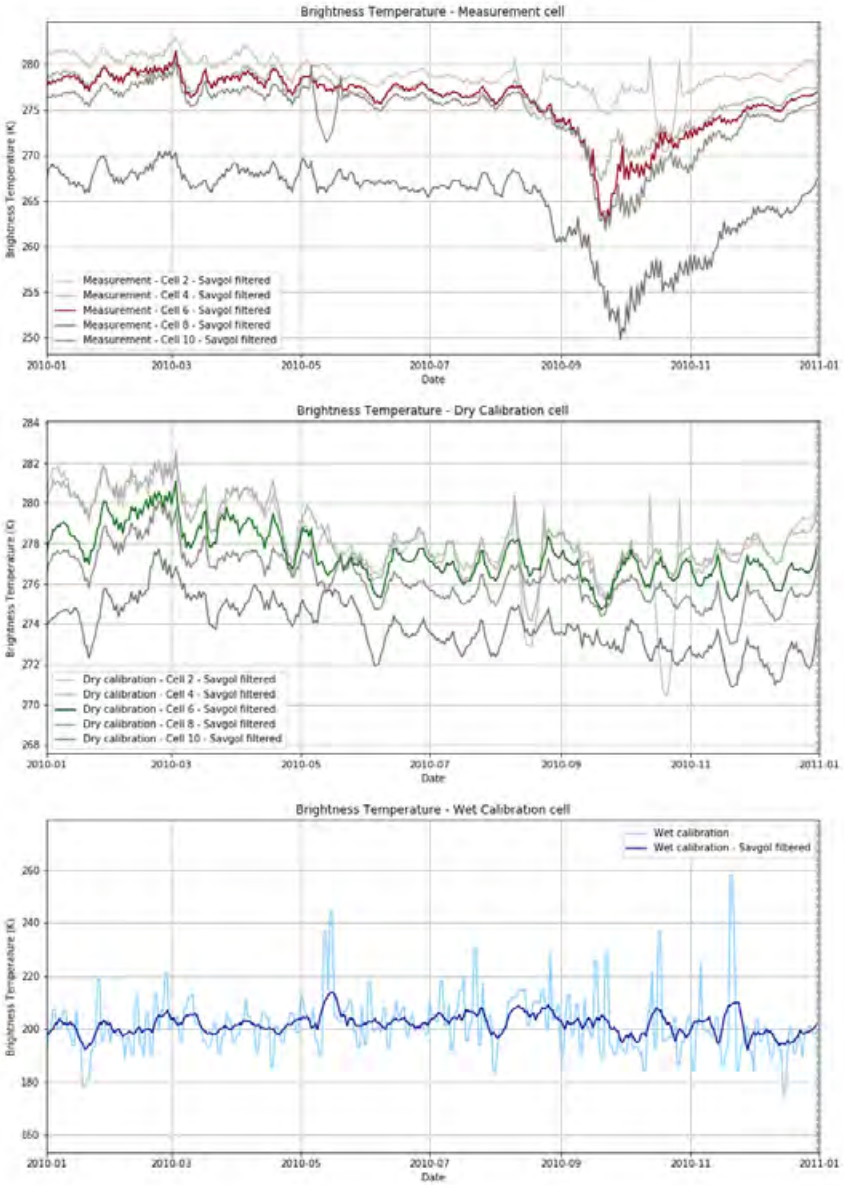

Figure 5.8. Brightness temperatures for Measurement, Dry Calibration and Wet Calibration cells at locations 2, 4, 6, 8 and 10 for 2010 (own work).

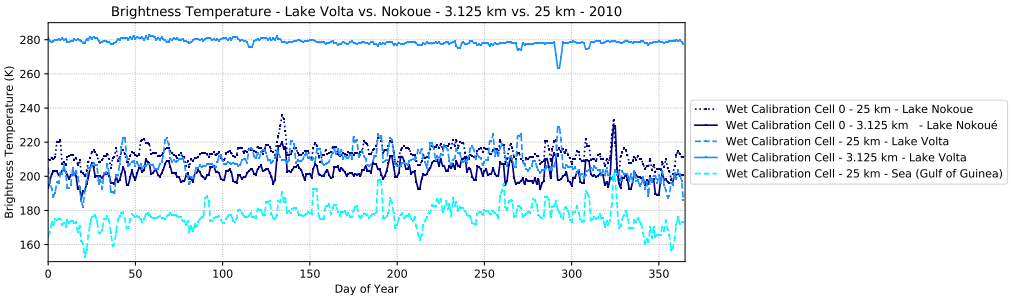

Figure 5.9. Brightness temperature of wet calibration cells in lake Nokoué and lake Volta. The latter shows a more constant signal on the 3.125 km cell, which we would expect for lake Nokoué as well. (own work).

5.2.7 Dry vs. Wet year

Comparing brightness temperature over time shows clear seasonality and inter-annual differences (Figure 5.10). For instance, 2005 was a year without registered inundations and the deviation in the measurement cell is significantly less than in years with recorded disasters, such as 2003, 2007 and 2010.

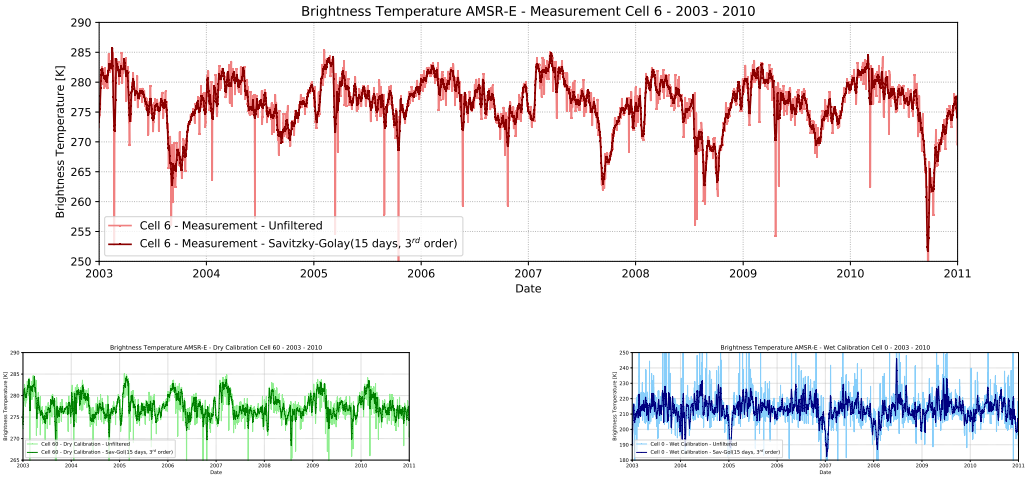

Figure 5.10. Brightness temperature over the AMSR-E period (2003 - 2010), showing clear seasonality in measurement cell 6 (a) and dry calibration cell 60 (b), but less in wet calibration cell 0 (c) (own work).

5.2.8 Local precipitation

Because of the short wavelength of the 37 GHz frequency band ($\lambda \approx 8mm$), large droplets might interfere with the brightness temperature signal. Analysis however showed no correlation (figure 5.11).

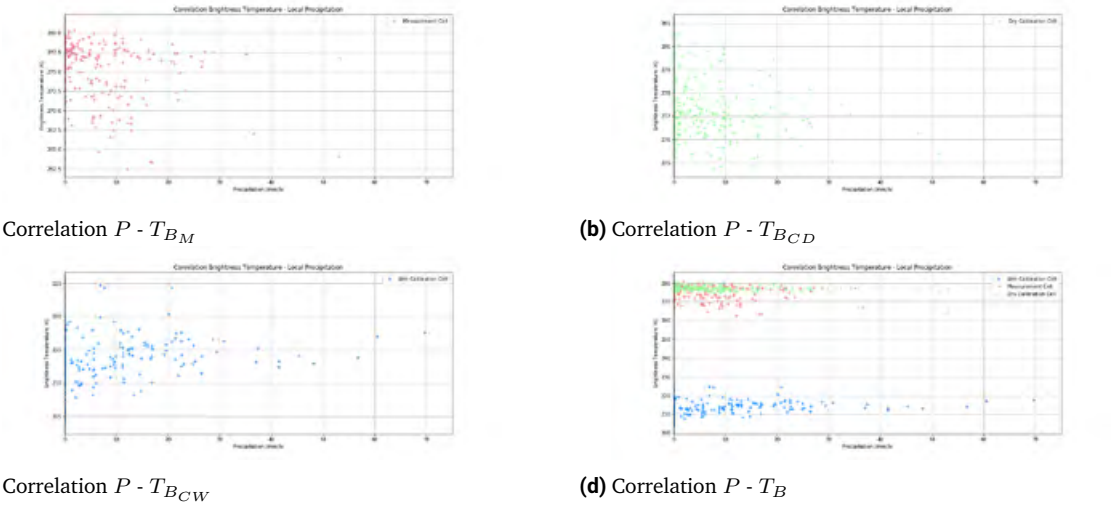

(a) Correlation P - T_{B_M}

(b) Correlation P - $T_{B_{CD}}$

(c) Correlation P - $T_{B_{CW}}$

(d) Correlation P - T_B

Figure 5.11. Correlation between T_B and local precipitation in each respective cell (i.e. Measurement, Dry, Wet cell) obtained by CHIRPS Daily precipitation with local station calibration (Funk et al., 2015)

5.3 CMC-ratio

Based on the analyses conducted on the individual brightness temperature signals, the CMC-ratio is deployed to estimate the scale of inundations and therefore subjected to the following tests. First, the correlation with its predecessor, the CM-ratio, is analysed (Section 5.3.1). Second, the outcome of locations of cells (measurement and dry calibration) and a multi-annual signal is presented (Section 5.3.2). Third, the inter-annual variation is depicted (Section 5.3.3).

5.3.1 Correlation with CM-ratio

Correlation between the CM-ratio and the CMC-ratio is very high: over 99 % according to Spearman's rank (Figure 5.12 - 5.13).

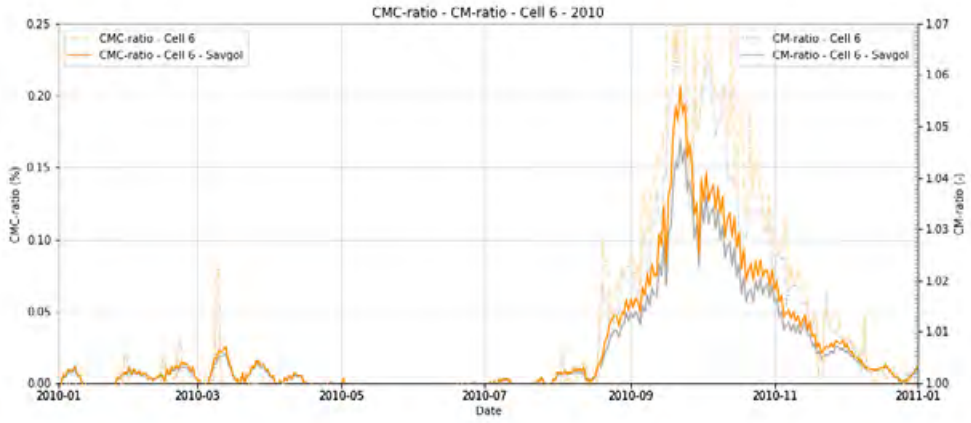

Figure 5.12. CMC-ratio and CM-ratio for cell 6 in 2010. The Spearman's rank indicates a correlation of 0.999245. (own work).

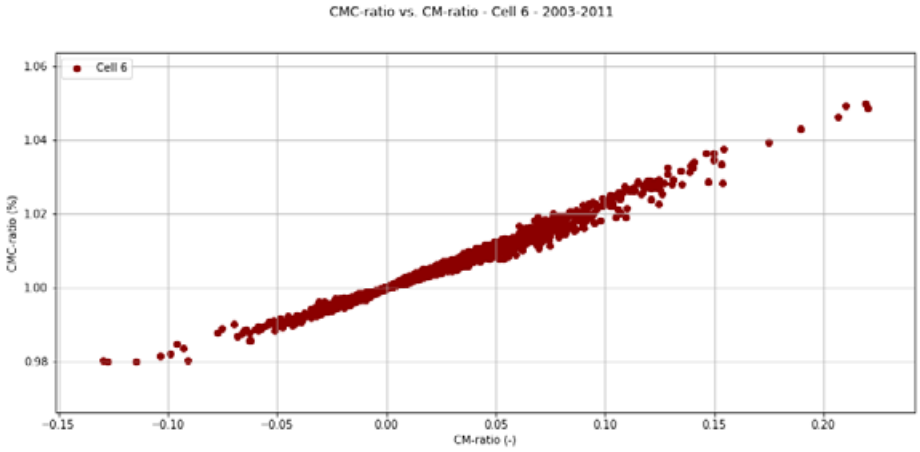

Figure 5.13. Correlation of 99.3% (based on Spearmans rank) between CM-ratio and CMC-ratio for the entire AMSR-E period. (own work).

5.3.2 Location of Measurement and Dry Calibration Cells

Similar to the brightness temperatures, clear differences are visible when changing the location of the cells producing the CMC-ratio. Taking cells 2, 4, 6, 8 and 10 an increasing inundation pattern is visible in 2010, supporting the notion that the CMC-ratio is location dependent. Furthermore, the peak and timing of maximum inundation is increasing and delaying for downstream cells.

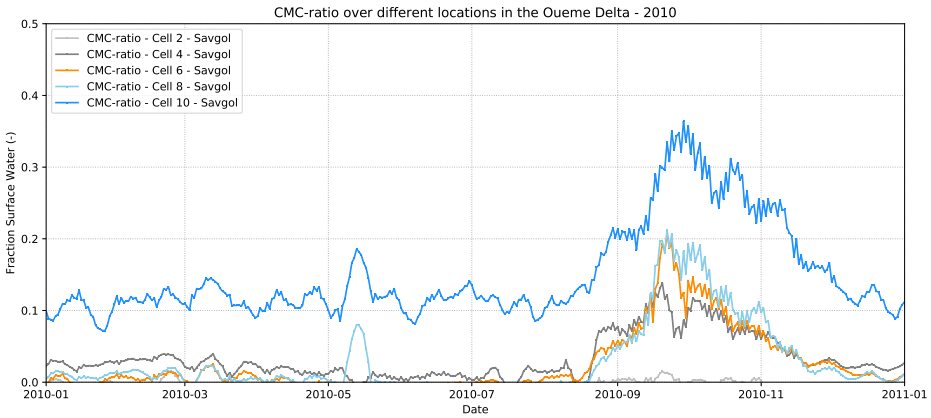

Figure 5.14. CMC-ratio at cell 2, 4, 6, 8 and 10 for 2010 (own work).

5.3.3 Inter-annual variation

Interannual variation of the CMC-ratio is visible in figure 5.15 supporting the notion that the CMC-ratio is time dependent. Years 2003, 2007 and 2010 were years with heavy inundations reported. In 2004 no disaster was reported, but still a significant inundation signal is detected in the inundation season.

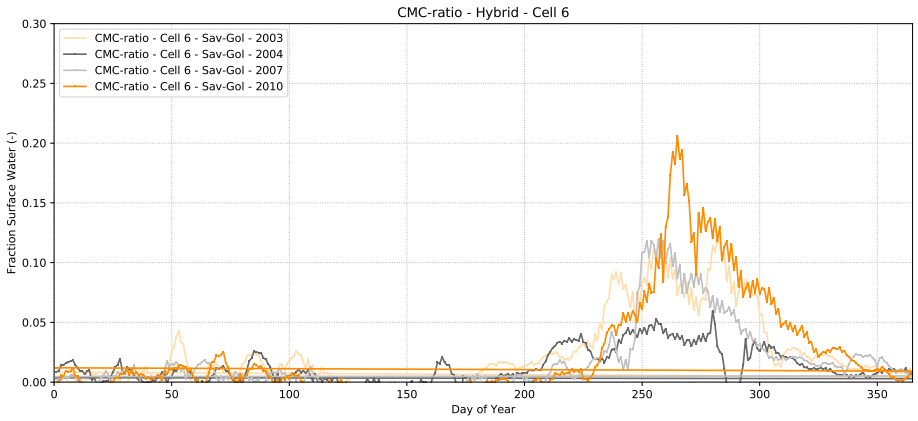

Figure 5.15. CMC-ratio at cell 6 for 2003, 2004, 2007, 2010 (own work).

5.4 Inundation Extent Mapping Model (IEMM)

The baseline method of inundation scale estimation shows a permanent underestimation of the inundation extent, compared to MODIS optical validation. Detailed figures are available in appendix D, a summary of the accuracy of the method is depicted in figure 5.16. Based on the combination of accuracy and standard deviation, the Hybrid scale estimation method is preferable and is therefore selected for further analysis in this research. The Fixed Wet Cell method still underestimates the inundation scale and as of now the full method is not yet able to accurately describe the inundation behaviour. Assuming that the signal error comes from the wet cell, a (i) factor and (ii) correction brightness temperature is found to correct for the permanent offset. Detailed plots of the inundation scale estimation methods can be found in Appendix D.

IEMM Methods			MODIS Validation	Baseline	Hybrid	Fixed Wet	Full - Factor	Full - Offset
Type			NIR-band	Accuracy	Accuracy	Accuracy	Accuracy	Accuracy
Units			Surface water (%)	Surface water (%)	Surface water (%)	Surface water (%)	Surface water (%)	Surface water (%)
Date	Sensor	Cell			TB_W-hybrid = 256.7 K	TB_ W-fixwet = 200.4 K	f_TB_W = 1.29	TB_Offset = 57.0 K
26-9-2003	AMSR-E	6	30.79	23.84	92.68	24.22	91.48	88.20
3-10-2003	AMSR-E	6	27.56	23.11	85.10	21.48	50.47	79.94
28-10-2003	AMSR-E	6	32.21	16.04	89.66	16.89	53.15	53.31
12-9-2007	ASMR-E	6	32.62	29.02	81.48	29.74	94.89	96.13
26-9-2007	ASMR-E	6	28.11	22.15	86.66	22.25	84.89	81.98
30-9-2007	ASMR-E	6	32.02	23.37	91.09	23.01	98.99	92.95
29-9-2010	AMSR-E	6	36.67	29.41	81.27	31.68	99.51	99.51
17-10-2010	AMSR-E	6	29.26	32.10	89.65	29.79	36.67	23.94
20-10-2010	AMSR-E	6	22.05	29.64	92.86	28.80	40.80	63.89
Average	AMSR-E	6		25.41	87.83	25.32	72.32	75.54
Standard Dev.				3.59	4.20	4.64	26.45	23.13

Figure 5.16. Overview of the percentage of surface water and accuracy of the inundation size estimation methods in cell 6 on 9 days in 2003, 2007 and 2010. Comparison between optical validation, the Hybrid method, the Fixed Wet Cell method, Full method - Factor and Full method - Offset. (own work)

5.4.1 Method - Baseline

The unfiltered T_B signal is corrected for missing values and to smoothened with the Savtizky-Golay filter (15 days, 3rd order polynomial) to reduce the signal's noise. The accuracy is low (25.4 % $\pm$ 3.6 %) and constantly underestimates the validated inundation scale. Therefore, alternative methods are considered.

5.4.2 Method - Fixed Wet Cell

The wet cell signal T_{B_W} has limited seasonality and is very noisy. Therefore, the Fixed Wet Cell method takes a constant $T_{B_{W-fixwet}}$. For the entire AMSR-E period this is $200,4K$. Comparing T_{B_W} taken above lake Volta show more constant signals for the 3.125 km cells. Since lake Nokoué is limited in size, taking the T_{B_W} from 3.125 km cells is inevitable, but subsequent downscaling effects might cause noise. In that case it is not possible to obtain a reliable T_B of a fresh water body in the Ouémé catchment. The accuracy of this method is very low: 25.3 % $\pm$ 4.6 %.

5.4.3 Method - Full Model

Relying solely on including other physical processes is not yet possible. Further research on the physical processes and the effect on the Ka-Band signal is required. Two alternatives are considered, the Full-Factor method and the Full-Offset method, each assuming corrections to T_{B_W} are required to improve results, either with a factor, or a constant offset. These corrections are based on validation values of MODIS optical imagery. Increasing T_{B_W} with a factor of 1.29 (f_{TB_W}) would result in an accuracy 72.3 % $\pm$ 26.4 % for the ASMR-E period. The Full-Offset method (increasing T_{B_W} with $T_{B_{W-Offset}}$ = 57.0 K) performs slightly better: 75.5 % $\pm$ 23.1 %. Both methods have a very high standard deviation, caused by the noise of T_{B_W}.

5.4.4 Method - Hybrid

The Hybrid method uses a constant and 'artificial' $T_{B_{W-hybrid}}$ of 256.7 K $\pm$ 3.46 K for AMSR-E, based on MODIS optical validation. The Hybrid method performs best on accuracy: 87.8 % $\pm$ 4.2 %. This method does not use any T_{B_W} and is thereby also suited for locations without (large) water bodies. This research selects the hybrid method as preferred method of the IEMM.

Testing the Hybrid method for other cells shows good results for cells 4, 6, 8 and 10 and poor results for the other cells, which is related to the average surface water fraction (Figure 5.17). On the validation days, cell 4 has an average surface water fraction of 0.25 with an accuracy of 83 %, increasing to 0.42 and 95 % for cell 10 respectively. The standard deviation decreases for increasing surface water fraction, but note that this is biased because the accuracy is more sensitive to deviations from smaller surface water fractions. The wet hybrid calibration cell temperature ($T_{B_{W-Hybrid}}$) shows a decreasing brightness temperature for an increasing surface water percentage. More detailed schemes on the Hybrid method can be found in appendix D.

5.4.5 Inundation Mapping

The size of inundation estimated by the CMC-ratio is subsequently allocated to designated pixels of an underlying elevation map (Figure 5.20), but mapping results (compared to MODIS validation inundation extent (Figure 5.18)) are equivocal and no clear conclusion for a preference of an elevation map or mapping method can be drawn. The result of the inundation extent estimation, in terms of accuracy and (false positive and false negative) depends on inundation size, natural slope in the measurement cell, non-inundated tributaries, local depressions and the quality (i.e.

CMC - Hybrid					
	Type	CMC	Accuracy	SD	TB_W-hybrid
	Unit	%	%	%	K
Sensor	Cell	average	average	average	
AMSR-E	1	1.01	-154.59	141.85	303.95
AMSR-E	2	6.13	-27.75	67.69	285.42
AMSR-E	3	5.93	15.11	67.69	261.61
AMSR-E	4	25.04	83.51	8.39	256.63
AMSR-E	5	2.96	-10.84	80.48	246.24
AMSR-E	6	29.34	87.83	4.20	256.73
AMSR-E	8	35.32	89.21	6.35	256.83
AMSR-E	10	41.53	95.13	2.70	233.87

Figure 5.17. Overview of CMC-Hybrid method on 9 validation days ('03,'07,'10) and the accuracy, standard deviation and required wet hybrid calibration cell per cell. Cells with satisfactory accuracy are highlighted in orange. (own work).

accuracy and spatial resolution) of the validation method. These results are further discussed in the next chapter. Detailed mapping results of individual cells can be found in Appendix E.

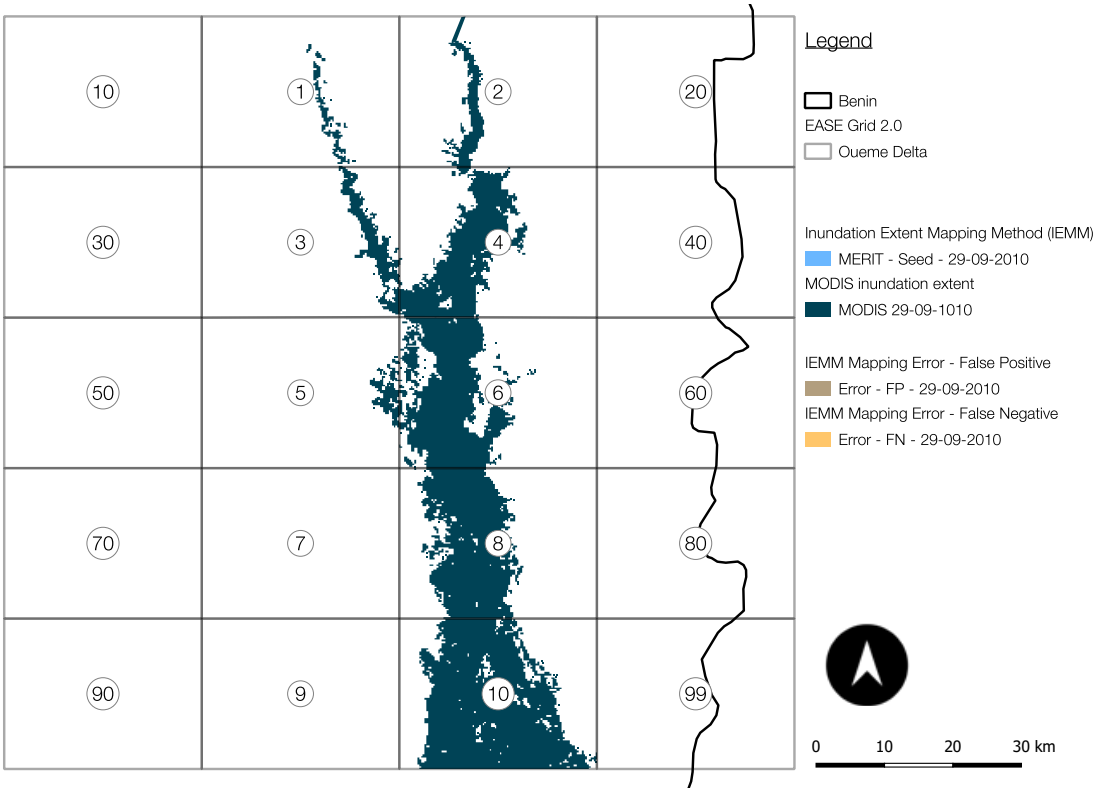

Figure 5.18. MODIS validation inunation extent on 29-09-2010, used as input to test the mapping methods (own work).

Longitude	Latitude	GPS accuracy (m)	h (MERIT) (m)	h (HAND) (m)
6,910,565	2,448,867	4.4	8.38	2.96
6,909,213	2,450,992	5.0	8.47	3.05
6,907,927	2,448,635	4.9	8.77	3.35
7,015,303	2,425,577	4.6	13.36	4.90
7,046,933	2,440,137	4.5	10.78	2.39
Mean (m)		4.7	9.95	3.33
Variance (m)		0.1	4.59	0.89
Standard Deviation (m)		0.3	2.14	0.94

Figure 5.19. ODK-collect locations taken in Cell 6 on 21-09-2018 at the edge of the inundation extent. Note that the GPS accuracy refers to a horizontal spatial accuracy, whereas the MERIT DEM and HAND columns refer to the vertical accuracy. (own work).

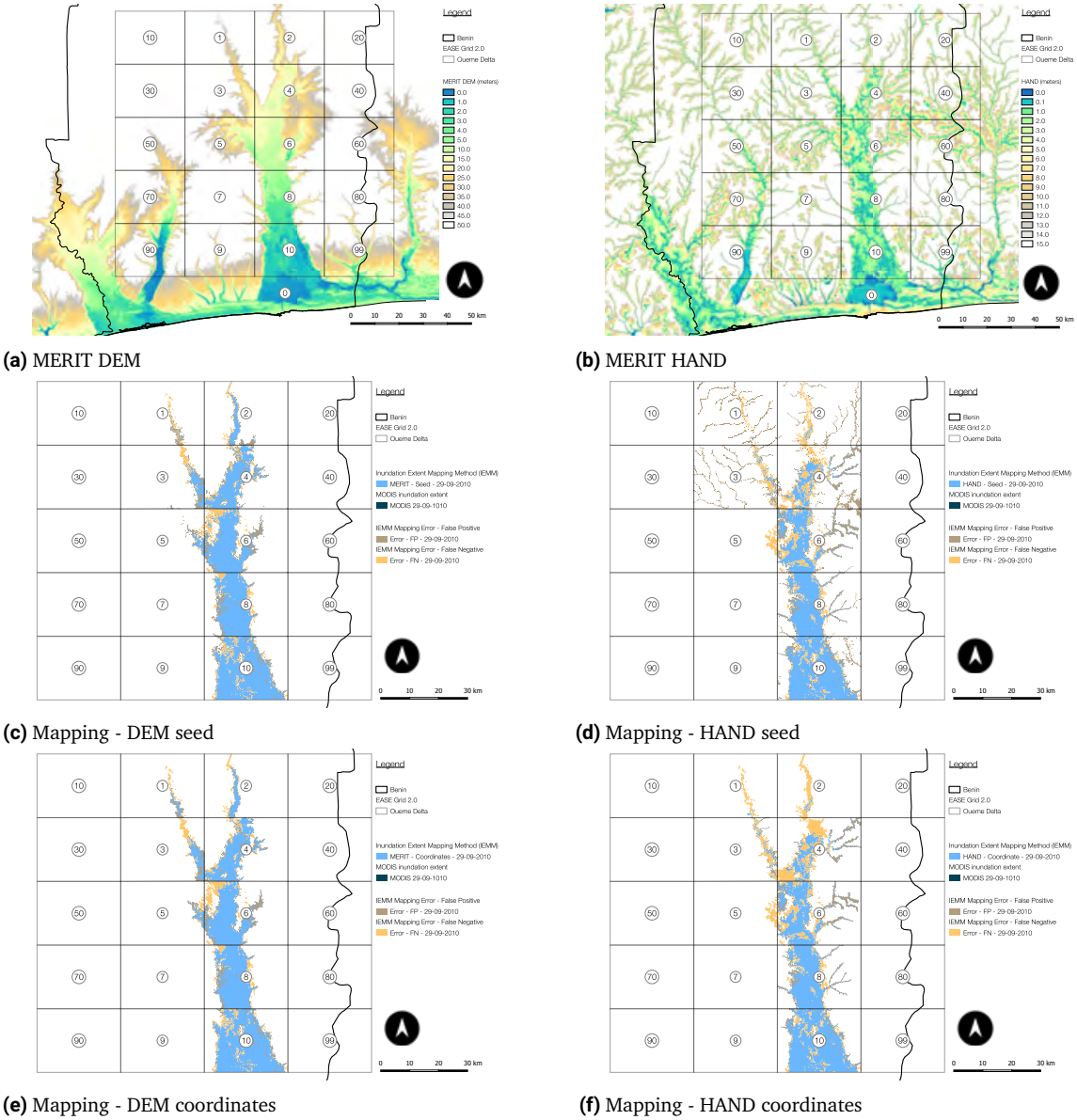

(a) MERIT DEM

(b) MERIT HAND

(c) Mapping - DEM seed

(d) Mapping - HAND seed

(e) Mapping - DEM coordinates

(f) Mapping - HAND coordinates

Figure 5.20. Visualisation of the different mapping methods and the false positive and false negative errors, on two different elevation maps: (a) MERIT DEM and (b) the HAND derived from the MERIT DEM. (c) and (d) show the result without contiguity constraints and (e), (f) depict the result when contiguity constraints based on (manually) given coordinates are included. (own work)

5.5 Time Series Analysis

The IEMM is set up with the Hybrid Method for the AMSR-E period. Inundation stages, start and duration are visible. Clear seasonality is visible in multi-annual plots, also in comparison with discharge at the Bonou station (figure 5.25). Lead time and threshold inundation levels of extreme inundation can be derived during the AMSR-E period (Figure 5.23, 5.26). However, for trend analysis of extreme inundations the time series is too short. Merging the entire T_B datasets directly is challenging due to slight changes in the radiometer's bandwidth, frequency and inclination angle, but from 1996 a relatively stable signal is available (Figure 5.27).

5.5.1 Inundation vs. Discharge

Comparing the CMC-ratio to discharge data shows different but relevant information when studying inundation patterns. The only discharge dataset available is the one at Bonou (located in cell 6) from 1952 – 2011. In 2010, the CMC-ratio does well in presenting clear patterns of inundation, whereas these events are less visible in the discharge data (Figure 5.21). Figure 5.22 confirms that the sensitivity of higher discharges declines, whereas the sensitivity of higher inundations increases and the tipping point lies approximately around 800 m^3/s, which is the 'emergency threshold' discharge according to SAP. This can be considered an advantage over conventional discharge data when interested in inundations, but also extreme discharges. The stages of inundation found in the CMC-ratio, resemble the discharge thresholds determined by the Flood Early Warning System (SAP) (Figure 5.23). These stages seem to relate to different phases of inundation, such as bank-full discharge, floodplain inundation and bank over-topping. More discharge data is required to investigate if this behaviour is consistent throughout the entire catchment. The timing of the start of inundation and the time span of maximum inundation matches the time span found by news and disaster reports. According to news and disaster reports, in 2010 inundations occurred between September 20th and October 25th (Smith, 2010). The CMC-ratio of location 6 reports extreme inundations for Bonou ($Q > 800m^3/s$) between September 17th and October 17th 2010. Further temporal comparison is impossible due to the lack of discharge data and the lack of detailed reports about inundation developments in other years. Lead time of peak inundations can be derived from upstream and downstream responses (Figure 5.26), but validation of lag time requires more detailed data, such as discharge datasets. Scatter-plots of discharge and inundation over time show that for increasing discharge, inundation becomes more sensitive, whereas discharge measurements face limitations (Figure 5.22).

5.5.2 Multi-annual Analysis

Over the AMSR-E period (2003-2011) the following analyses have been carried out: (i) threshold analysis, based on the notion that stability of the inundation analysis increases over time with the CMC-ratio. This is done both for number of days and annual maxima (Figure 5.24). In the first analysis, 2008 has the most days exceeding the emergency threshold and was longer than 2010. The second analysis shows that the total inundation in 2010 was larger. Based on the reported impact in which 2010 was a disastrous year, this would indicate that the size of the inundation extent has a larger influence in terms of impact than only the number of days of extreme inundations.

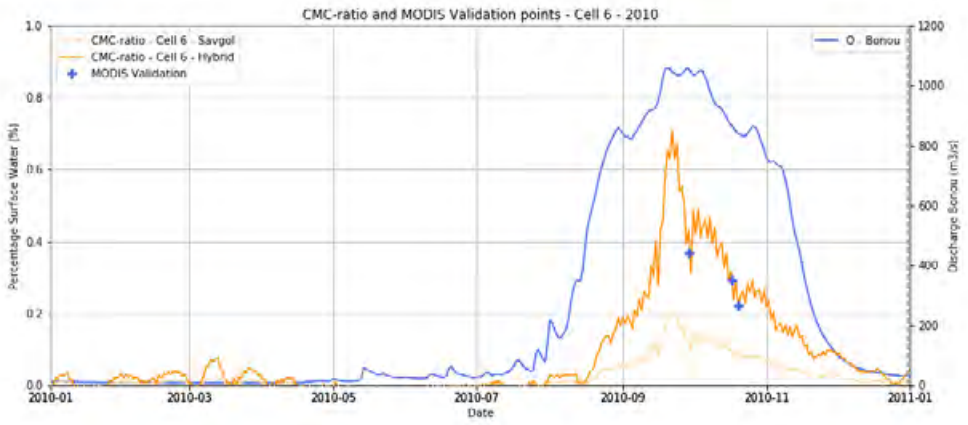

Figure 5.21. CMC-ratio for cell 6 and discharge at the Bonou station for 2010. Notice the sharp response in r_{CMC}, possibly corresponding with different stages of inundations (bank-full discharge, overtopping) (own work).

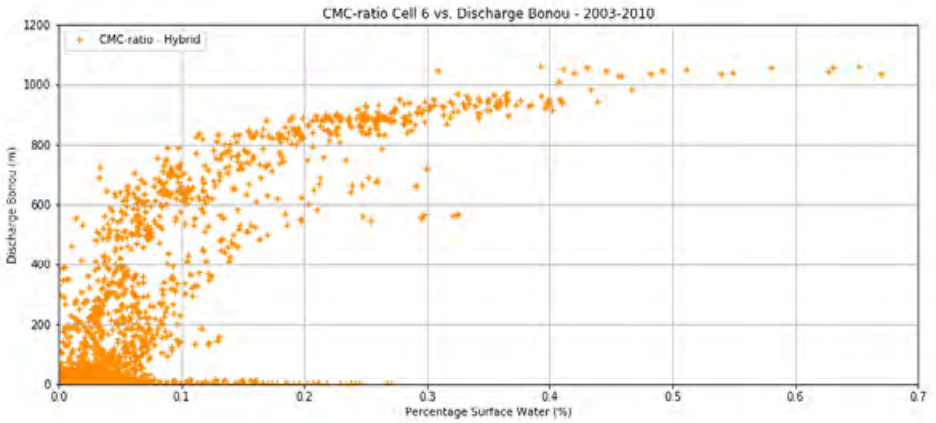

Figure 5.22. Inundation versus discharge showing that around 800 m^3/s discharge becomes less sensitive and inundation becomes more sensitive (own work).

Secondly a (ii) maximum lead time analysis is carried out to investigate the downstream propagation time of inundation maxima (Figure 5.26). For years with a clear single annual inundation peak this results in satisfactory results for cells 6, 8 and 10 and provides valuable insights on the inundation patterns in the delta, despite the little information on discharge available.

Comparison of inundation timing - CMC-hybrid and Q_Bonou - Cell 6 - AMSR-E										
	Year	2003	2004	2005	2006	2007	2008	2009	2010	Standard Deviation
CMC_hybrid Q>550	%	5,07	9,93	24,82		9,60	11,13		3,78	7,50
CMC_hybrid Q>700	%	9,04	13,78			6,17	14,49		11,90	3,46
CMC_hybrid Q>800	%	13,95				11,19	14,55		11,72	1,65
Q_max	m3/s	971,50	781,40	566,00		949,80	960,30		1060,00	
DOY Q_max	DOY	282	249	289		258	279		263	
CMC_max	%	36,59	18,04	32,56	13,45	40,82	41,00	27,17	70,84	
DOY CMC_max	DOY	282	256	288	260	257	275	255	265	
Difference DOY	DOY	0	-7	1		1	4		-2	3,73

Figure 5.23. Overview of a comparison of the $r_{CMC-hybrid}$ method and discharge at the Bonou station for the ASMR-E period. The first rows describe what $r_{CMC-hybrid}$ is on the day that Q exceeds the thresholds defined by SAP (i.e. 550, 700 and 800 m^3/s). Notice how for increasing warning levels, $r_{CMC-hybrid}$ becomes more accurate. The second part describes how many days the annual maxima of Q and $r_{CMC-hybrid}$ are apart. (own work).

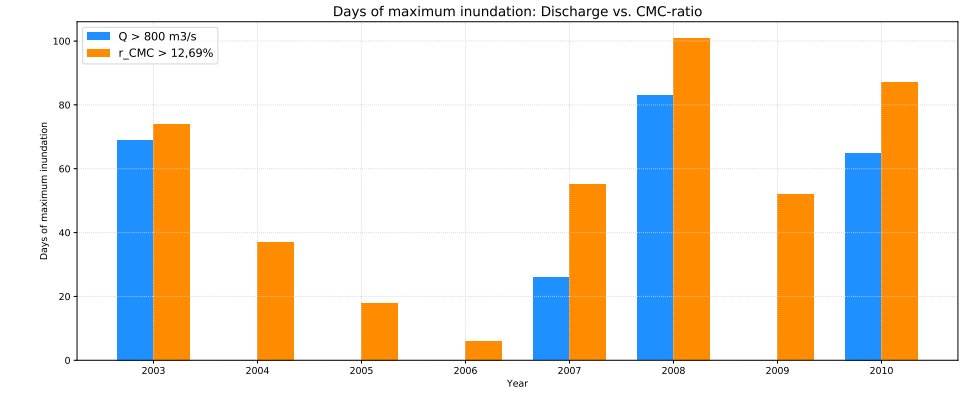

(a)

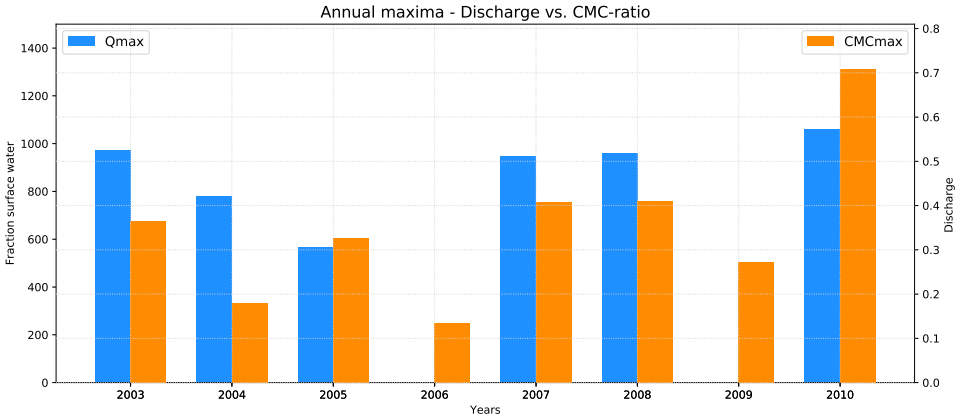

(b)

Figure 5.24. Maximum inundation and discharge analysis for (a) number of days exceeding the emergency threshold (Q = 800 $^3/s$, which corresponds to $r_{CMC} > 12{,}69$ %) and (b) annual maxima (own work)

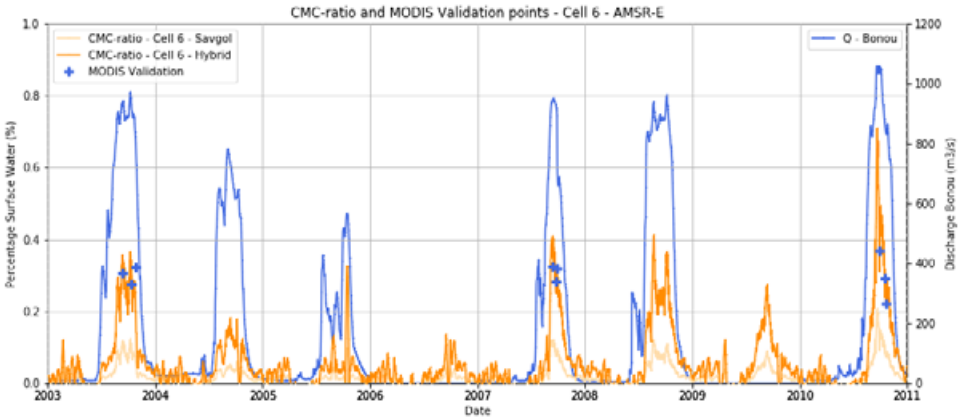

Figure 5.25. CMC-ratio over AMSR-E period (2003-2011) comparison with discharge and MODIS validation points. (own work)

Lead time per cell					
Cell	2	4	6	8	10
Year		days			
2003		180	0	-25	37
2004		202	23	-24	2
2005		47	-2	-47	-106
2006		-235	199	14	-2
2007		162	0	2	0
2008		81	3	4	5
2009		199	2	2	5
2010		209	2	0	7
mean (days)		105.63	28.38	-9.25	-6.50
variance (days)		22495.98	4815.70	420.79	1767.71
SD (days)		149.99	69.40	20.51	42.04

(a)

Lead time per cell					
Cell	2	4	6	8	10
Year		days			
2003					
2004					
2005					
2006					
2007		162	0	2	0
2008		81	3	4	5
2009		199	2	2	5
2010		209	2	0	7
mean (days)		81.38	0.88	1.00	2.13
variance (days)		3378.92	1.58	2.67	8.92
SD (days)		58.13	1.26	1.63	2.99

(b)

Figure 5.26. (a) Lead time showing the number of days of CMC-ratio maxima compared to the upstream cell. So, in 2010 there were 2 days between the CMC-ratio maximum in cell 4 and cell 6. Cell 2 is not possible because it has no upstream cells. (b) Removing years with multiple inundation peaks per year results in more consistent values. Lead time between cell 2 and 4 is unclear, but improves further downstream. (own work)

5.5.3 Multi-system Analysis

Changes in sensor and satellite settings cause inter-system changes in the brightness temperature which need to be accounted for prior to conducting inter-system analysis. From 1996 - 2016 a relatively stable signal is found which is used for trend analysis (Figure 5.27). In 2010 multi-system analysis shows the performance of other systems (Figure 5.28a). The required hybrid wet calibration temperature is derived from comparitive analysis in 2010 and is listed in figure 5.17. The years 2003 and 2007 are used for correcting the brightness temperatures and subsequent Hybrid CMC-ratio because these are the only two validated years with data of all three satelilte missions. For cell 6 the brightness temperatures of DMSP F-13 and F-15 are corrected for the mean (figure 5.30) and the subsequent CMC-ratio is corrected for the mean, standard deviation and variance (Figure 5.31 - 5.28b). DMSP F-13 shows higher correlations with AMSR-E than DMSP F-15. The resulting fused dataset from 1996 - 2016 is analysed for trends in annual maxima, but no clear trend is found (Figure 5.32). Discharge rates in 1998 and 1999 exceeded the 2010 rate, despite reported record inundations and disasters in the latter. Additional time series shows that for an average year, in the months August, September and October inundations occurs, as the monthly mean surface water fraction exceeds 0.11-0.12 (which as mentioned earlier corresponds to the emergency threshold of 800 m^3/s) (Figure 5.33a). Return periods of 1, 10 and 100 years correspond to approximately 0.20, 0.45 and 0.65 surface water fraction (Figure 5.33c). These surface water fractions can subsequently be mapped on MERIT HAND and DEM elevation maps to give a spatial estimate (Figure 5.34 and 5.35, respectively). Note that the maximum inundation in 2010 approximately corresponds to an inundation of 100-year return period. Comparing time series from 1996 - 2006 with 2006 - 2016 does not show a clear trend in maxima of inundations, Figure note that the time-frames are very short (10 years, i.e. 10 inundation seasons) and the arbitrarily chosen bin size has a significant effect on the outcome (figure 5.33d - 5.33f).

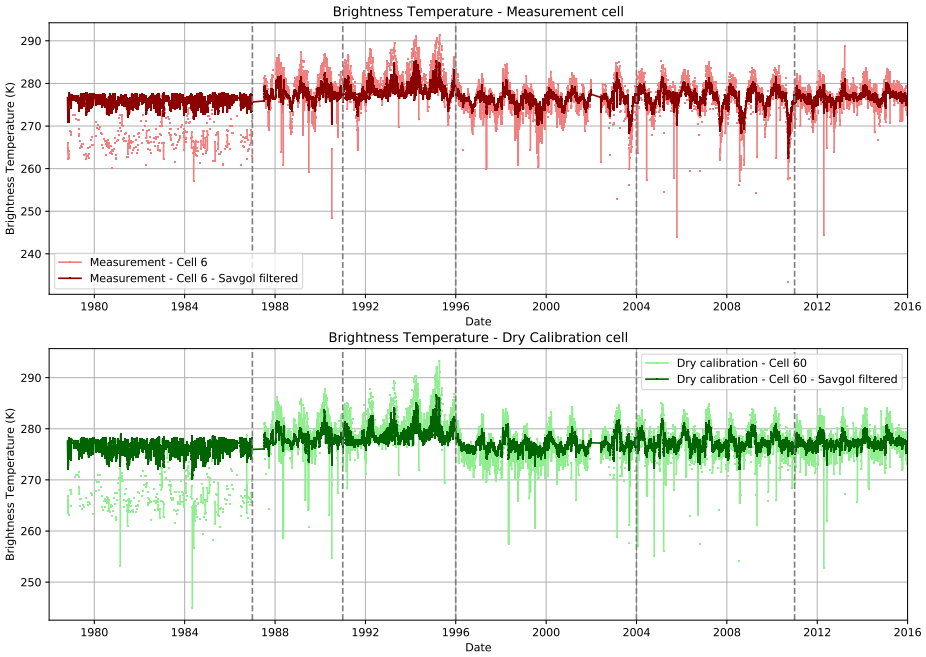

(a)

Figure 5.27. Brightness temperatures for measurement cell 6 and dry calibration cell 60 for the entire MEaSUREs dataset (1978-2017). The grey vertical lines indicate start and end periods of missions (own work)

Multi-System - Hybrid Wet Calibration Cell - Cell 6 - 2010				
Sensor	Cell	Year	Accuracy	TB_W_Hybrid
			-	K
AMSR-E	6	2010	0.89	256.73
DMSP-F13	6	2010	0.72	264.90
DMSP-F15	6	2010	0.75	267.18
DMSP-F18	6	2010	0.81	265.44

(a)

Correction DMSP F-13 & F-15 vs. AMSR-E - Cell 6 - 2003 - 2007						
	DMSP-F13			DMSP-F15		
Brightness Temperature	mean (K)	std (K)	var (K)	mean (K)	std (K)	var (K)
TB_M_c6_savgol	1.07	0.93	4.11	-3.49	0.38	1.90
TB_D_c6_savgol	1.43	0.48	1.25	-3.24	-0.30	-1.00
CMC-ratio	mean (-)	std (-)	var (-)	mean (-)	std (-)	var (-)
CMC-ratio - Hybrid	-0.03	-0.01	0.00	-0.02	0.00	0.00
CMC-ratio percentiles	surface water fraction (-)			surface water fraction (-)		
CMC-ratio - 90th percentile	-0.02			0.00		
CMC-ratio - 90th percentile	-0.05			-0.02		
CMC-ratio - 90th percentile	-0.07			-0.03		
Correlation AMSR-E	0.82			0.79		

(b)

Figure 5.28. Overview of (a) multi-system comparison of required artificial wet calibration temperatures of cell 6 in 2010 and (b) corrections for brightness temperatures and hybrid CMC-ratio for the DMSP F-13 and F-15 methods in 2003 and 2007. (own work).

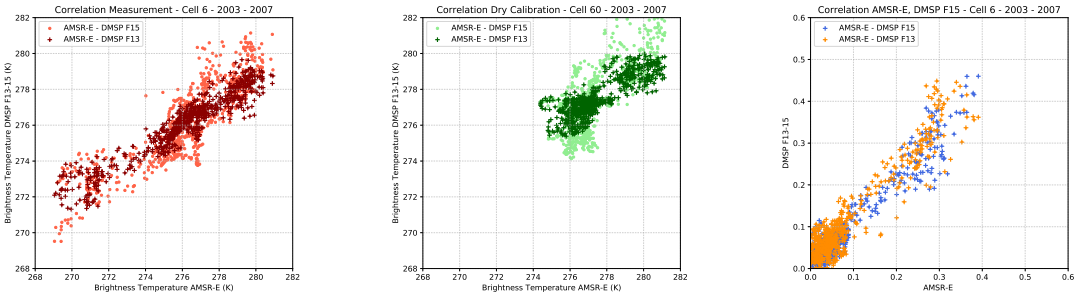

(a) Correlation T_B - Measurement **(b)** Correlation T_B - Dry Calibration **(c)** CMC-ratio - Hybrid

Figure 5.29. Correlation between AMSR-E and DMSP F13-F15 in terms of (a) measurement (cell 6) brightness temperature, (b) dry calibration (cell 60) brightness temperature and (c) Hybrid CMC-ratio (own work).

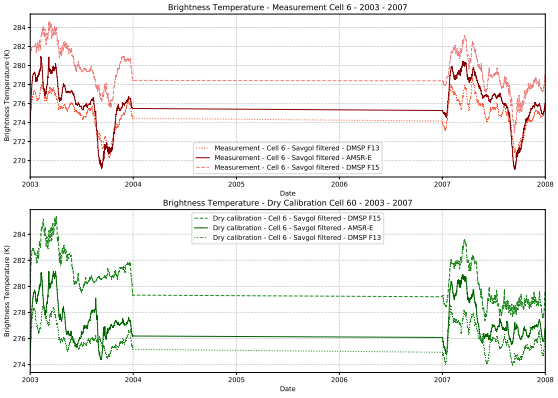

(a) Original T_B signal for data fusion in 2003 and 2007

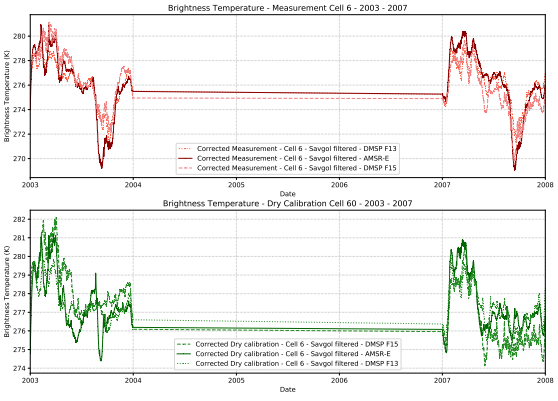

(b) Corrected T_B signal for data fusion in 2003 and 2007

Figure 5.30. Brightness Temperatures of (a) the orginal incoming signal from DMSP F-13-15 and AMSR-E and (b) the mean corrected version. (own work)

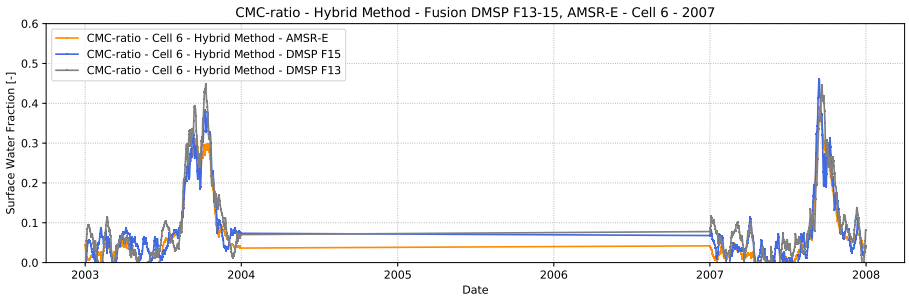

(a) Original Hybrid CMC-ratio 2003 - 2007

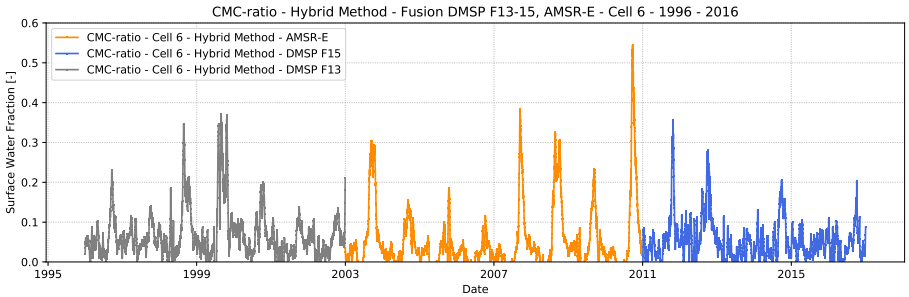

(b) Original Hybrid CMC-ratio 1996 - 2016

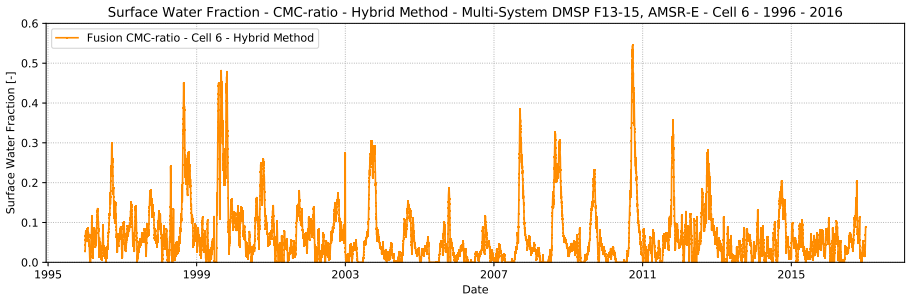

(c) Corrected Hybrid CMC-ratio 1996 - 2016

Figure 5.31. Correcting the Hybrid CMC-ratio in 2003 and 2007 (a) and afterwards for the entire period of satellite coverage (b) resulting in the final fused dataset (c) (own work)

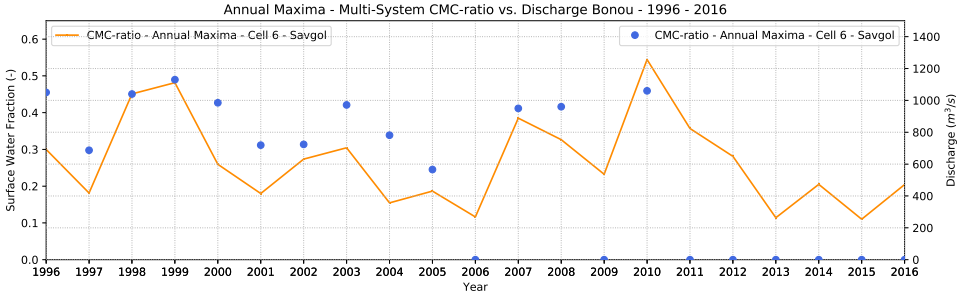

Figure 5.32. Annual maxima in discharge and Hybrid CMC-ratio of the fused dataset. (own work)

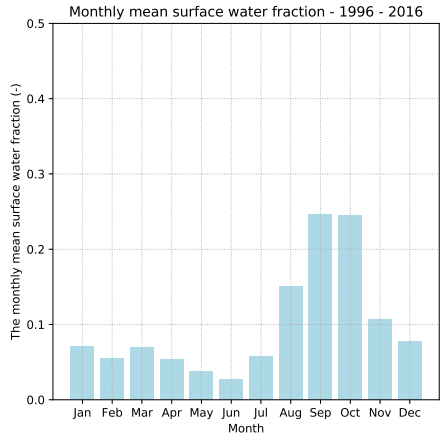

(a)

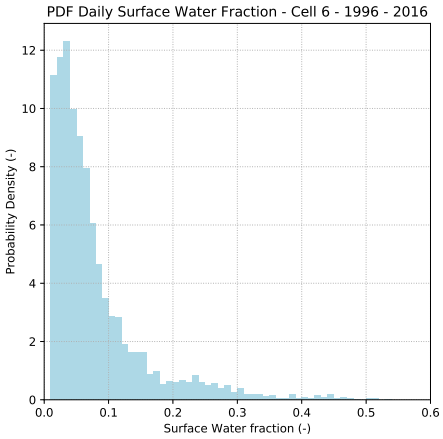

(b)

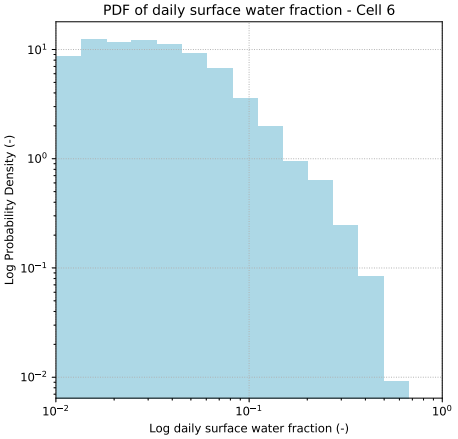

(c)

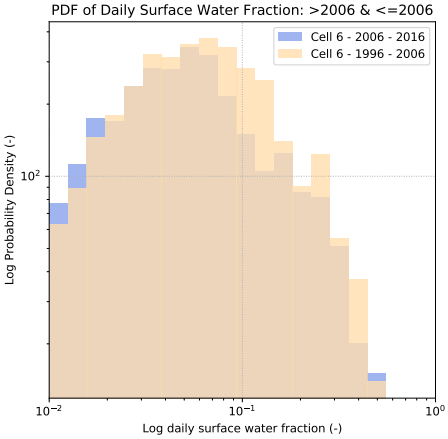

(d) 25% bin size increase per bin

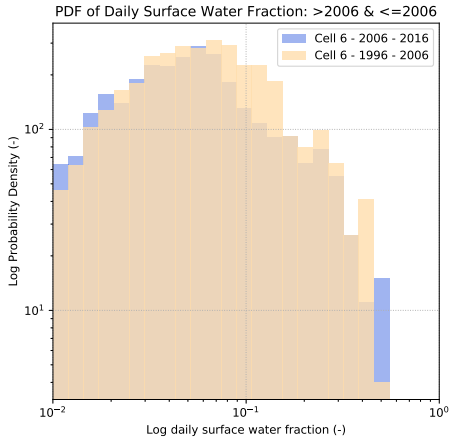

(e) 20% bin size increase per bin

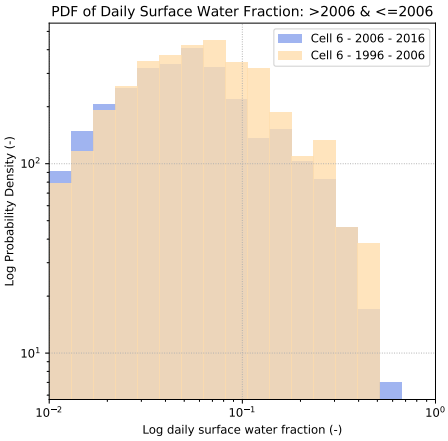

(f) 30% bin size increase per bin

Figure 5.33. Time series analysis of Hybrid CMC-ratio in cell 6 between 1996 and 2016 depicting the (a) monthly mean surface water fraction. In stead of using a probability distribution function on a (b) linear scale, a (c) log-log scale is used, clearly showing the return periods for every 1, 10, 100 years. Comparing trends of 1996-2006 vs. 2006 - 2016 (d) shows ambiguous results due to the short time time-frame of data available, but no clear increase in maximum inundations is found. Furthermore the (arbitrarily chosen) bin size has a significant effect on the outcome (e) (f).(own work)

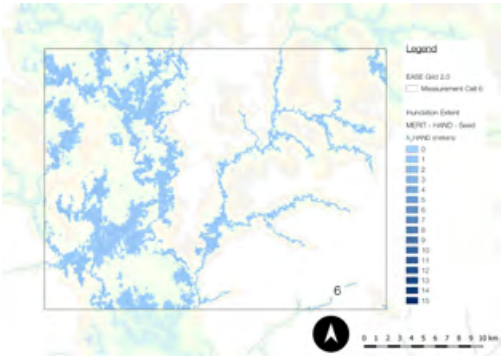

(a) HAND - 1-year return period - 1.37 m - Seed mapping

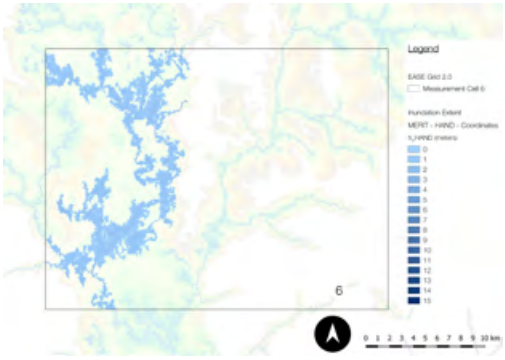

(b) HAND - 1-year return period - 1.37 m - Coordinates

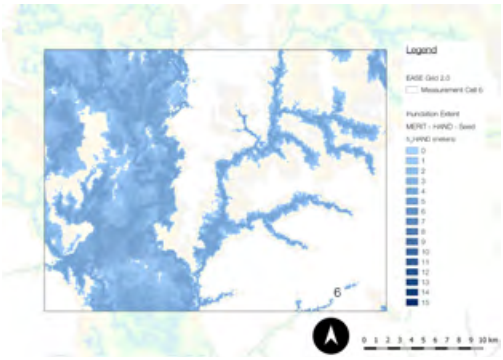

(c) HAND - 10-year return period - 4.59 m - Seed

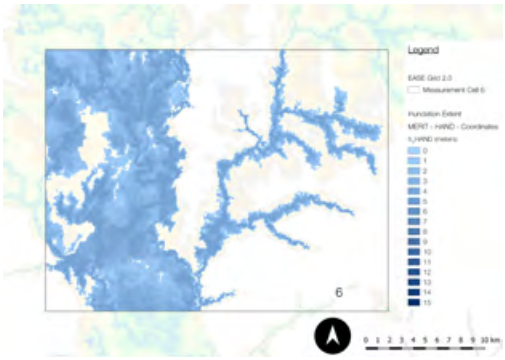

(d) HAND - 10-year return period - 4.59 m - Coordinates

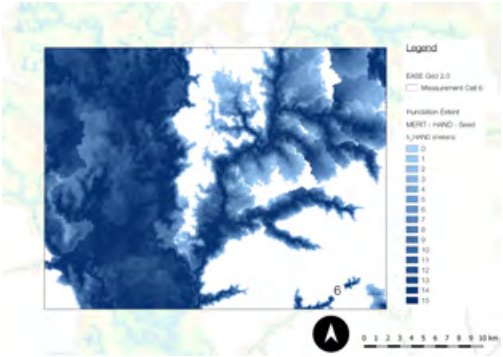

(e) HAND - 100-year return period - 15.24 m - Seed

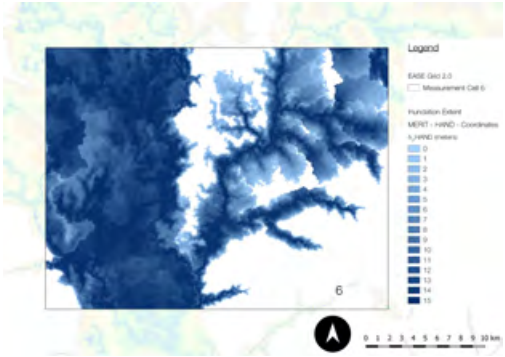

(f) HAND - 100-yr return period - 15.24 m - Coordinates

Figure 5.34. Estimated (a, b) 1, (c, d) 10 and (e, f) 100 year return period inundation extents, based on MERIT HAND elevation map and 'seed' (a, c, e) and 'coordinates' (b, d, f) mapping techniques.(own work)

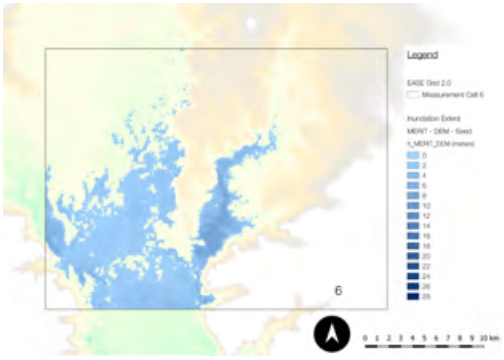

(a) DEM - 1-year return period - 10.08 m - Seed

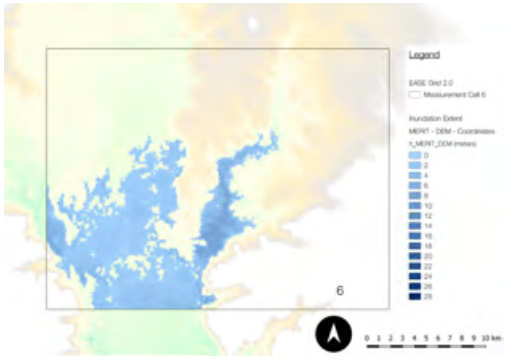

(b) DEM - 1-year return period - 10.08 m - Coordinates

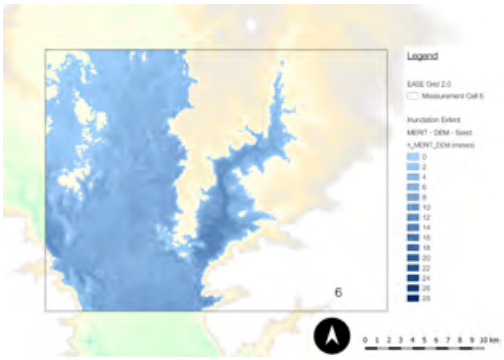

(c) DEM - 10-year return period - 15.45 m - Seed

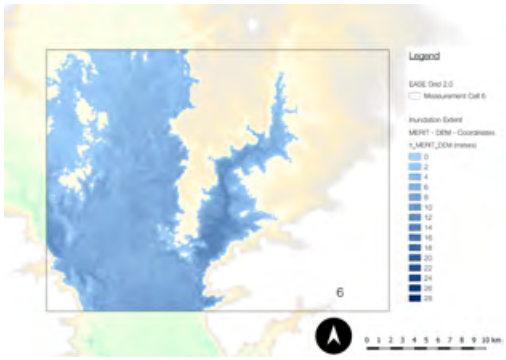

(d) DEM - 10-year return period - 15.45 m - Coordinates

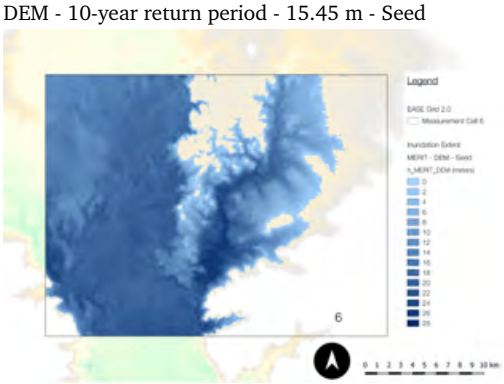

(e) DEM - 100-year return period - 28.43 m - Seed

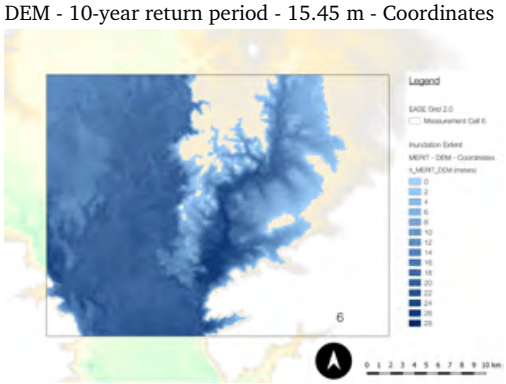

(f) DEM - 100-year return period - 28.43 m - Coordinates

Figure 5.35. Estimated (a, b) 1, (c, d) 10 and (e, f) 100 year return period inundation extents, based on MERIT DEM elevation map and 'seed' (a, c, e) and 'coordinates' (b, d, f) mapping techniques.(own work)

5.6 Accounting Factors

The research is based on the notion that precipitation caused by the African Monsoon causes fluvial inundations and that when these inundations take place in the delta, local rainfall (causing pluvial precipitation) does not play a role. Figure 5.36a supports this hypothesis and therefore additional trend analyses with rainfall stations in the middle and northern catchment have been carried out based on daily rainfall (figure 5.37). The mean rainfall still shows a slight bi-model annual pattern due to the various stations included in the analysis (although stations in the delta are excluded). The normal PDF tells little about extreme precipitation, but the log-log representation gives a better idea of the probability of extreme rainfall. Conducting this analysis for rainfall from 1983 - 1999 and 2000 - 2017 (both 17 years) shows that daily rainfall decreased over the past years, when comparing daily rainfall extremes before 2000 and after 2000. This also means that, the PDF of extreme daily rainfall has changed. Manual comparisons with PDF's before and after 2000 shows that the former should be adjusted with a factor 0,9 approximately.

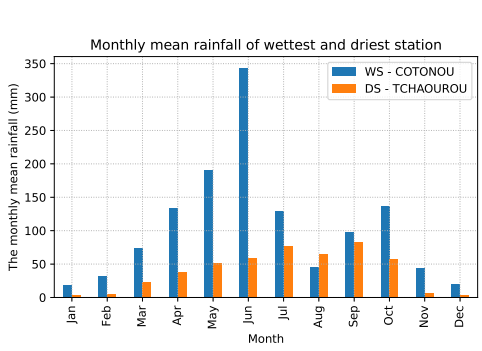

(a) Monthly mean rainfall (own work)

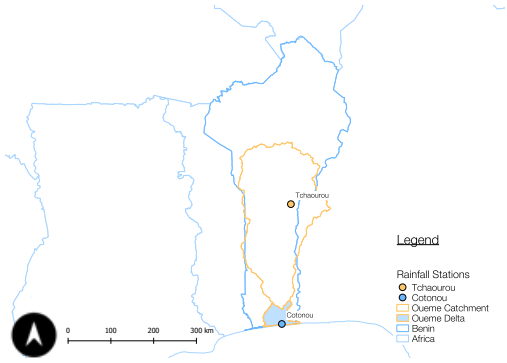

(b) Rainfall stations Tchaourou and Cotonou (own work)

Figure 5.36. Monthly mean rainfall of the wettest and driest station in the Ouémé Delta, clearly distinguishing the different rainfall regimes between the Northern and Southern Ouémé catchment. (own work)

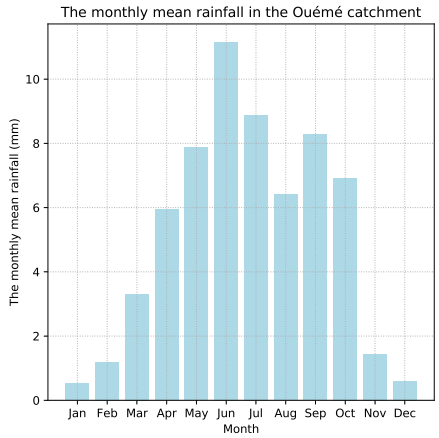

(a) Monthly mean rainfall

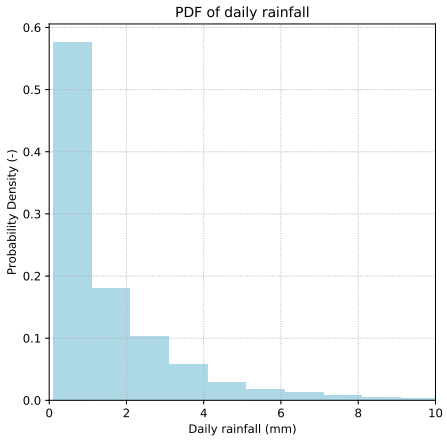

(b) PDF of daily rainfall

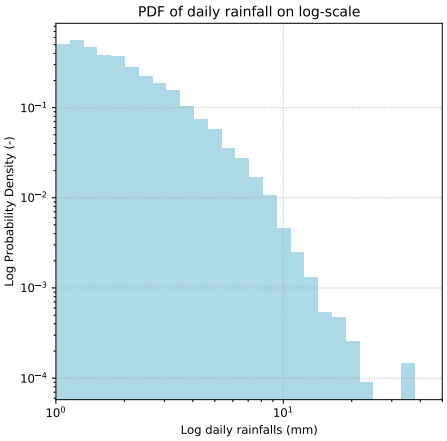

(c) PDF on log-log scale

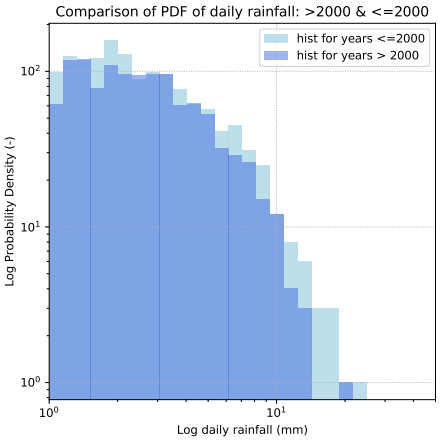

(d) Comparison year >2000<

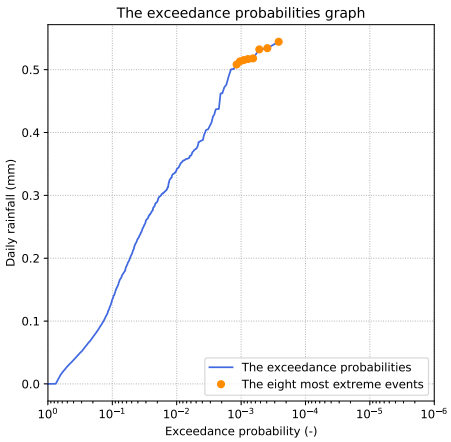

(e) Exceedance probability

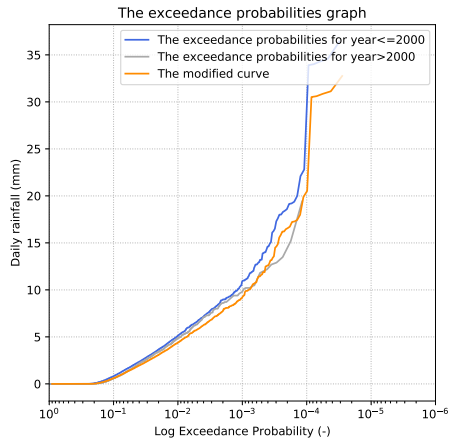

(f) Change in exceedance probability

Figure 5.37. Extreme rainfall analysis for middle and upper Ouémé catchment. (own work)

5.7 Impact

Impact in terms of affected people and deaths caused by fluvial inundations show that the presence of population has had a (larger) influence than the occurrence of the inundation events itself.

5.7.1 Disasters

The EM-DAT database reported 183 deaths and more than 2.7 million affected citizens in the middle and southern part of Benin as a result of floods (floods and inundations are used interchangeably here) between 1970 and 2018. Figure 5.39 shows that locations 2, 4, 6, 8 and 10 are located in flood prone areas. A full list of EM-DAT registered disasters and a more detailed overview of impact of the 2010 flood event is presented in Appendix F. Despite the relative sparsely population density, the inner delta is susceptible to inundations, especially within cell 2 and 4. Furthermore the towns Sô-Ava and Aguégués are susceptible to inundations, located right above lake Nokoué and lacking the infrastructure of a larger city like Cotonou. Although Cotonou, Abomey-Calavi and Porto Novo are not located within any of the cells, these cities are reportedly more susceptible to pluvial inundation, whereas fluvial inundation has little impact.

5.7.2 Population Growth

Population growth in the study area occurred especially in cell 10, where parts of the urban agglomeration of the southern cities are located. Two noteworthy towns are Sô-Ava and Aguégués, which have been repeatedly reported in disaster reports (figure 5.38c). This is in also visible in earlier chapters in figure 2.5.

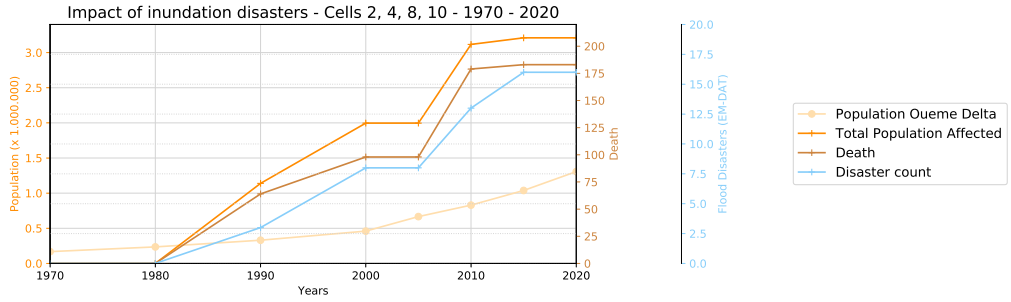

(a)

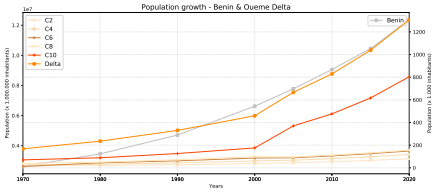

(b) Population growth

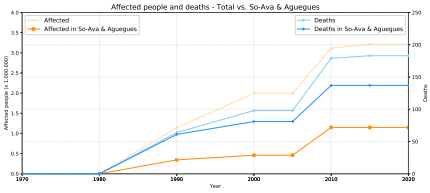

(c) Impact Sô-Ava & Aguégués

Figure 5.38. (a) Impact of inundations in terms of disaster count, population growth, affected people and deaths. (b) Population growth in Benin, and Cell 2, 4, 6, 8, 10. (c) Impact of all inundation disasters and the ones hitting Sô-Ava and Aguégués (own work)

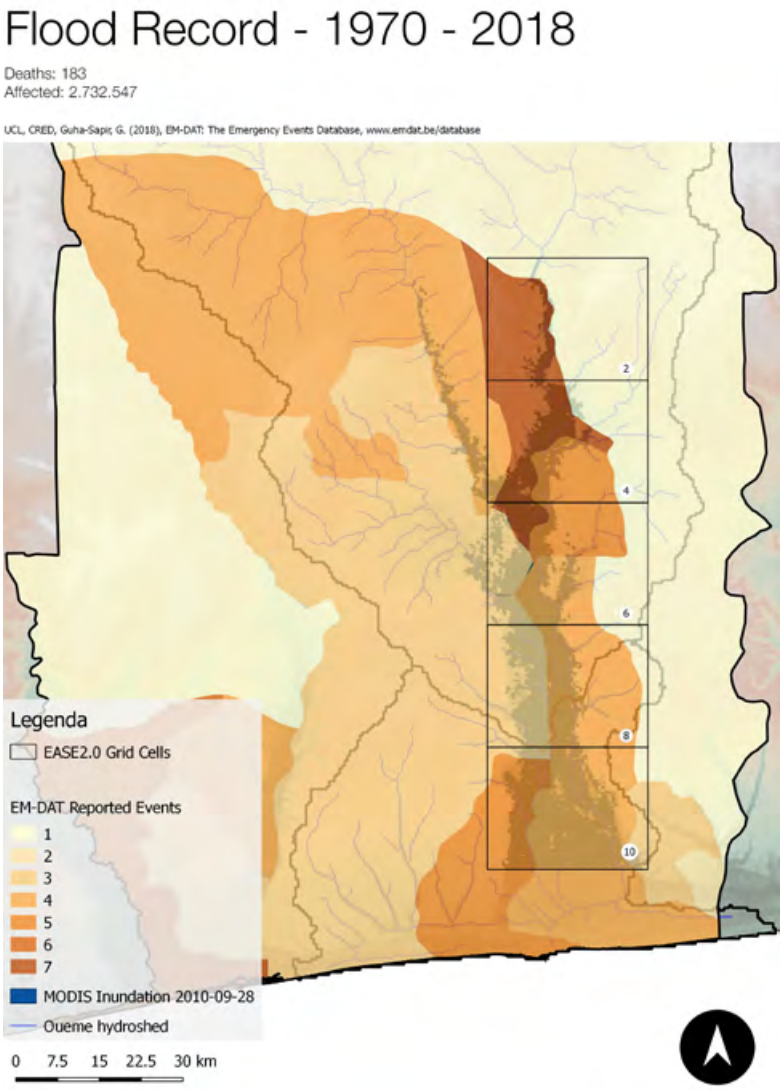

Figure 5.39. Years with reported flood events by the Emergency Events Database between 1970 and 2018 (Universite catholoique de Louvain (UCL) et al., 2018).

Discussion

6

This section interprets the results presented in the previous chapter and discusses shortcomings and limitations of the current research. The method developed to examine inundation behaviour (IEMM) is to a large extent suited to detect, estimate and allocate inundation extent. In doing so, it also directly contributes to the needs of locals: providing information on inundation extent and timing of inundations, making the research approach valid. Nevertheless, some results were unexpected due to data, method or location dependent circumstances.

6.1 Wet Calibration Cell

The wet calibration cell (cell 0) was added in this research to scale inundation patterns and thereby enabling inundation size estimations. However, the brightness temperature obtained from the largest fresh water body in this region (lake Nokoué) produced more noise than expected. This also resulted in the errors in the inundation scale estimations of the baseline method, and the full method. Two alternatives (full-factor and full-offset) aimed to account for this error by including a certain artificial factor or brightness temperature, but the results did not improve sufficiently; the standard deviation of the signals increased to 23,1 and 26,4 %, making the method less valuable. The influencing processes that are considered in this research, which might have an influence on (disturbing) the brightness temperature and thereby the CMC-ratio, are: surface roughness, local precipitation, vegetation, distance from the wet cell to the measurement cell, salinity, downscaling effects, re-gridding effects and the location of the wet calibration cell itself.

- **Surface Roughness**
  For the 37 GHz channel, objects larger than 6 mm should be considered rough, following the Fraunhoffer equation. In practice, this means that the entire land surface and likely even water surface within the tiles should be considered rough. Possibly, this means that even small capillary waves on lake Nokoué constantly influence this signal.

- **Local Precipitation**
  Local precipitation does not have a correlation with either of the T_B signals (Figure 5.11).

- **Vegetation**
  The Ka-band (i.e. $\lambda \approx 8mm$) has a very small penetration depth and therefore vegetation and canopies have a large influence on the incoming T_B. In other words, an area covered in water in the measurement cell will not generate the same T_B as the same area in the wet calibration cell, due to noise caused by vegetation, presumably resulting in a higher T_B for the measurement cell. Eutrophication (i.e. "*the process by which a body of water becomes enriched in dissolved nutrients (such as phosphates) that stimulate the growth of aquatic plant life usually resulting in the depletion of dissolved oxygen*") in Lake Nokoué (caused by salt

water intrusion) causes strong rapid growth of the water hyacinth on lake Nokoué, which can equally influence the wet cell signal (Djihouessi and Aina, 2018).

- **Distance from Wet cell**
  A linear relation was found between T_{B_D} at location x and T_{B_W} ($\Delta T_B = T_{B_D} \breve{} T_{B_W}$). Although the distance from the wet cell itself is supposedly not influential, changing soil composition (e.g. higher clay content in the southern delta) and soil moisture conditions might be accountable.

- **Salinity**
  Salinity is not expected to have an influence on the T_{B_W} as this only applies to signal below 6 GHz (Woodhouse, 2006). In practice, however, the wet calibration cell taken in lake Nokoué might be influenced by brightness temperatures from the sea as the signals are very similar (figure 5.9).

- **Downscaling Effects**
  Downscaling effects of the 10 km footprint to a 3.125 km tile can cause noise from surrounding land surfaces. Furthermore different image gridding algorithms have been used for the 3.125 km and 25 km tiles: GRD and SIR, respectively (Brodzik and Long, 2015) (Figure Appendix B.4 - B.5).

- **Re-gridding Effects**
  Not only does downscaling play a role in the 3.125 km product (using the SIR algorithm), the 25 km cells (using the GRD algorithm) also show noise from surrounding cells as we can see from brightness temperature measurement of the wet calibration cell in lake Volta (Figure 5.9). Therefore, in some cases it might be preferable to use the original footprint data (i.e. level 0-1) instead to better control the actual signals that are included.

- **Wet Calibration Cell location**
  The stable results of the 3.125 km cell in lake Volta suggest that the re-gridding effects (i.e. both downscaling and re-gridding) have had an effect on the wet calibration signal in lake Nokoué. In other words, the lake is too small and in the Ouémé catchment no suited permanent fresh water body is present (figure 5.9).

6.2 DEM vs. HAND

The outcome of comparisons between mapping on the MERIT DEM and mapping on the HAND (derived from the DEM) is unequivocal. The following characteristics influence the performance of this mapping step.

- **Natural slope**
  The quality of mapping on a DEM depends on the natural slope in that cell. In cells with little elevation like cell 8 and 10, this causes no large problems, but otherwise, such as in cell 3, it can cause an overestimation of inundation extent downstream (i.e. false positive error) and an underestimation upstream (i.e. false negative). This result is clearly visible on the borders between cells, where the inundation estimation of the upstream cell does

not correspond with the downstream cell (e.g. border between cell 1 and 3 or 4 and 6). Using a HAND avoids this problem.

- **Non-inundated tributaries**
  Both the HAND and DEM suffer from the effect of non-inundated tributaries, but this process has a larger effect on the HAND. This is clearly visible in figure 5.20d in nearly all cells (but especially cells 1, 2, 3, 4 and 6) and causes a self-sustaining error: the over-representation (i.e. false positive error) of non-inundated tributaries causes an under-representation (i.e. false negative error) of the inundated river and tributaries. Cell 4 and 6 clearly depict this effect. Setting contiguity constraints does reduce the false positive errors, but not the false negative errors (figure 6.2), because the tributaries still influence the corresponding elevation level found in the cumulative distribution of the measurement cells. The false negative errors could be improved by manually adjusting (i.e. masking) the maximum allowable inundation extent. In the end, this research refrains from doing so because this results not only in a very local solution, it furthermore highly depends on the quality of the validation method. One would enter a "slippery slope", since the question until which point the mask may or should be applied to mimic the validation material in order to improve results is subjective.

- **Validation method**
  Validating with MODIS optical validation comes at a spatial resolution of 250 m, which makes the method unable to capture inundated smaller tributaries. In other words, it could be that the HAND mapping method allocates water to tributaries that were not found inundated by the validation method, but in reality were inundated. Using higher resolution validation imagery (e.g. Sentinel (10 m), Landsat (30 m) or a different validation method (e.g. ODK-collect inundation survey ($\approx$ 5 m)) can (partially) mitigate this problem.
  Although validation with the ODK-collect inundation survey is not possible, a first test for the 2018 methods shows promising results in terms of measurement accuracy ($<$ 5 m accuracy). Interestingly, the measurements are taken at the edge of the inundation extent and show a lower standard deviation than measurements taken for the MERIT DEM (figure 5.19). Although the DEM naturally has a larger variation in elevation than the HAND, these samples do show that perhaps mapping on a HAND is preferable in some cases, because it captures inundated zones which are now invisible to the MODIS validation imagery.

- **Local depressions**
  Local depressions can cause a problem especially when mapping on a DEM, which seems to be a minor problem in the Ouémé delta. Setting contiguity constraints (i.e. coordinates mapping technique) can improve this result.

- **Inundation Size**
  This is a problem for the HAND only, since a normal DEM already naturally has higher values of elevation. Small inundations do sometimes not manage to exceed the inundation detection threshold (i.e. $h_{HAND} < 0,0$), which for the HAND lies between 2 - 5 % of inundation in the measurement cell, corresponding to 12,7 and 31,8 km^2 inundated area respectively. A higher threshold usually corresponds to a cell with less elevation and more rivers or tributaries, so the 5 % is found in cell 10, for instance. Despite the higher threshold,

cell 10 always reports inundation because of the size of inundation present in that cell. For smaller inundations in cell 5 (threshold at 4 %) this was not the case, resulting solely in false negative errors, since no inundation could be mapped.

- **Stitching**
  In terms of transition between cells the HAND method performs better than the DEM, in part because of the aforementioned natural slope effects.

The size of these false positive and false negative errors can be compared relative to the mapped inundation extent, but this favours the more inundated cells, such as cell 10. Therefore the mapping errors are schematised in figure 6.2 and presents the error as surface area compared to the cell size (as surface area in figure 6.2a and as percentage of the cell in figure 6.2b), compared to the MODIS validated inundation extent (figure 6.2c) and compared to the mapped IEMM inundation extents (figure 6.1). Detailed figures of individual cells can be found in Appendix E.

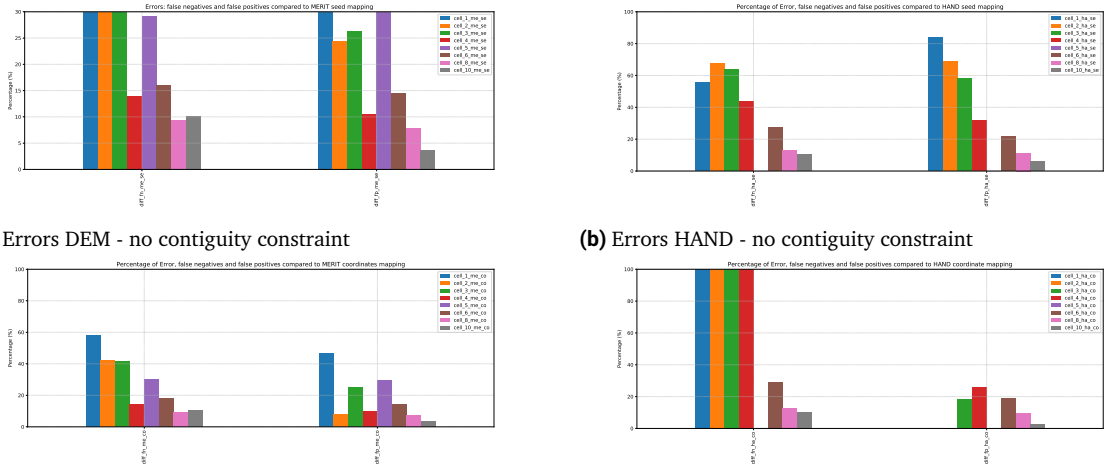

(a) Errors DEM - no contiguity constraint

(b) Errors HAND - no contiguity constraint

(c) Errors DEM - contiguity constraint

(d) Errors HAND - contiguity constraint

Figure 6.1. Mapping errors (1/2). Reading guide: Figure (a) and (b) depict errors without contiguity constraints and (c) and (d) including contiguity constraints, all for HAND and DEM maps respectively (own work)

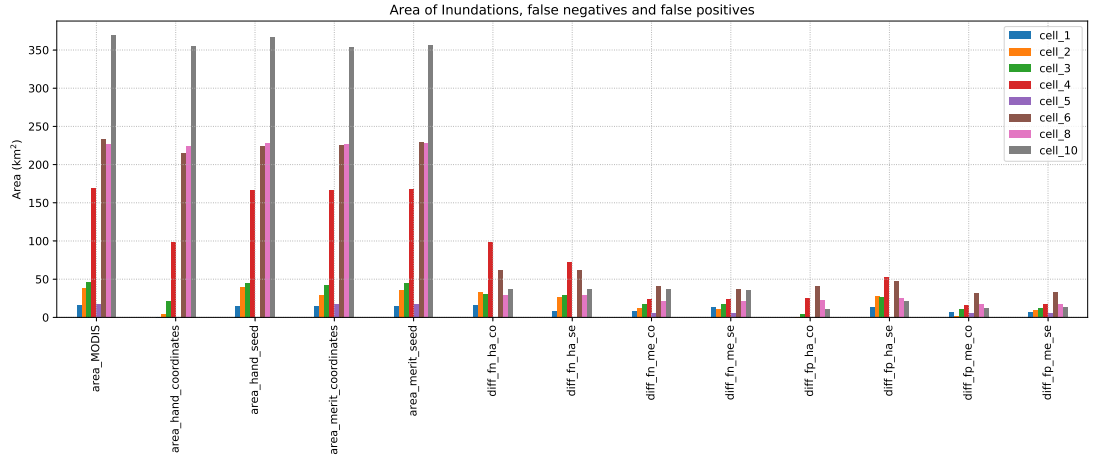

(a) Mapping methods and errors relative to EASE grid cell (km^2)

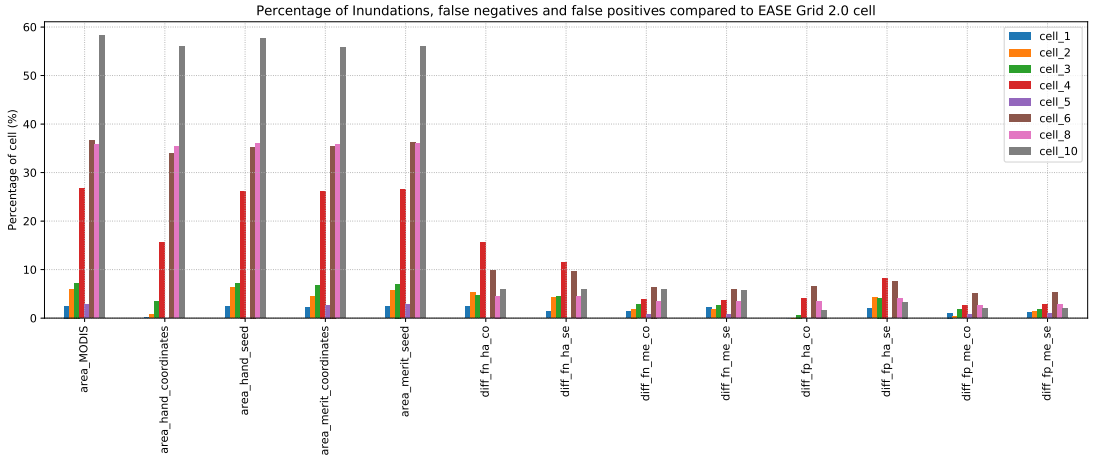

(b) Mapping methods and errors relative to EASE grid cell (%)

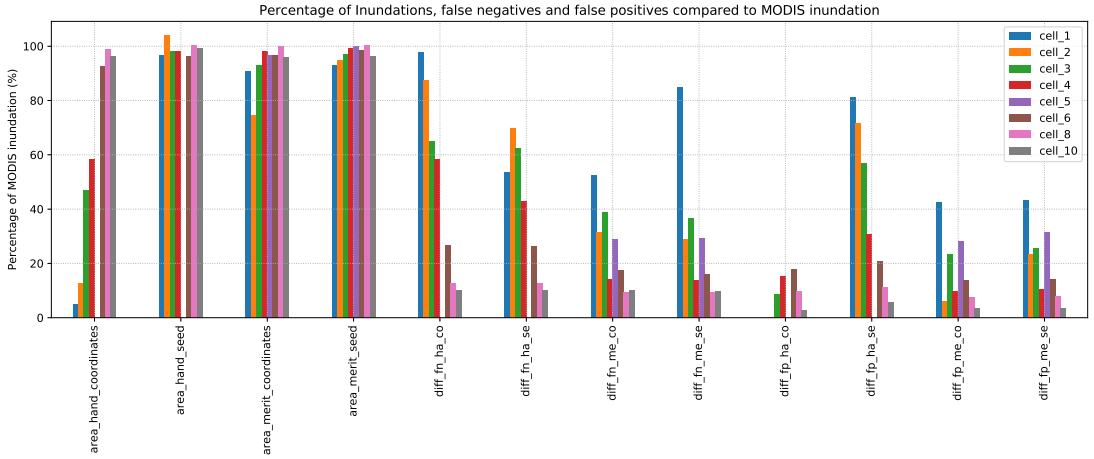

(c) Mapping methods and errors relative to MODIS inundation extent

Figure 6.2. Mapping errors (2/2). Reading guide: hand (or 'ha') = HAND elevation map; merit (or 'me') = DEM elevation map; coordinates (or 'co') = Mapping method based on contiguity constraints; seed (or 'se')= Mapping method without contiguity constraints; diff = errors; fn = False Negative mapping error; fp = False Positive mapping error. Figure (a) depicts the area and (b) the percentage of mapping errors relative to cell size. Figure (c) depicts the error relative to MODIS inundation extent mapping (own work).

6.3 Inundation and Discharge

The comparisons between inundation in cell 6 and the discharge data from the Bonou station suggest that different stages of inundation are visible. More local information about these stages, such as 'regular' flow, bank-full flow and overtopping is required to draw conclusions from these observations.
Although in this case the discharge station was located in a region with wide floodplains, usually the ideal location for discharge and inundation measurements differs (figure 6.3).

Discharge-inundation scatter-plots do not only provide information on the main river, but can also show information about inundation of tributaries. Comparing the entire AMSR-E period shows that in cell 6 different 'branches' of inundation exist, which are the effect of different tributaries inundating. This is confirmed by inspection of one of the validation points located on this branch in the 2007 inundation season (30-09-2007) (figure 6.4a). In 2008 (figure 6.4c) a clear effect of surpassing the Q > 800 m^3/s threshold is clear. Furthermore in individual years hysteresis can be observed, due to the time lag between rise and fall of discharge and rise and fall of inundation (the latter following the former) (figure 6.4c-6.4c).

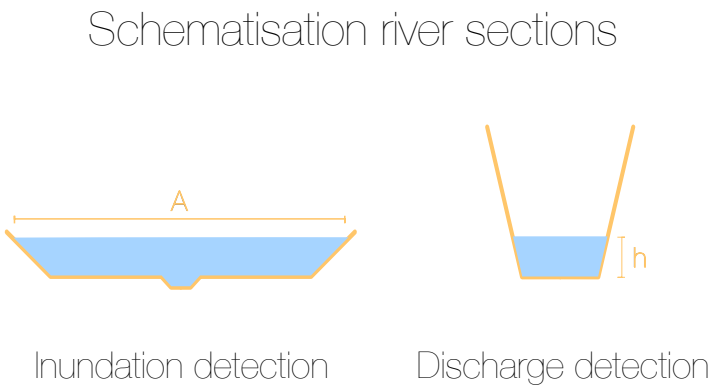

Figure 6.3. Schematisation of an ideal scenario for inundation and discharge detection, left and right respectively (own work).

6.4 Uncertainties

A comprehensive uncertainty analysis is not carried out in this research, due to the large number of steps involved in the mapping method, in which the inaccuracies are not always known or well described. The following list gives a description of the sources of uncertainties and discusses which ones should be further investigated to conduct a thorough uncertainty analysis.

- **Sensor**
  The ASMR-E sensor has a reported sensor sensitivity of 1 K (*AMSR-E Instrument Description*). Considering that for instance for cell 6, the measurement and dry calibration annual mean are about 276 and 277 K, it becomes clear why one cannot distinguish any surface

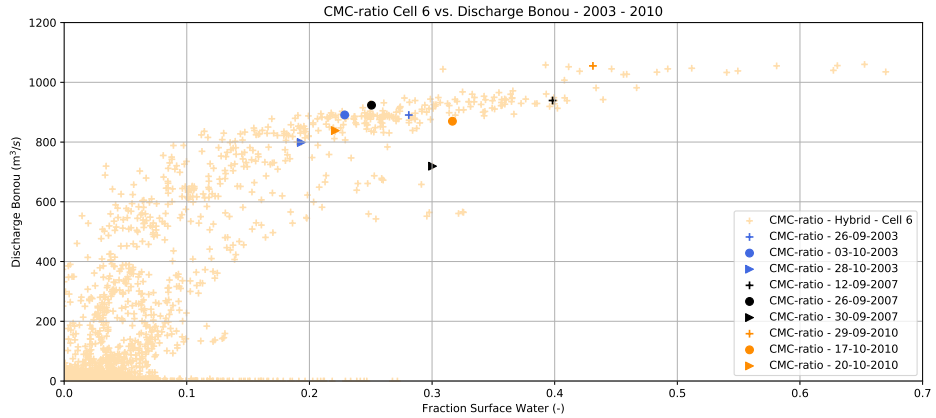

(a) CMC-ratio vs. Discharge - 2003 - 2010

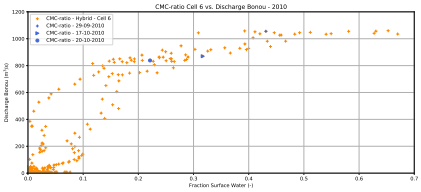

(b) CMC-ratio vs. Discharge - 2010

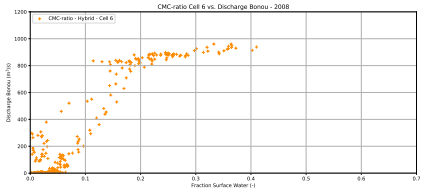

(c) CMC-ratio vs. Discharge - 2008

Figure 6.4. CMC-ratio with Discharge comparison. (a) for the entire AMSR-E period (2003-2010), (b) for 2010 and (c) for 2008 (own work)

water in the measurement cell under 'normal' (i.e. non-inundated) conditions. During the inundation season these signals start to move away from each other and from the 1 K sensor (in)accuracy when suddenly inundations become visible. Based on the optical validation, a relation between accuracy and standard deviation over surface water fraction is found. Although more validation is needed with surface water percentages between 10 and 25 %, figure 6.5. For an accuracy over 80 %, approximately 25 % surface water in the measurement cell is required, corresponding to 158.75 km^2.

- **Level 0 - 3**
  The incoming level 0 brightness temperature undergoes several corrections before it arrives at the level 3 MEaSUREs product. The details about this step are given in the technical documentation (Brodzik et al., 2016).

- **Downscaling and Re-gridding**
  The downscaling and re-gridding done to produce the MEaSUREs dataset has an influence on the signal, especially due to overlapping tile effects and the different algorithms used (GRD vs. SIR) (Paget et al., 2001).

- **Signal filtering**
  The incoming brightness temperature is corrected by the Savitzky-Golay filter with a 15 day

window and a 3^{rd} order polynomial. More validation data is required to investigate which window and order are preferable.

- **Calibration cells**
  The assumption of 0 and 100 % surface water in the dry and wet calibration cells respectively should be studied more extensively with local precipitation and in-situ terrain inspection.

- **Validation material**
  The validation material used most in this research is the MODIS 250 m NIR band, which directly indicates the approximate accuracy of the validation steps. The inundation extent survey has an accuracy of about 5 m.

- **Digital Elevation Maps**
  The MERIT DEM has a horizontal spatial resolution of about 90 m and a vertical resolution of 10 cm, assuming that the region is covered by ICESat observations (NASA and Zwally, 2016; Yamazaki et al., 2017). Mapping the given surface water fraction on a certain digital elevation map by means of the elevation percentiles causes rounding errors. For example, if a 0.246 surface water fraction is found, now either the 24^{th} or 25^{th} percentile are taken. Applying linearisation can solve this problem.

- **Data fusion**
  Correcting brightness temperatures and subsequent CMC-ratios from other satellite missions causes noise in the signal, which should be further investigated in research dedicated to data fusion. Reference approaches from soil moisture studies can be used as a starting point (Schalie et al., 2018).

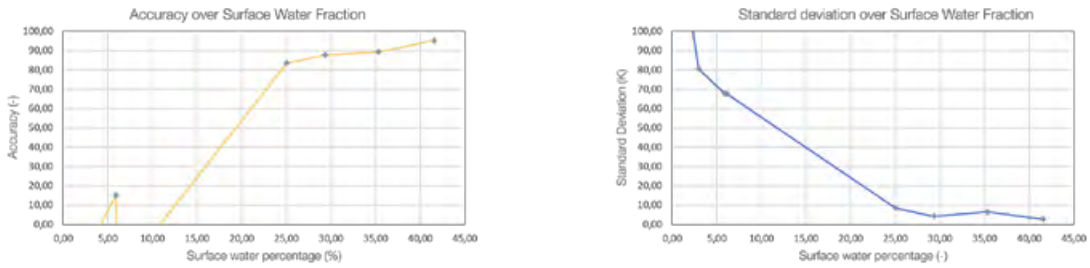

(a) Accuracy of IEMM scale estimation

(b) Standard deviation of IEMM scale estimation

Figure 6.5. Relation between accuracy (a) and standard deviation (b) over surface water percentage based on nine validation days (own work)

6.5 Limitations

The following limitations were observed and should be taken into account when interpreting the results or when additional research is desired.

6.5.1 Lack of Wet Calibration cells

The notion of the CMC-ratio is that permanent fresh water bodies enable scaling of measurement cells, but in reality the outcome might be more uncertain than expected. In reality only few catchments will have permanent surface water bodies large enough to facilitate such a measurement cell (order scale 30 x 30 km). Although this research focussed on water bodies that are permanently large enough to serve as wet calibration cell (and thereby only leaving very few options), the research could also be set-up with a region that is not fully covered in water, but is very constant in surface water fraction. This would allow again more regions to deploy such a system, just like the Hybrid method avoids the mere necessity of the presence of wet calibration cells.

6.5.2 MEaSUREs dataset

Availability of the MEaSUREs till April 2017 makes this dataset only suited for past inundations, but not for in-season applications. Furthermore, applicability of this dataset does in part depend on the location of the grid cells in relation the the study area. In this research, cell 2, 4, 6, 8 and 10 were properly aligned to capture important parts of the main river and investigate upstream-downstream behaviour, but this will not be the case for every study. Especially the large grid cells make analyses close to the sea difficult, whereas those regions are often of interest due to human presence and the delta-like landscape.

Furthermore, the available 3.125 km and 25 km products depend on different image re-gridding algorithms and it is not yet fully understood how this affects combinations or direct comparisons of signals from these different products.

Despite the level 3 data (among others correcting for errors) inter-system differences, such as bandwidth, incidence angle and sensor sensitivity cause the brightness temperatures obtained from the same locations to change between sensors in terms of mean and standard deviation. This makes it difficult to conduct inter-system comparisons because data fusion would need to be applied. Even then, it remains time series analysis should be done with care because data fusion can also cause information-loss due to over-manipulation of the data.

6.5.3 Detection of smaller inundations

The effect of cell size also has an effect on smaller inundations, such as cell 1, 2, 3 and 5. With the 25 km cell product, these inundations are difficult to grasp. Smaller inundations could therefore be better investigated with the 3.125 km cells (measurement and dry calibration).

6.5.4 Validation material

In the current set-up, optical imagery both functions as a validation method (of inundation scale and inundation extent) and as the input to determine the artificial wet calibration brightness temperature used in the hybrid method. Although the reported accuracy of the IEMM methods still gives an indication of the performance of these methods, the results should be reviewed with

care, because the measurements indirectly rely on themselves. Alternative validation methods like the inundation extent survey can add a new independent source of information, which could reduce a bias. The accuracy of validation with the inundation extent survey could be based on a length-scale, which can contribute to represent the outcome as an interpretable quantity that contributes to the objective to provide information on inundation extent to locals.

With the current optical validation, cloud-correction is required and this is done manually in this research. However, this also leads to arbitrary decisions where cloud shadows are difficult to distinguish from surface water. Based on elevation data an estimate can be made about what is expected to be "dry" land and what is expected to be inundated land, but in-situ data and observations would improve this validation step. Some supposed cloud-shadows could even be due to precipitation causing isolated puddles that would have an effect on the brightness temperature signal.

Higher accuracy (optical) validation material like Sentinel 1 and 2 could provide more information on the location of surface water.

6.5.5 Assumption of horizontal water table

Inundation mapping is done by allocating surface water to a certain level of elevation, either in the form of a DEM or a HAND. This assumption more likely holds for slowly developing inundations, but for rapidly developing floods this might not be the case. More research is required to investigate these differences and wether this assumption is sound.

6.5.6 Critical precipitation

Although extreme daily precipitation seems to have decreased over the past decades, it has not been investigated if daily precipitation is the critical time-frame for inundations. Perhaps, analyses on hourly, weekly or monthly rainfall maxima would give different results. More information on hydrological models should be incorporated to investigate the exact behaviour between rainfall and runoff.

6.5.7 Scale of disaster reports

The disaster database does not provide detailed spatial information on where and how many people are affected. Only towns and regions are listed, which makes it difficult to make a comparison with population density maps (available at gridded 1 km resolution). This still leaves many questions open about the scale and location of the impact of disasters. The database also works with a ‘threshold’ system, leaving out smaller inundations, although these still might have a local effect.

Stating that Sô-Ava and Aguégués are heavily affected by inundations is the best estimate that this research can provide, but it should be interpreted carefully. Comparing disasters with and without Sô-Ava and Aguégués showed that there is a large difference in impact, especially in terms of deaths. However, when an inundation does not reach Sô-ava and Aguégués it might also mean that the inundation is just smaller overall. Furthermore it is not possible to distinguish between

the location of the people affected and deaths. This means that we cannot fully attribute the difference of disasters with and without to Sô-ava and Aguégués. More information is supposedly available, but due to administrative reasons not available for this research. Organisations ANCP (supported by some NGO's like Red Cross) are in charge of the emergency response during and after inundations.

6.5.8 Dam construction

A development not included in this research, but still ongoing is for instance the construction of a dam upstream in the catchment. This would have a large influence on inundations. Probably positive in terms of effects of extreme inundations, but potentially negative for farmers in the catchment relying on natural inundations for irrigation.

6.6 Future Scenarios

The research has provided more information on the development of inundations, disasters, precipitation and population over the past decades. Based on these results, a qualitative interpretation and projection can be made on how these processes will develop in the future. The development of inundations both depends on internal and external factors, which will be referred to as 'driving forces' for change. With these driving forces, four scenarios and the expected effects are presented. The exact development of these scenarios cannot be quantified, but this method is merely intended to present the general direction in which the developments of inundations are expected to progress.

- **Internal forces: Governance**
  The most important internal force is governance, which should be interpreted in various aspects.

  Based on the knowledge that population present in the inundation prone areas likely caused the steep increase in negative impact of inundations and considering the past and expected population growth, the first issue that should be dealt with is the urbanisation in the Ouémé delta. The population residing in these inundation prone areas likely does so out of financial need, since housing in the safer (i.e. higher) zones of the delta is more expensive. The government can play a role in motivating people to settle in other locations or by increasing the resilience of people, infrastructure and buildings located in these areas.

  On the other hand governance also plays a role in the way data and knowledge are accessible to researchers, governmental organisations and other institutions. As of now, this is still very protective, but in view of the national interest it is important that this cross-sharing among universities, ministries and institutions takes place as it accelerates the process of gaining knowledge on inundations as well as finding subsequent possible solutions.

  In the ideal situation where an integral flood risk study is carried out and an effective mitigation strategy is in place, including a fully operational flood early warning system, the impact of inundations could presumably be reduced. If however the government

refrains from taking action, the impact of inundations will deteriorate as the continuation of population growth will continue to have an increasingly negative effect on the population health and country's economy.

- **External forces: Climate Change**
  Climate change is seen as the most important external driving force, but perhaps counter-intuitively, a larger effect of climate change in the Ouémé catchment is expected to be accompanied with a decreasing effect on the extreme inundations in the Ouémé delta as a result of the further decreasing (extreme) rainfall by the African Monsoon. As a consequence, the subsequent runoff from the Ouémé river will also decrease (Biao, 2017).

  Although the decrease in rainfall might be accompanied with an increase in other problems, such as increase in drought and higher rapid surface runoff, these effects have not been studied in detail yet and should therefore be better understood. However, the Ouémé catchment is a generally speaking wet catchment.

  A smaller effect of climate change means that the extreme inundation events will remain similar to the current situation. Nevertheless, the notion that maximum inundations might not increase should however not be interpreted too positively: already as a result of the current maximum inundation patterns, vast negative impacts are a result, based on past disaster reports. Further studies on interpreting the climate change scenarios as presented by IPCC can result in more detailed information on the effects of climate change (Riede et al., 2016).

The resulting scenarios are presented in figure 6.6. For instance, in scenario 1 climate change will have a large impact and therefore less extreme inundations will take place. However, the governance in Benin is still weak, and as such the increasing population remains exposed to inundations. Beninese government officials, politicians and other stakeholders should do their best to direct to scenario 2 or 4. In either case, the population would be better protected to inundations than they are nowadays. Students, researchers and scientists should investigate the effect that climate change has (i.e. scenarios 1, 2 vs. 3, 4) to support effective decision making.

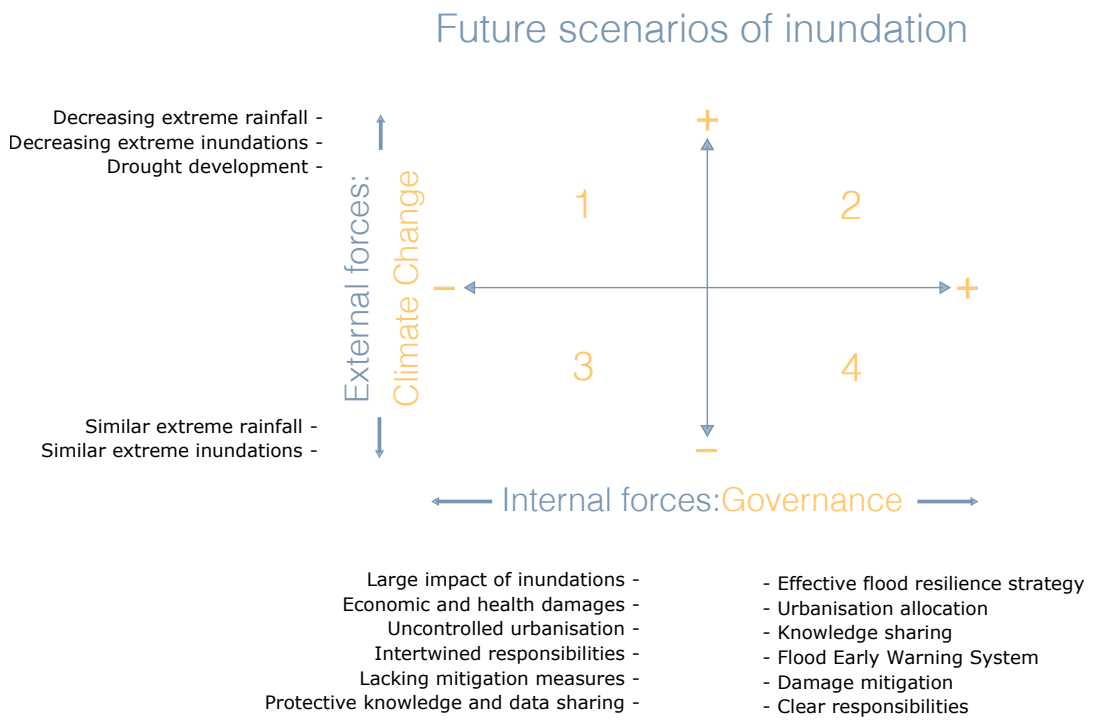

Figure 6.6. Schematisation of four future scenarios regarding inundations as a result of climate change (external) and governance (internal) (own work).

7 Conclusions and Recommendations

This chapter presents the answers to the research questions as presented in chapter 1 (Section 7.1). Furthermore recommendations for further research are given in Section 7.2.

7.1 Conclusions

Sub-question 1 - *How can fluvial inundations be detected by means of optical and passive microwave imagery in the Ouémé delta, Benin?*

Detection of fluvial inundations in the Ouémé delta is technically feasible with both optical and passive microwave remote sensing imagery. MODIS optical imagery works best by selecting the NIR surface reflectance band, but suffers from the high cloud cover in the Ouémé delta, resulting in approximately three (partially) cloud-free images per inundation season. Despite the high cloud cover, due to the higher spatial resolution (250 m; high compared to passive microwave spatial resolution) the few cloud-free days provide useful validation material. Passive microwave radiometry gives optimal inundation detection results when using brightness temperatures from the Ka-band (36.5 - 37.0 GHz) with horizontal polarisation on the descending node (i.e. night-time overpass), preferably with the 25 km cell product from the NSIDC MEaSUREs dataset, which is based on the EASE Grid 2.0.

Sub-question 2. *How can the inundation extent be derived from the inundation detection method?*

The scale of inundation can be investigated by transforming the CM-ratio to the CMC-ratio and obtaining the estimated surface water fraction in a given region of interest referred to as measurement cell. This method scales brightness temperature between the measurement cell and the wet and dry calibration cells, which are assumed to be covered by 100 and 0 % water, respectively. The wet calibration cell above lake Nokoué is taken as a 3.125 km cell due to the limited size of the lake while the dry calibration and measurement cells are taken as 25 km cells. The wet calibration generates a noisy signal, possibly caused by the downscaling and re-gridding effects, the limited size of lake Nokoué and vegetation in the form of water hyacinths. MODIS cloud-free validation images indicate that the proposed CMC-ratio method (i.e. Baseline) underestimates the true scale of inundation, likely related to the aforementioned errors in the wet calibration cell, but possible also in the measurement cell due to vegetation and canopies covering actually inundated surfaces. The underlying physical reason for this offset cannot yet be fully described, but using the Hybrid CMC-ratio method provides satisfactory results ($>$ 80 % accuracy) for inundation scale estimation in cell 4, 6, 8 and 10 and relies on including a constant, artificial wet calibration cell based on reverse engineering the inundation extent from optical cloud-free validation images.

The subsequent inundation extent can be estimated by mapping the given surface water fraction to the corresponding percentile of lowest pixels in an elevation map, for which MERIT DEM and the derived MERIT HAND are considered, both with and without contiguity constraints. Using the MERIT DEM without contiguity constraint gives the best results based on the false positive and false negative errors compared to MODIS optical imagery, but in-situ inundation extent measurements from 2018 indicate more stable corresponding HAND values. The IEMM enables inundation extent analysis at a given location and for a given period of time.

Sub-question 3 - *How can information about timing of fluvial inundations be derived from the inundation detection method?*

Timing of inundations can be derived by analysing the different stages of inundation, which can be distinguished by analysing the CMC-ratio over time, demonstrating sharp changes in surface water fraction. These changes supposedly correspond to inundation 'regimes', which in terms of river discharge would be 'normal' discharge (water within the banks), inundating floodplains (bank full discharge) and extreme inundation (i.e. bank overtopping). Especially in the last stage the CMC-ratio gives a sharp response, which is the regime most relevant for disaster and extreme inundation analysis. In Bonou (measurement cell 6) the extreme discharge is 800 m^3/s and the corresponding surface water percentage is 12.7 %. Comparison of CMC-ratio, discharge in Bonou and the emergency thresholds defined by SAP demonstrates that the CMC-ratio becomes increasingly sensitive to larger inundations. Thereby, the CMC-ratio enables analysis of start, duration of a given inundation stage and maximum inundation, especially suited for extreme inundations. Furthermore, the propagation speed of inundations can be derived from the difference in timing of maximum inundation between the cells, which is useful information for flood early warning systems for instance. In the Ouémé catchment, the maximum inundation in the urbanized southern delta arrives 4.0 days after the peak inundation peak at Bonou (measurement cell 6).

Sub-question 4 - *Can trends in extreme inundation patterns be observed by multi-annual, multi-system time series analysis?*

Multi-annual analysis between 2003-2010 (AMSR-E) shows that the size of maximum inundation extent is more important than the days that inundations exceed the emergency threshold. Multi-system analysis is hampered by slight differences in satellite and sensor characteristics. So, instead of nearly 40 years of data (1978 - 2016), 20 years remain (1996 - 2016). In 2003, 2007 and 2010 overlapping coverage by DMSP F-13, F-15 and AMSR-E enables data fusion in the form of correction of brightness temperatures and the subsequent Hybrid CMC-ratio. Based on the resulting fused dataset a time series analysis is carried out, focussing on the extreme inundations. Based on the available dataset no clear trend in inundation is found, which is confirmed by reference studies (Hounkpè et al., 2015b). The time series does allow for an estimation of maximum daily inundation extent with a 1, 10 and 100 year return period, indicating that the 2010 inundation season approximately corresponds to a maximum 100 year return period inundation extent. More research on data fusion is required however, since 1998 and 1999 maxima exceeded the 2010 discharge, but does not exceed the 2010 maximum inundation extent.

Sub-question 5 - *How do precipitation and population growth relate to the impact of fluvial inundations in the Ouémé delta?*

Extreme daily rainfall between 1970 and 2014, in the middle and northern Ouémé catchment has decreased, confirming trends found in related climate change studies and contradicting the supposed increase of inundations extents. Population growth since 1970 occurred especially in the southern delta in the urban agglomeration adjacent to lake Nokoué. This suggests that presence of population has a larger effect on the impact of inundations than the actual inundations, which occur naturally. In the study region, especially the towns Sô-Ava and Aguégués are susceptible to inundations and cause a large impact in terms of affected people and deaths. Based on these processes and the lack of a clear trend in inundation maxima, governance can play an important role in the prevention and mitigation of future inundation disasters.

Research question. *How can fluvial inundations be detected by means of optical and passive microwave imagery in the Ouémé delta, Benin?*

The conclusion of this research is therefore that with the presented method passive microwave and optical remote sensing imagery form a valuable source of information regarding timing and extent of inundations. Data-scarce regions thereby suddenly become much less "scarce", since the open source data and software used in this research can in theory be applied anywhere in the world. The IEMM, consisting of the consecutive steps of inundation detection and scale estimation by the Hybrid CMC-ratio, followed by inundation extent mapping estimates with MERIT DEM or HAND elevation maps, can provide daily inundation extent estimates at a given location, even under cloudy conditions and without the presence of a wet calibration cell. The inundation size should however be of sufficient size since the method does not work for smaller inundations. The timing of inundations can also be derived from the CMC-ratio, where the resulting signal becomes increasingly sensitive to extreme inundations and stages of inundations can be distinguished. The lead time of inundations can be used in flood early warning systems. Multi-annual and multi-system analysis enable trend analysis in inundations, although multi-system analysis requires additional corrections for the inter-system variations. Additional databases, such as precipitation, population growth and reported disasters enable a first step in investigating the relation between these processes in the Ouémé catchment. The presented method works both stand-alone as well as complementary to conventional flood risk studies.

7.2 Recommendations

The following is recommended for further research on this topic.

Current model improvements

- The role of vegetation (inside both measurement and wet calibration cell), soil composition and soil moisture should be further investigated to improve understanding of influencing processes, which can further improve the Full method CMC-ratio.
- Setting up the system with 3.125 km cells from the MEaSUREs database could allow for smaller inundations to be detected, although downscaling and re-gridding effects are likely to continue to cause noise.
- If more discharge data is granted, more information can be obtained from (i) the stages of inundations and (ii) the propagation of inundations throughout the catchment. Discharge stations in Benin are operated by the Water Directory (DG-Eau).
- Instead of focussing on regions with very large water bodies, it might be worth considering selecting the wet calibration cell over a region with a very constant surface water fraction. This would allow more regions to deploy the CMC-ratio. Alternatively, just like this thesis, the hybrid inundation scale estimation can be deployed.
- Considering the influence that presence of population has on the (sometimes disastrous) effect of inundations and considering expected population growth in Benin (and similar countries across (West-Africa), further research should aim to predict the development and impact of inundations.
- Improved data fusion techniques allow more accurate multi-system time series analysis as well as longer time frames of the MEaSUREs dataset included in the analysis.
- Using the CMC-ratio with the original imagery footprint avoids the re-gridding effects of the EASE-Grid 2.0.
- Investigating a comprehensive uncertainty and sensitivity analysis.

Alternative means of Validation

- Using the ODK-collect inundation extent survey can provide more accurate information on the spatial extent, which can be used for validation of mapping estimates from the IEMM. This reduces the dependency of optical remote sensing imagery as the only source of validation. A user manual (written in French) for this system is available and can be provided by the author. Cooperation with Beninese researchers showed promising results and this collaboration could be continued.

- When this model is developed in a a more data-rich environment in terms of discharge, high-resolution elevation models, conventional flood risk studies and hydrological models, improved comparisons can be made between conventional methods and the IEMM method. The lessons learned can subsequently be deployed in other data-scarce environments. An example of this is the use of the Savitzky-Golay filter that is used for signal smoothing and to account for missing days. Due to the limited validation material determining these settings, is still to some extent an arbitrary procedure. Once data-rich environments provide more information on the required settings this could subsequently be applied in data-scarce environments.

Expanding the possibilities

- If the relation between precipitation and (extreme) inundation is better understood, the model could be tailored towards predicting inundations, which in the case of Benin can be used stand-alone or complimentary to the current flood early warning system. The current flood early warning relies on discharge data, which suffers from data-gapss. In the case of Benin operating the flood early warning system (i.e. SAP) still is a laborious procedure.

- Developing the model for AMSR-2 data can provide more information on (i) how different grids affect the inundation detection and (ii) what the possibilities are for in-season applications of the IEMM. Level 2 data from JAXA's G-Portal is available after approximately 3 days of overpass (JAXA, 2018).

- Developing a mapping method where inundation can be allocated by selecting which parts of the main river or tributaries are inundated is expected to further improve the mapping accuracy.

Bibliography

Aggarwal, Shiv P., Praveen K. Thakur, and Vinay Kumar Dadhwal (2009). „Remote sensing and GIS Applications in Flood Management“. In: January, p. 12 (cit. on p. 2).

Al-Tahir, R., I. Saeed, and R. Mahabir (2014). „Applications of remote sensing and GIS technologies in flood risk management“. In: *Flooding and Climate Change: Sectorial Impacts and Adaptation Strategies for the Caribbean Region* November 2015, pp. 137–150 (cit. on p. 2).

Biao, Eliézer (2017). „Assessing the Impacts of Climate Change on River Discharge Dynamics in Oueme River Basin (Benin, West Africa)“. In: *Hydrology* 4.4, p. 47 (cit. on p. 88).

Bourles, Bernard, Peter Brandt, Guy Caniaux, and Marcus Dengler (2007). „African Monsoon Multidisciplinary Analysis (AMMA): special measurements in the tropical Atlantic“. In: *Clivar* 12.2, pp. 7–10 (cit. on pp. 3, 33).

Brakenridge, G. Robert, Son V. Nghiem, Elaine Anderson, and Rodica Mic (2007). „Orbital microwave measurement of river discharge and ice status“. In: *Water Resources Research* 43.4, pp. 1–16 (cit. on pp. 2, 25, 34, 49).

Brodzik, M. J., D. G. Long, M. A. Hardman, A. Paget, and R. Armstrong (2016). *MEaSUREs Calibrated Enhanced-Resolution Passive Microwave Daily EASE-Grid 2.0 Brightness Temperature ESDR, Version 1*. Boulder Colorado, USA (cit. on pp. 32, 33, 83).

Brodzik, Mary J and David G Long (2015). „NASA MEaSUREs Calibrated Passive Microwave Daily EASE - - Grid 2 . 0 Br ightness Temperature ESDR (CETB) Algorithm Theoretical Basis Document.“ In: *MEaSUREs Project White Paper, NSIDC, Boulder, CO.* June 2015 (cit. on p. 78).

Cazenave, A, N Champollion, J Beneveniste, and J Chen (2016). *Remote Sensing and Water Resources*. Vol. 55 (cit. on p. 2).

Center for International Earth Science Information Network - CIESIN (2016). *Gridded Population of the World, Version 4 (GPWv4): Population Density Adjusted to Match 2015 Revision of UN WPP Country Totals*. Version 4. Palisades, NY: Columbia University (cit. on pp. 11, 32).

– (2017). „NASA Socioeconomic Data and Applications Center (SEDAC) Documentation for the Global Population Count Grid Time Series Estimates, v1 (1970- 2000)“. In: 1.845, pp. 1–8 (cit. on pp. 11, 32).

De Jeu, Richard (2003). „RETRIEVAL OF LAND SURFACE PARAMETERS USING PASSIVE MICROWAVE REMOTE SENSING“. PhD thesis. VU Amsterdam (cit. on p. 25).

De Jeu, Richard A.M., W. Wagner, T. R.H. Holmes, et al. (2008). „Global soil moisture patterns observed by space borne microwave radiometers and scatterometers“. In: *Surveys in Geophysics* 29.4-5, pp. 399–420 (cit. on pp. 21–24, 34).

DG-Eau (2014). „PROJET SAP-BENIN“. In: pp. 1–90 (cit. on p. 12).

Djihouessi, Metogbe Belfrid and Martin Pépin Aina (2018). „A review of hydrodynamics and water quality of Lake Nokoué: Current state of knowledge and prospects for further research“. In: *Regional Studies in Marine Science* 18, pp. 57–67 (cit. on p. 78).

Du, Weiwei, Gerard Joseph Fitzgerald, Michele Clark, and Xiang Yu Hou (2010). „Health impacts of floods“. In: *Prehospital and Disaster Medicine* 25.3, pp. 265–272 (cit. on pp. 3, 7).

Funk, Chris, Pete Peterson, Martin Landsfeld, et al. (2015). „The climate hazards infrared precipitation with stations - A new environmental record for monitoring extremes“. In: *Scientific Data* 2, pp. 1–21. arXiv: `arXiv:1011.1669v3` (cit. on pp. 32, 54).

Hounkpè, Jean, Bernd Diekkrüger, Djigbo Badou, and Abel Afouda (2015a). „Non-Stationary Flood Frequency Analysis in the Ouémé River Basin, Benin Republic“. In: *Hydrology* 2.4, pp. 210–229 (cit. on pp. 3, 8).

– (2015b). „Non-Stationary Flood Frequency Analysis in the Ouémé River Basin, Benin Republic“. In: *Hydrology* 2.4, pp. 210–229 (cit. on pp. 7, 43, 92).

– (2016). „Change in Heavy Rainfall Characteristics over the Ouémé River Basin, Benin Republic, West Africa“. In: *Climate* 4.1, p. 15 (cit. on p. 3).

Humboldt State University (2014). *Blackbody Radiation* (cit. on p. 19).

IFRC (2013). *DREF operation update Benin : Floods Red Cross and Red Crescent action*. Tech. rep. April 2014. International Federation of Red Cross and Red Crescent Societies, p. 10 (cit. on p. 3).

IRIN (2008). *Benin: Half million potential flood victims : WHO*. Cotonou, Benin (cit. on pp. 3, 7).

JAXA (2018). *G-Portal - Globe Portal System* (cit. on pp. 32, 95).

JAXA EORC (2013). „Data Users' Manual for the Advanced Microwave Scanning Radiometer 2 (AMSR2) onboard the Global CHange OBservation MIssion 1st - Water "SHIZUKU" (GCOM-W1)“. In: 2.March, pp. 55–60 (cit. on p. 32).

Kabenge, Martin, Joshua Elaru, Hongtao Wang, and Fengting Li (2017). „Characterizing flood hazard risk in data-scarce areas, using a remote sensing and GIS-based flood hazard index“. In: *Natural Hazards* 89.3, pp. 1369–1387 (cit. on p. 1).

Kummu, Matti, Hans de Moel, Philip J. Ward, and Olli Varis (2011). „How close do we live to water? a global analysis of population distance to freshwater bodies“. In: *PLoS ONE* 6.6 (cit. on p. 1).

Lakshmi, Venkat (2017). *Remote Sensing of Hydrological Extremes*. Ed. by Venkat Lakshmi. Stanford: Springer International Publishing Switzerland (cit. on p. 2).

Marx, Werner (2004). „Application of Remote Sensing in Flood Management with Special Reference to Monsoon Asia: A Review“. In: *Natural Hazards* 33, pp. 283–301. arXiv: `arXiv:1112.2903v1` (cit. on p. 2).

McFeeters, Stuart K. (1996). „The Use of Normalized Difference Water Index (NDWI) in the Delineation of Open Water Features“. In: *International Journal of Remote Sensing* 17.7, pp. 1425–1432 (cit. on pp. 17, 37).

Mini Physics (2018). *The electromagnetic spectrum* (cit. on p. 15).

NASA (2018). *The Thematic Mapper* (cit. on p. 17).

NASA and H.J. Zwally (2016). „ICESat“. In: (cit. on p. 84).

NOAA (2018). *NNDC Climate Data Online - Global Summary of the Day* (cit. on p. 32).

NSIDC. *AMSR-E Instrument Description* (cit. on p. 82).

Ouikotan, B.R, J. Van der Kwast, A. Mynett, and A. Afouda (2017). *Gaps and challenges of flood risk management in West African coastal cities*. Tech. rep. Cancun, Mexico: International Water Resources Association (IWRA), pp. 1–12 (cit. on pp. 3, 7).

Paget, A, M J Brodzik, J Gotberg, M A Hardman, and D G Long (2001). „Using image reconstruction methods to enhance gridded resolution for a newly-calibrated passive microwave Earth System Data Record“. In: 2, pp. 1–2 (cit. on p. 83).

Riede, J.O., R. Posada, A.H. Fink, and F. Kaspar (2016). „What's on the 5th IPCC Report for West Africa?“ In: *Adaptation to Climate Change and Variability in Rural West Africa*, pp. 1–244 (cit. on p. 88).

Schalie, Robin van der, Richard De Jeu, Nemesio Rodríguez-Fernández, et al. (2018). „The effect of three different data fusion approaches on the quality of soil moisture retrievals from multiple passive microwave sensors“. In: *Remote Sensing* 10.1 (cit. on p. 84).

Shang, H (2017). „Applications of passive microwave data to monitor inundated areas and model stream flow“. PhD thesis. Delft University of Technology, pp. 1–258 (cit. on p. 2).

Smith, David (2010). *Benin suffers worst floods since 1963*. Johannesburg, South Africa (cit. on pp. 3, 44, 60).

SNV Netherlands Development Organisation (2016). *New EKN fund to improve access to water and sanitation in Benin* (cit. on p. 12).

Technopedia (2018). *Remote Sensing* (cit. on p. 15).

The Central Intelligence Agency (2018). *Benin* (cit. on pp. 7, 8).

Ticehurst, Catherine, Peter Dyce, and J P Guerschman (2009). „Using passive microwave and optical remote sensing to monitor flood inundation in support of hydrologic modelling“. In: *18th World IMACS / MODSIM Congress* July, pp. 3747–3753 (cit. on p. 2).

United Nations Development Program (UNDP) (2013). „Note D ' Information - Lancement du projet de renforcement de l'information sur le climat et les systèmes d'alerte précoce“. In: pp. 1–6 (cit. on p. 12).

Universite catholoique de Louvain (UCL), CRED, and G. Guha-Sapir (2018). *EM-DAT: The Emergency Events Database* (cit. on pp. 10, 12, 32, 75, 136, 137, 139).

U.S. Census Bureau (2018). *International Data Base (IDB), version 18.0822, code 12.0321* (cit. on p. 32).

Van de Griend, A A and M Owe (1994). „Microwave Vegetation Optical Depth and Inverse Modeling of Soil Emissivity Using Nimbus SMMR Satellite-Observations“. In: *Meteorology and Atmospheric Physics* 54.1-4, pp. 225–239 (cit. on p. 23).

Vermote, E. and R. Wolfe (2015a). *MOD09GA MODIS/Terra Surface Reflectance Daily L2G Global 1kmand 500m SIN Grid V006* (cit. on pp. 32, 33).

– (2015b). *MOD09GQ MODIS/Terra Surface Reflectance Daily L2G Global 250m SIN Grid V006* (cit. on pp. 32, 33).

– (2015c). *MYD09GA MODIS/Aqua Surface Reflectance Daily L2G Global 1kmand 500m SIN Grid V006* (cit. on pp. 32, 33).

– (2015d). *MYD09GQ MODIS/Aqua Surface Reflectance Daily L2G Global 250m SIN Grid V006* (cit. on pp. 32, 33).

Wahlstrom, Margareta and Debarati Guha-Sapir (2015). *The Human Cost of Weather Related Disasters 1995-2015*. Tech. rep. Geneva, Switzerland: CRED, UNISDR (cit. on p. 1).

Ward, Philip J., Brenden Jongman, Peter Salamon, et al. (2015). „Usefulness and limitations of global flood risk models“. In: *Nature Climate Change* 5.8, pp. 712–715 (cit. on p. 1).

Wilson, Adam M. and Walter Jetz (2016). „Remotely Sensed High-Resolution Global Cloud Dynamics for Predicting Ecosystem and Biodiversity Distributions“. In: *PLoS Biology* 14.3, pp. 1–20 (cit. on pp. 36, 47).

Wilson, Emily Hoffhine and Steven A. Sader (2002). „Detection of forest harvest type using multiple dates of Landsat TM imagery“. In: *Remote Sensing of Environment* 80, pp. 385–396 (cit. on pp. 17, 37).

Woodhouse, Iain H. (2006). *Introduction to Microwave Remote Sensing*. Boca Raton: Taylor & Francis Group (cit. on pp. 15, 22, 23, 25, 78, 105, 106).

World Bank (2011). *Inondations au Bénin*. Tech. rep. World Bank (cit. on pp. 10, 13, 101–103).

Xu, Hanqiu (2006). „Modification of Normalized Difference Water Index (NDWI) to Enhance Open Water Features in Remotely Sensed Imagery". In: *International Journal of Remote Sensing* 27.14, pp. 3025–3033 (cit. on pp. 17, 37).

Yamazaki, Dai, Daiki Ikeshima, Ryunosuke Tawatari, et al. (2017). „A high-accuracy map of global terrain elevations". In: *Geophysical Research Letters* 44.11, pp. 5844–5853 (cit. on pp. 32, 41, 84).

Inundations in Benin

A

A.1 Inundations in 2010

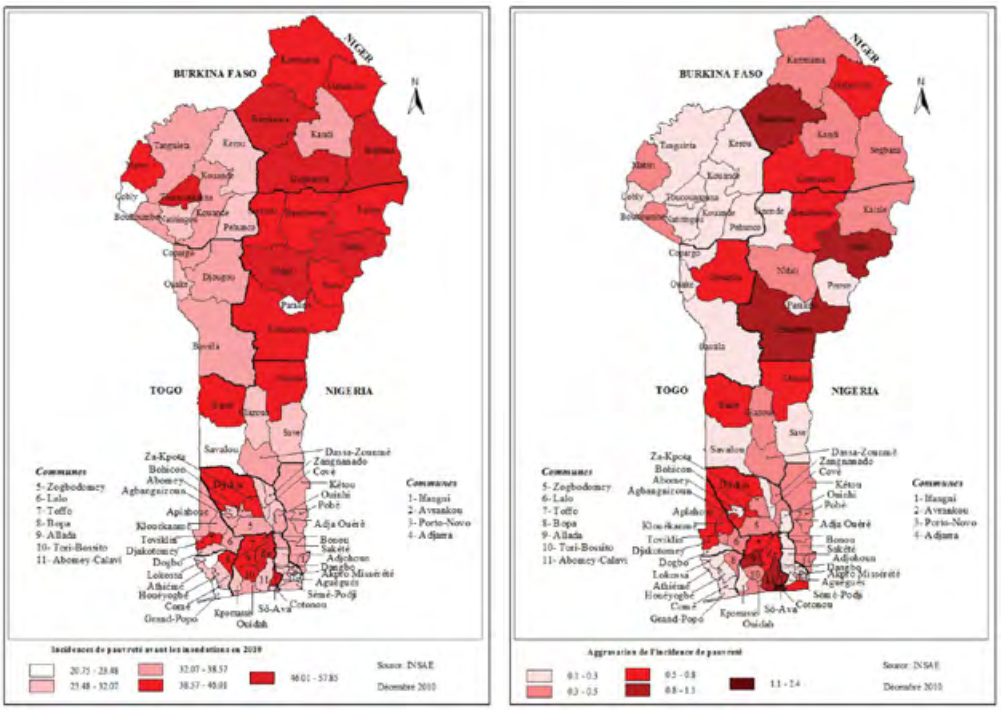

(a) Poverty before 2010 inundations **(b)** Poverty after 2010 inundation

Figure A.1. Poverty (a) before and (b) increase of poverty after the 2010 inundations (World Bank, 2011

A.2 Inundation prone areas

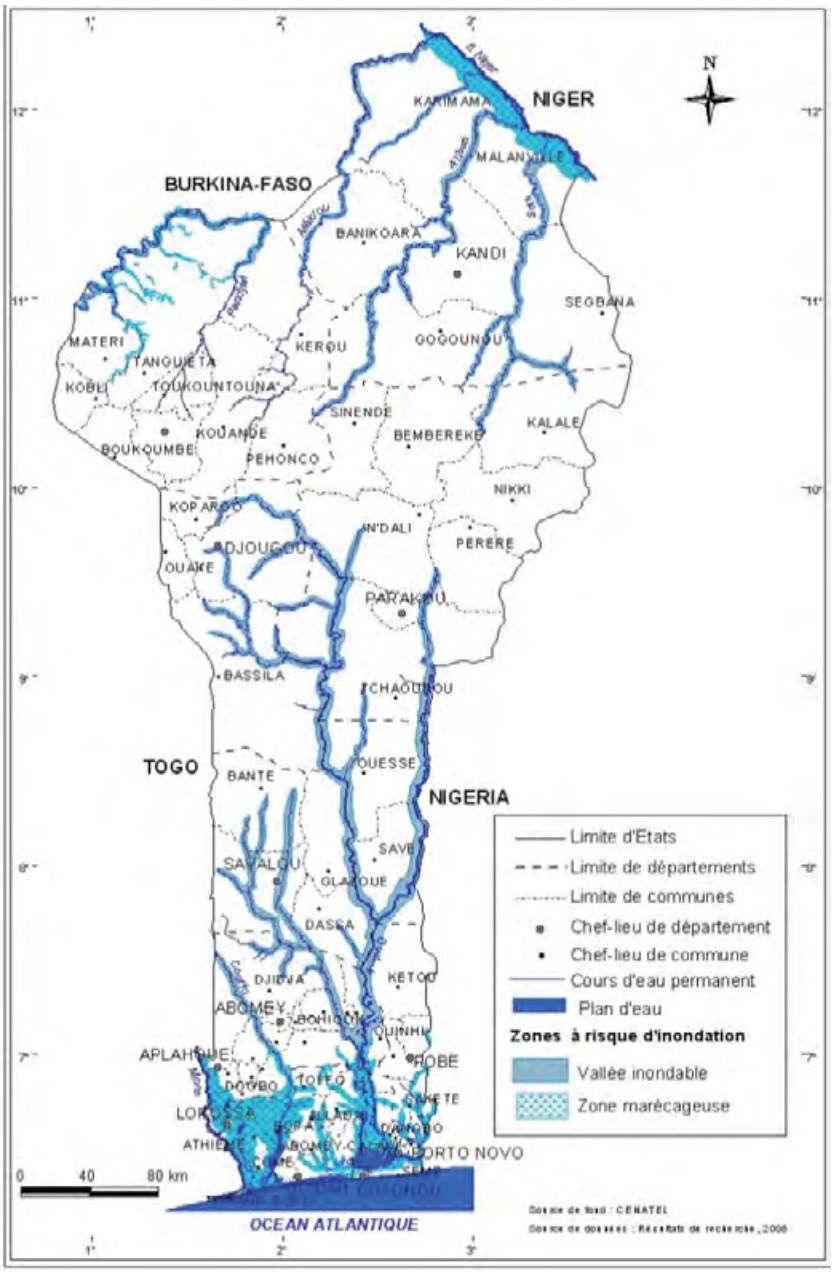

Figure A.2. Flood prone areas in Benin (1/2) (World Bank, 2011

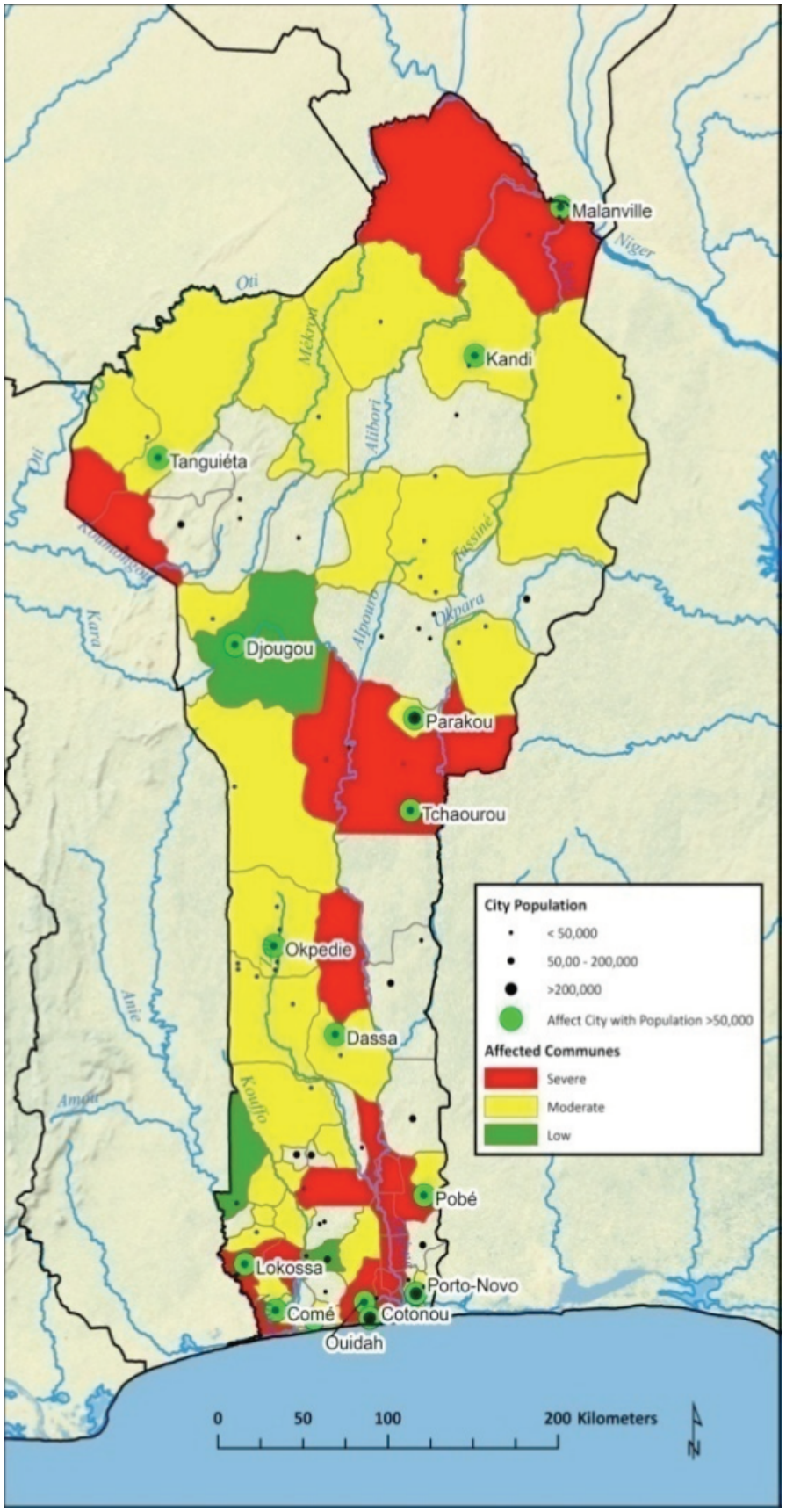

Figure A.3. Flood prone areas in Benin (2/2) (World Bank, 2011

B Fundamentals of microwave remote sensing

B.1 Fundamentals of Passive Microwave Remote Sensing

Looking at terrestrial radiance, the first thing that stands out is the low intensity of radiation in the microwave spectrum compared to the visible spectrum. This is the main reason for the need of large antennas to capture terrestrial microwave radiation and its subsequent low spatial resolution. In figure B.1 the atmospheric attenuation of a nominal clear atmosphere is depicted, where one distinguishes the atmospheric constituents and precipitation. Atmospheric microwave attenuation is mainly due to absorption by H_20 and 0_2. For frequencies $<$ 10 GHz, the atmosphere can be considered completely transparent. This is why principally, microwave imagery has been used for earth observation, such as (sea) ice observation, sea winds, soil moisture.

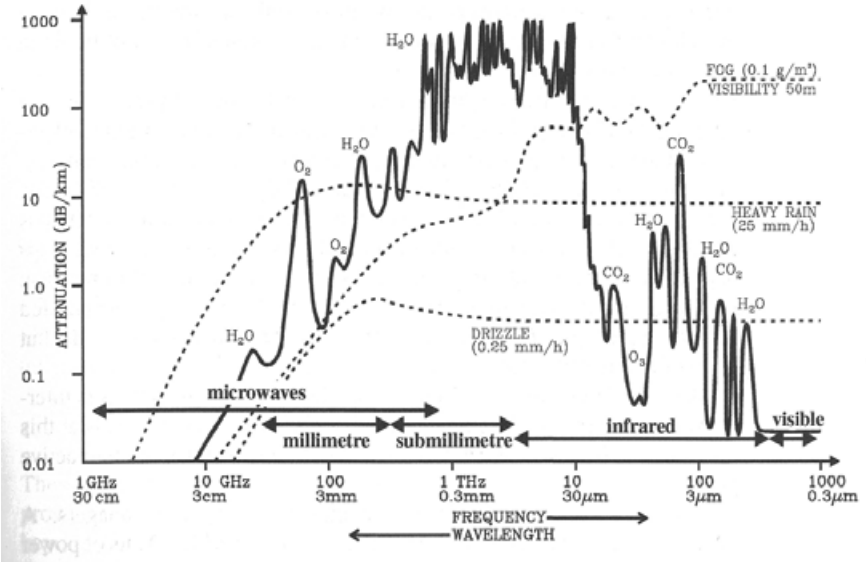

Figure B.1. The attenuation of the atmosphere for a nominal clear atmosphere, with additional attenuation shown for fog, heavy rain and drizzle. Notice the "windows" at optical and microwave frequencies of low attenuation that are used often for terrestrial remote sensing (Woodhouse, 2006).

B.1.1 Blackbody Radiation

An important concept to introduce is blackbody radiation, which in the case of microwaves could better be referred to as thermal radiation. The concept of blackbody radiation tells us that

anything with a physical temperature above the absolute zero will emit some electromagnetic radiation. The Planck Function (B.1) was the first law to describe a relation for the intensity of radiation at different frequencies by any body of temperature T (Woodhouse, 2006).

$$B_\nu(T) = \frac{2h\nu^3}{c^2}\frac{1}{\exp^{\frac{h\nu}{\kappa T}} - 1} \qquad [Wm^{-2}sr^{-1}Hz^{-1}] \tag{B.1}$$

B.1.2 Stephan-Boltzmann Law

Another physical law of importance is the Stephan-Boltzmann law (equation B.2), which shows energy emitted by a blackbody over time is proportional to T^4, which explains the enormous intensity difference between radiation from the (cool) Earth, compared to the Sun (as depicted in Figure 3.6).

$$S = \sigma T^4 \qquad [Wm^{-2}] \tag{B.2}$$

B.1.3 Wien's displacement Law

Furthermore, Wien´s displacement law (equation B.3) describes that the wavelength of the spectral peak is proportional to T^{-1}, which tells us that cooler objects have their peak of radiative energy at longer wavelengths.

$$\nu_{max} \approx T\, x\, 5.876x10^{10} \qquad [K^{-1}s^{-1}] \tag{B.3}$$

B.1.4 Rayleigh-Jeans Approximation

Microwave radiometers are used for terrestrial observation because the atmospheric attenuation is low in the microwave domain, depicted in figure B.1. This means that the intensity of terrestrial radiation picked up through remote sensing (i.e. observed by satellites) is relatively high for these frequencies (as well as the optical frequencies). The radiative energy can be described by the Planck law and the Rayleigh-Jeans approximation is a convenient approximation (equation B.4) of the Planck Law intended for the lower frequencies in the microwave domain, which holds for wavelengths $\lambda >> \lambda_{max}$. At a frequency of 300 GHz for example, Rayleigh-Jeans is valid for wavelengths larger than 2.57 mm. In comparison, 37 GHz corresponds to a wavelength of approximately 8 mm, hence the R-J holds.

$$T_B(\nu) \equiv \left(\frac{c^2}{2\nu^2\kappa}\right)B_\nu = \left(\frac{\lambda^2}{2\kappa}\right)B_\nu \qquad [K] \tag{B.4}$$

B.2 Bands

Microwave frequency bands			
Designation	Frequency range	Wavelength range	Typical uses
L band	1 to 2 GHz	15 cm to 30 cm	military telemetry, GPS, mobile phones (GSM), amateur radio
S band	2 to 4 GHz	7.5 cm to 15 cm	weather radar, surface ship radar, and some communications satellites (microwave ovens, microwave devices/communications, radio astronomy, mobile phones, wireless LAN, Bluetooth, ZigBee, GPS, amateur radio)
C band	4 to 8 GHz	3.75 cm to 7.5 cm	long-distance radio telecommunications
X band	8 to 12 GHz	25 mm to 37.5 mm	satellite communications, radar, terrestrial broadband, space communications, amateur radio, molecular rotational spectroscopy
Ku band	12 to 18 GHz	16.7 mm to 25 mm	satellite communications, molecular rotational spectroscopy
K band	18 to 26.5 GHz	11.3 mm to 16.7 mm	radar, satellite communications, astronomical observations, automotive radar, molecular rotational spectroscopy
Ka band	26.5 to 40 GHz	5.0 mm to 11.3 mm	satellite communications, molecular rotational spectroscopy
Q band	33 to 50 GHz	6.0 mm to 9.0 mm	satellite communications, terrestrial microwave communications, radio astronomy, automotive radar, molecular rotational spectroscopy
U band	40 to 60 GHz	5.0 mm to 7.5 mm	
V band	50 to 75 GHz	4.0 mm to 6.0 mm	millimeter wave radar research, molecular rotational spectroscopy and other kinds of scientific research
W band	75 to 110 GHz	2.7 mm to 4.0 mm	satellite communications, millimeter-wave radar research, military radar targeting and tracking applications, and some non-military applications, automotive radar
F band	90 to 140 GHz	2.1 mm to 3.3 mm	SHF transmissions: Radio astronomy, microwave devices/communications, wireless LAN, most modern radars, communications satellites, satellite television broadcasting, DBS, amateur radio
D band	110 to 170 GHz	1.8 mm to 2.7 mm	EHF transmissions: Radio astronomy, high-frequency microwave radio relay, microwave remote sensing, amateur radio, directed-energy weapon, millimeter wave scanner

Figure B.2. Microwave bands, the ones on the AMSR-E mission are highlighted

B.3 Level 0-4

Data processing level	
Level	Description
0	Reconstructed unprocessed instrument data at full resolutions
1a	Reconstructed unprocessed instrument data at full resolution, time referenced, and annotated with ancillary information, including radiometric and geometric calibration coefficients and georeferencing parameters (i.e., platform ephemeris) computed and appended but not applied to the Level 0 data.
1b	Data that has been processed to sensor units (i.e., radar backscatter cross section, brightness temperature, etc.). Not all instruments will have a Level I B equivalent.
2	Derived environmental variables (e.g., ocean wave height, soil moisture, ice concentration) at the same resolution and location as the Level I source data.
3	Variables mapped on uniform space-time grid scales, usually with some completeness, and consistency properties (e.g., missing points interpolated, complete regions mosaicked together from multiple orbits)
4	Model output or results from analyses of lower-level data (i.e., variables that were not measured by the instruments but instead are derived from these measurements).

Figure B.3. Data processing levels. NSIDC MEaSUREs data is available on L3 (**NASA1986**)

B.4 Downscaling and re-gridding

From the original footprint resolution, some datasets re-grid the available imagery to provide a consistent grid for several satellite missions, which would normally vary. The two types of algorithms used by the MEaSUREs dataset, which is used in this thesis are a drop-in-the-bucket GRD and the SIR algorithm (**Long2016**). Detailed information about the principle will not be discussed in this research, but it is important to note the differences in practice.

The GRD algorithm (Figure B.4) includes the brightness temperature from the original footprint pixel if the centerline of the pixel is located within the boundaries of the predetermined grid cell, in this research the EASE 2.0 Grid. In the case of Ka-band imagery one does not speak of downscaling, but rather of re-gridding, since the original spatial resolution of the footprint (14 x 7 km) is increased to a 25 km cell product. Despite the large scale, the GRD method might include noise from surrounding pixels, similar to downscaling effects.

The SIR algorithm (Figure B.5) uses the principle of overlapping pixels to downscale the original footprint to a 3.125 km cell product. It is furthermore based on the fact that the signal of the original footprint is for a larger part determined by the center of the pixel than the sides.

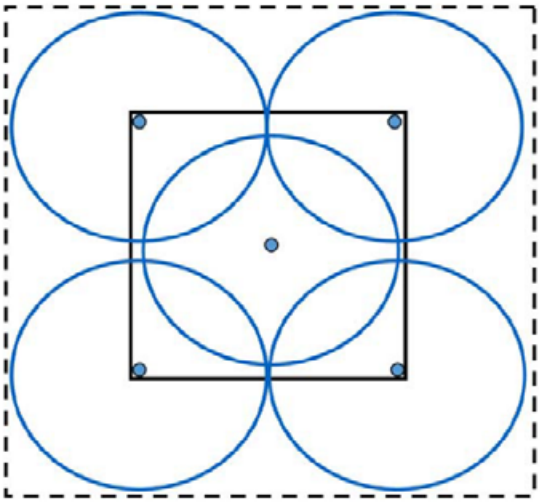

Figure B.4. GRD re-gridding illustration (**Long2016**

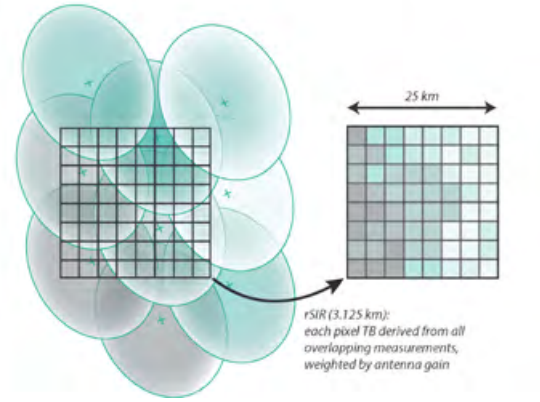

Figure B.5. Illustration of the SIR method used to create the MEaSUREs EASE2.0 grid resulting in downscaling 10 km footprint to 3.125 km tiles. **Long2016**

.

Fieldwork

C

C.1 Interviews

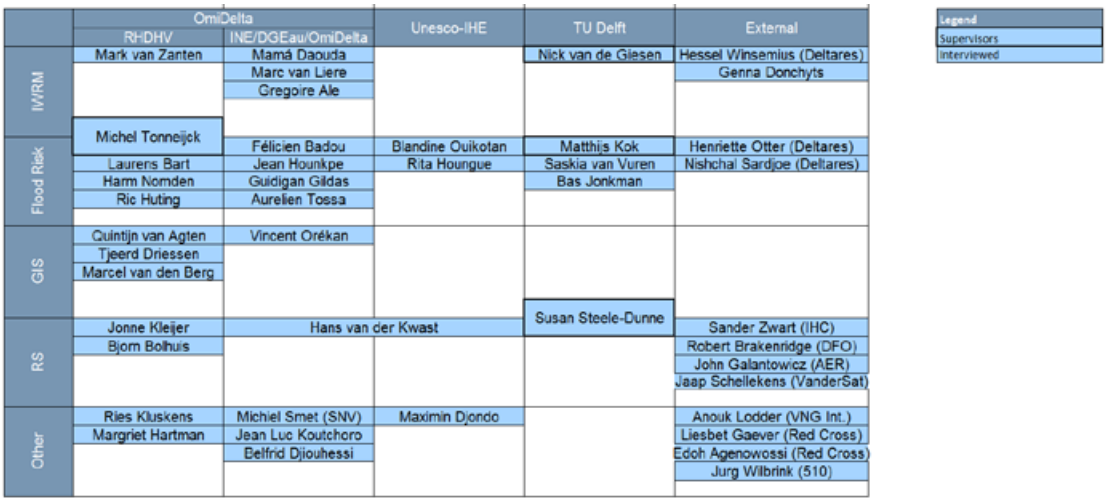

Figure C.1. Interviews held for this research (own work)

C.2 Impression of fieldwork

(a) Inundating floodplains at the Dome discharge station (1/2) (own work)

(b) Inundating floodplains at the Dome discharge station (2/2) (own work)

(c) Taking 2010 flood mark measurements (own work)

(d) Eroded soil and trees resulting from previous floods (own work)

(e) Dwellings on lake Nokoue (own work)

(f) Small town built along the Oueme River (own work)

Figure C.2. Pictures taken during fieldwork in the Oueme Delta in July-August 2018. (a,b) Start of the inundation season: floodplains filling up. (c) Clear flood-marks from the 2010 inundations visible. Taking water level measurements. (d) Eroded soil visible at the root of a tree, at the moment still located far above the water level (e) Dwellings in and near lake Nokoue (f). Typical image of a town in the delta, built in the vicinity of the river. (own work)

C.3 Discharge stations

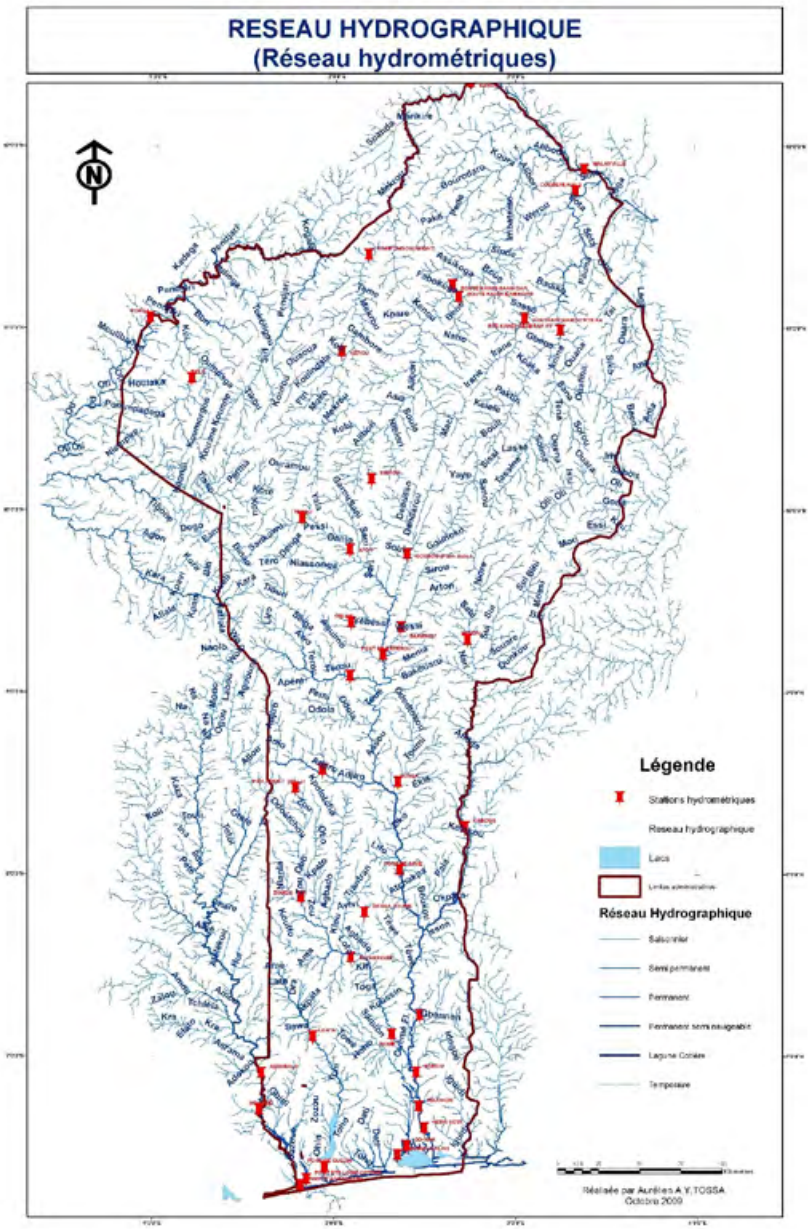

Figure C.3. Discharge stations in the Oueme catchment (from DG-Eau)

C.4 Inundation Extent Survey

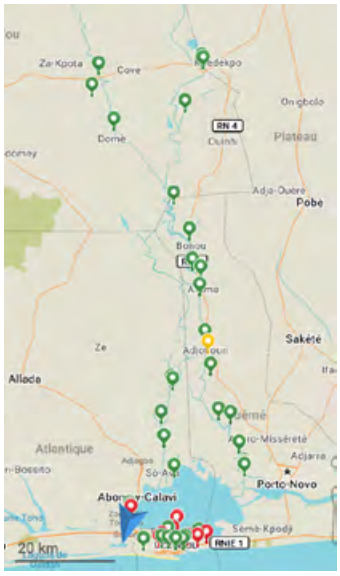

(a) Measurement locations of 2010 flood marks during fieldwork in July-August 2018 (**MAPS.ME2018**)

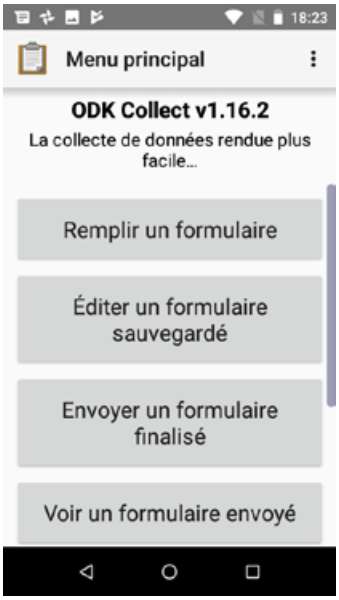

(b) Screenshot ODK-Collect Survey (1/5) (**OpenDataKit2017**)

(c) Screenshot ODK-Collect Survey (2/5) (**OpenDataKit2017**)

(d) Screenshot ODK-Collect Survey (3/5) (**OpenDataKit2017**)

(e) Screenshot ODK-Collect Survey (4/5) (**OpenDataKit2017**)

(f) Screenshot ODK-Collect Survey (5/5) (**OpenDataKit2017**)

Figure C.4. Screenshots of the locations of 2010 flood marks and the ODK-Collect survey used for fieldwork in July-August 2018. A comprehensive installation guide and user manual in French is available at the author (**OpenDataKit2017**)

.

CMC-ratio

D

The CMC-ratio is the core of the IEM: it estimates a percentage surface water in a given cell and provides information about the timing of inundations. This chapter serves as background information on the input data used by the CMC-ratio (i.e. $T - B$), and performance of the current method.

D.1 Scale Estimation Method - Fixed Wet Cell

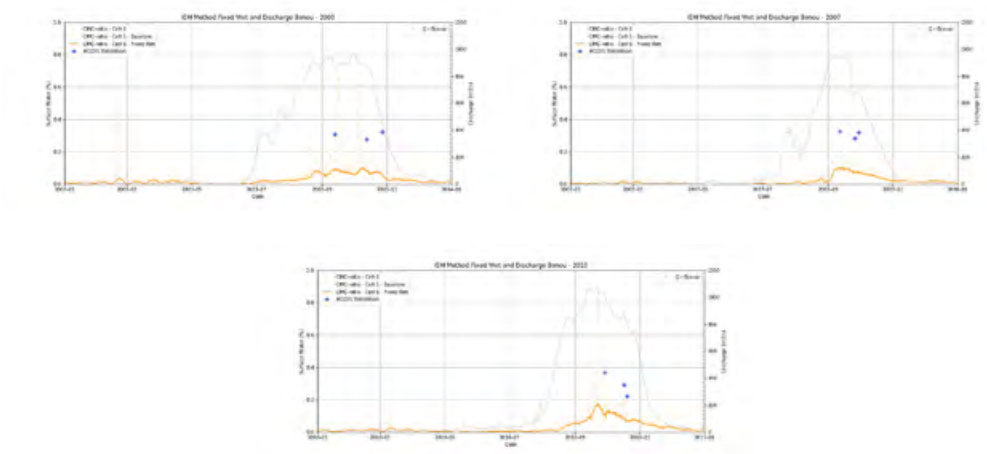

Figure D.1. r_{CMC} Fixed Wet Cell Method and MODIS validation points for 2003, 2007 and 2010

D.2 Scale Estimation Method - Full

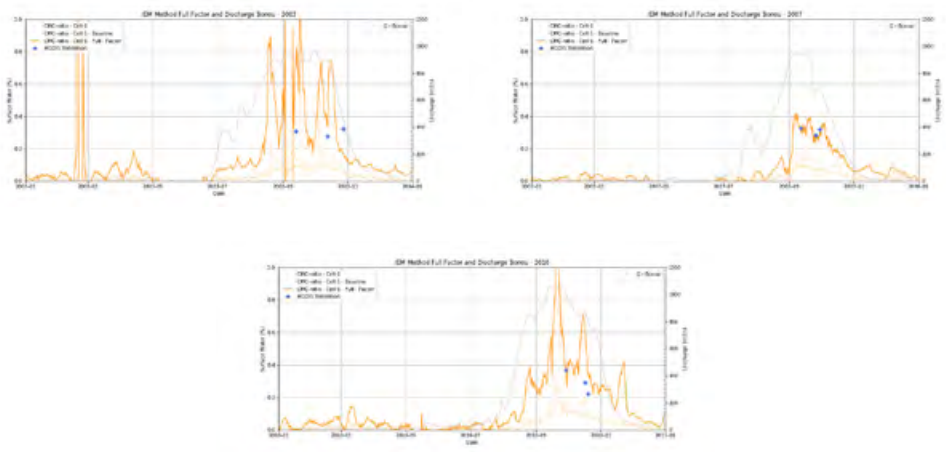

Figure D.2. r_{CMC} Full-Factor Method and MODIS validation points for 2003, 2007 and 2010

D.3 Scale Estimation Method - Offset

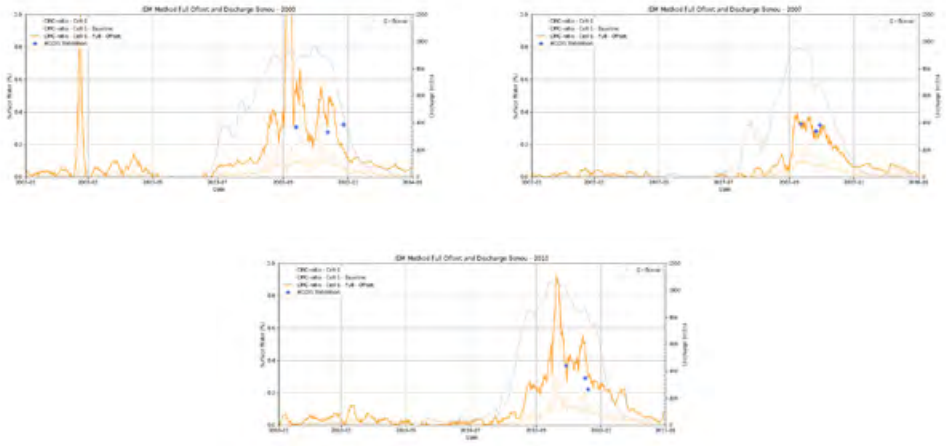

Figure D.3. r_{CMC} Full-Offset Method and MODIS validation points for 2003, 2007 and 2010

D.4 Scale Estimation Method - Hybrid

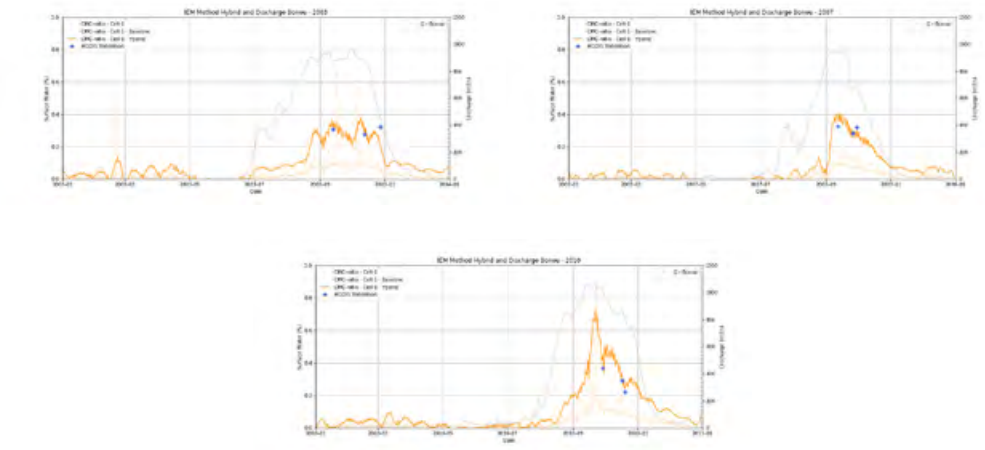

Figure D.4. r_{CMC} Hybrid Method and MODIS validation points for 2003, 2007 and 2010

			Validation	CMC-Baseline		CMC-Hybrid	
Type			MODIS	CMC	Accuracy	CMC	Accuracy
Units			%	%	%	%	%
Date	Sensor	Cell					
26-9-2003	AMSR-E	1	1.12	-2.69	-240.04	7.69	-485.15
3-10-2003	AMSR-E	1	1.59	1.32	83.01	-4.02	-252.38
28-10-2003	AMSR-E	1	24.37	-0.67	-2.76	2.30	9.44
12-9-2007	ASMR-E	1	2.92	0.65	22.35	-2.12	-72.69
26-9-2007	ASMR-E	1	5.53	1.07	19.42	-3.40	-61.35
30-9-2007	ASMR-E	1	1.54	-2.04	-132.31	6.08	-194.95
29-9-2010	AMSR-E	1	2.50	-2.59	-103.57	7.63	-105.50
17-10-2010	AMSR-E	1	1.22	0.80	65.57	-2.36	-194.03
20-10-2010	AMSR-E	1	7.70	0.87	11.27	-2.67	-34.72
Average	AMSRE	1			-30.78		-154.59
SD					99.74		141.85

Figure D.5. Cell 1 - Validation days, Baseline and Hybrid method (own work)

			Validation	CMC-Baseline		CMC-Hybrid	
Type			MODIS	CMC	Accuracy	CMC	Accuracy
Units			%	%	%	%	%
Date	Sensor	Cell					
26-9-2003	AMSR-E	2	4.09	0.31	7.56	-3.02	-73.73
3-10-2003	AMSR-E	2	5.39	-2.78	-51.57	19.05	-153.58
28-10-2003	AMSR-E	2	5.48	-0.65	-11.93	7.36	65.58
12-9-2007	ASMR-E	2	4.06	-0.90	-22.07	7.92	4.95
26-9-2007	ASMR-E	2	10.07	-2.02	-20.11	15.14	49.57
30-9-2007	ASMR-E	2	3.75	-1.34	-35.57	10.66	-83.98
29-9-2010	AMSR-E	2	6.02	-0.18	-2.95	1.62	26.90
17-10-2010	AMSR-E	2	4.19	0.53	12.61	-2.70	-64.37
20-10-2010	AMSR-E	2	4.17	0.20	4.77	-0.88	-21.09
Average	AMSR-E	2			-13.25		-27.75
SD					20.07		67.69

Figure D.6. Cell 2 - Validation days, Baseline and Hybrid method (own work)

			Validation	CMC-Baseline		CMC-Hybrid	
Type			MODIS	CMC	Accuracy	CMC	Accuracy
Units			%	%	%	%	%
26-9-2003	AMSR-E	3	3.95	-0.17	-4.28	-0.88	-22.23
3-10-2003	AMSR-E	3	4.74	4.48	94.41	18.55	-191.24
28-10-2003	AMSR-E	3	6.67	1.91	28.57	8.94	66.05
12-9-2007	ASMR-E	3	8.51	2.19	25.74	10.87	72.32
26-9-2007	ASMR-E	3	9.37	1.51	16.11	6.99	74.64
30-9-2007	ASMR-E	3	7.41	-0.09	-1.20	-0.47	-6.38
29-9-2010	AMSR-E	3	7.24	0.48	6.69	2.67	36.94
17-10-2010	AMSR-E	3	6.34	0.85	13.47	3.70	58.37
20-10-2010	AMSR-E	3	6.34	0.66	10.36	3.02	47.55
Average	AMSR-E	3			21.10		15.11
SD					20.07		67.69

Figure D.7. Cell 3 - Validation days, Baseline and Hybrid method (own work)

			Validation	CMC-Baseline		CMC-Hybrid	
Type			MODIS	CMC	Accuracy	CMC	Accuracy
Units			%	%	%	%	%
26-9-2003	AMSR-E	4	27.12	7.78	28.69	29.20	92.34
3-10-2003	AMSR-E	4	24.85	4.42	17.78	17.01	68.43
28-10-2003	AMSR-E	4	25.99	4.79	18.42	18.26	70.26
12-9-2007	ASMR-E	4	27.27	7.83	28.72	30.80	87.06
26-9-2007	ASMR-E	4	21.19	7.05	33.29	25.44	79.94
30-9-2007	ASMR-E	4	25.86	7.05	27.25	27.69	92.93
29-9-2010	AMSR-E	4	26.70	7.52	28.17	29.77	88.51
17-10-2010	AMSR-E	4	24.30	8.22	33.82	27.69	86.06
20-10-2010	AMSR-E	4	22.69	5.45	24.02	19.52	86.06
Average	AMSR-E	4			26.68		83.51
SD					5.37		8.39

Figure D.8. Cell 4 - Validation days, Baseline and Hybrid method (own work)

			Validation	CMC-Baseline		CMC-Hybrid	
Type			MODIS	CMC	Accuracy	CMC	Accuracy
Units			%	%	%	%	%
26-9-2003	AMSR-E	5	2.81	0.75	26.61	1.92	68.25
3-10-2003	AMSR-E	5	2.63	4.79	18.12	10.68	-205.63
28-10-2003	AMSR-E	5	4.15	3.52	84.82	8.87	-13.61
12-9-2007	ASMR-E	5	4.99	0.52	10.50	1.37	27.48
26-9-2007	ASMR-E	5	2.51	-0.13	-5.17	-0.31	-12.53
30-9-2007	ASMR-E	5	4.34	0.18	4.22	0.49	11.21
29-9-2010	AMSR-E	5	2.82	1.60	56.96	4.38	44.40
17-10-2010	AMSR-E	5	1.86	0.48	25.65	1.09	58.79
20-10-2010	AMSR-E	5	2.44	-0.76	-31.26	-1.85	-75.94
Average	AMSR-E	5			21.16		-10.84
SD					32.03		80.48

Figure D.9. Cell 5 - Validation days, Baseline and Hybrid method (own work)

			Validation	CMC-Baseline		CMC-Hybrid	
Type			MODIS	CMC	Accuracy	CMC	Accuracy
Units			%	%	%	%	%
26-9-2003	AMSR-E	6	30.79	7.34	23.84	28.53	92.68
3-10-2003	AMSR-E	6	27.56	6.37	23.11	23.46	85.10
28-10-2003	AMSR-E	6	22.76	5.17	22.70	20.41	89.66
12-9-2007	ASMR-E	6	32.62	9.66	29.61	38.66	81.48
26-9-2007	ASMR-E	6	28.11	6.64	23.60	24.36	86.66
30-9-2007	ASMR-E	6	32.02	7.22	22.55	29.17	91.09
29-9-2010	AMSR-E	6	36.67	10.78	29.41	43.54	81.27
17-10-2010	AMSR-E	6	29.26	9.39	32.10	32.29	89.65
20-10-2010	AMSR-E	6	22.05	6.54	29.64	23.63	92.86
Average	AMSR-E	6			26.29		87.83
SD					3.59		4.20

Figure D.10. Cell 6 - Validation days, Baseline and Hybrid method (own work)

			Validation	CMC-Baseline		CMC-Hybrid	
Type			MODIS	CMC	Accuracy	CMC	Accuracy
Units			%	%	%	%	%
26-9-2003	AMSR-E	8	29.75	7.04	23.67	28.82	96.89
3-10-2003	AMSR-E	8	23.70	6.41	27.05	24.85	95.15
28-10-2003	AMSR-E	8	28.49	5.95	20.90	25.57	89.76
12-9-2007	ASMR-E	8	42.02	8.16	19.42	34.18	81.35
26-9-2007	ASMR-E	8	29.86	6.41	21.48	25.20	84.38
30-9-2007	ASMR-E	8	33.80	7.71	22.82	33.20	98.22
29-9-2010	AMSR-E	8	54.64	15.87	29.05	66.05	79.11
17-10-2010	AMSR-E	8	39.76	12.23	30.77	44.10	89.08
20-10-2010	AMSR-E	8	32.34	9.48	29.31	35.92	88.93
Average	AMSR-E	8			24.94		89.21
SD					3.93		6.35

Figure D.11. Cell 8 - Validation days, Baseline and Hybrid method (own work)

			Validation	CMC-Baseline		CMC-Hybrid	
Type			MODIS	CMC	Accuracy	CMC	Accuracy
Units			%	%	%	%	%
26-9-2003	AMSR-E	10	36.64	20.29	55.39	38.37	95.27
3-10-2003	AMSR-E	10	33.70	19.03	56.46	32.88	97.58
28-10-2003	AMSR-E	10	34.62	18.26	52.75	35.97	96.09
12-9-2007	ASMR-E	10	45.21	21.28	47.07	40.89	90.43
26-9-2007	ASMR-E	10	35.74	19.68	55.06	35.25	98.61
30-9-2007	ASMR-E	10	45.01	21.03	46.72	41.07	91.24
29-9-2010	AMSR-E	10	58.17	30.77	52.90	60.68	95.69
17-10-2010	AMSR-E	10	42.34	25.77	60.87	43.33	97.66
20-10-2010	AMSR-E	10	42.63	25.71	60.32	45.37	93.57
Average	AMSR-E	10			54.17		95.13
SD					4.71		2.70

Figure D.12. Cell 10 - Validation days, Baseline and Hybrid method (own work)

D.5 Savitzky-Golay Filter

The following figures depict variations in number of days included in the filter and the polynomial order at which the filter estimates (figure D.13, D.14).

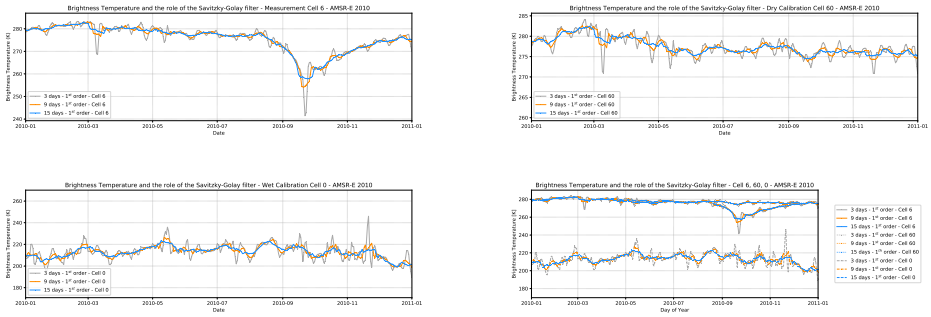

Figure D.13. Brightness temperature and the role of the length of days that the Savitzky-Golay filter uses for Cell (a) 6, (b) 60 and (c) 0 (own work)

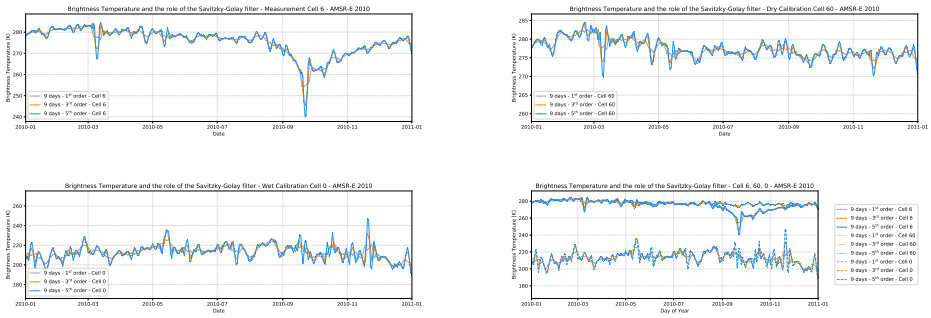

Figure D.14. Brightness temperature and the role of the polynomial order that the Savitzky-Golay filter uses for Cell (a) 6, (b) 60 and (c) 0 (own work).

Inundation Mapping

E

E.1 Measurement Cell 1

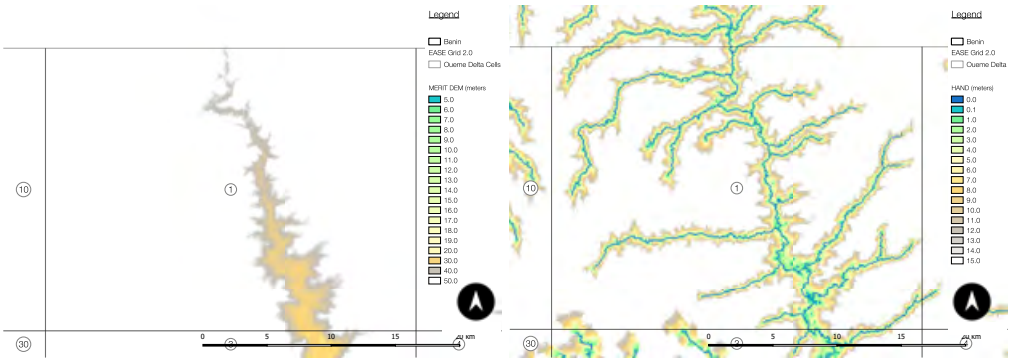

(a) Cell 1 - MERIT DEM

(b) Cell 1 - MERIT HAND

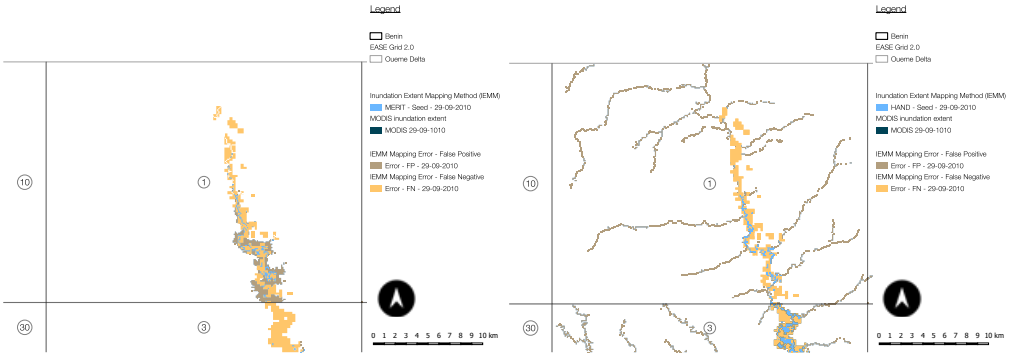

(c) Cell 1 - Mapping DEM seed

(d) Cell 1 - Mapping HAND seed

(e) Cell 1 - Mapping DEM coordinates

(f) Cell 1 - Mapping HAND coordinates

Figure E.1. Measurement cell 1: visualisation of the different mapping methods and the false positive and false negative errors, on two different elevation maps: (a) MERIT DEM and (b) the HAND derived from the MERIT DEM. (c) and (d) show the result without contiguity constraints and (e), (f) depict the result when contiguity constraints based on (manually) given coordinates are included. (own work)

E.2 Measurement Cell 2

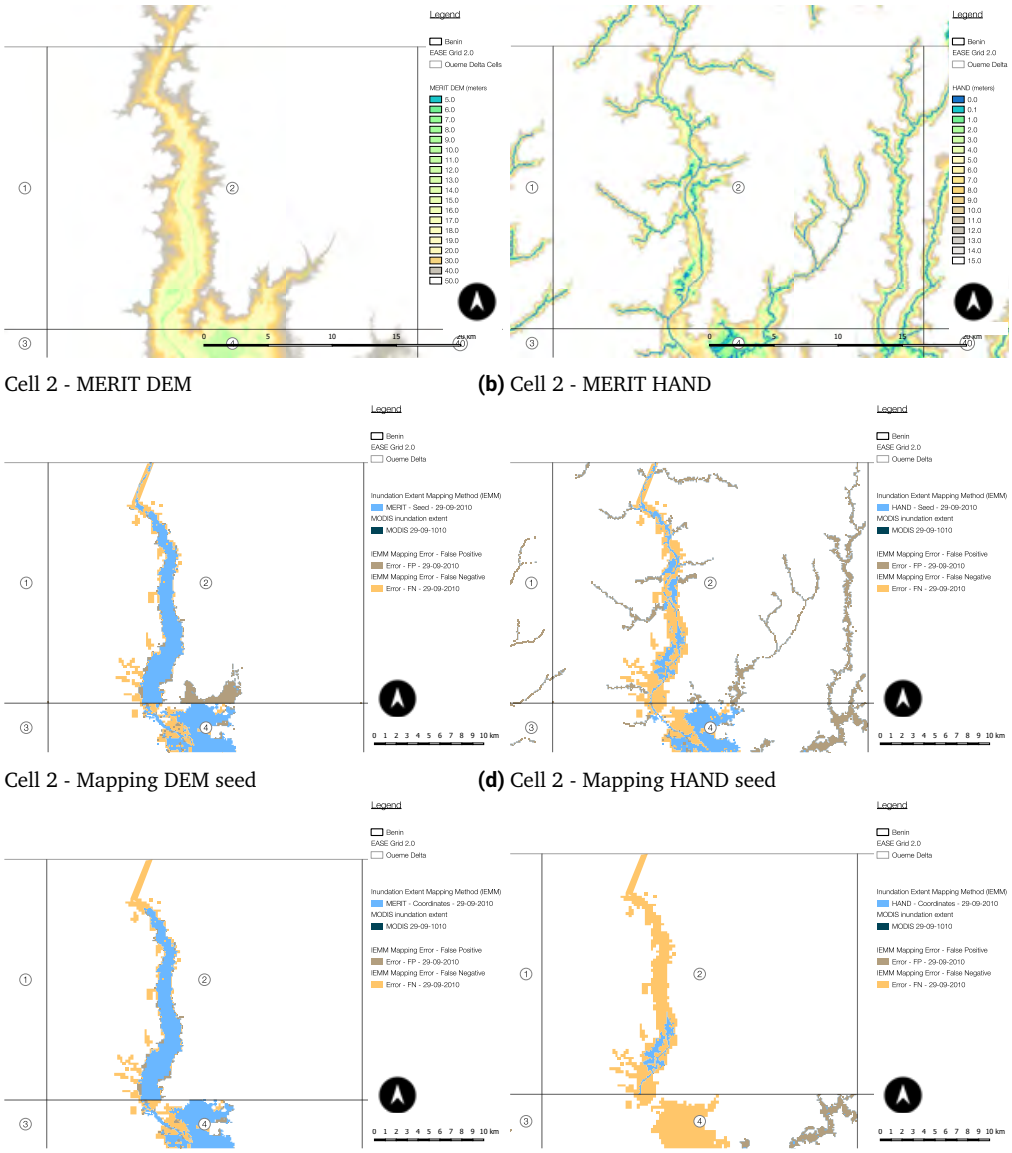

(a) Cell 2 - MERIT DEM

(b) Cell 2 - MERIT HAND

(c) Cell 2 - Mapping DEM seed

(d) Cell 2 - Mapping HAND seed

(e) Cell 2 - Mapping DEM coordinates

(f) Cell 2 - Mapping HAND coordinates

Figure E.2. Measurement cell 2: visualisation of the different mapping methods and the false positive and false negative errors, on two different elevation maps: (a) MERIT DEM and (b) the HAND derived from the MERIT DEM. (c) and (d) show the result without contiguity constraints and (e), (f) depict the result when contiguity constraints based on (manually) given coordinates are included. (own work)

E.3 Measurement Cell 3

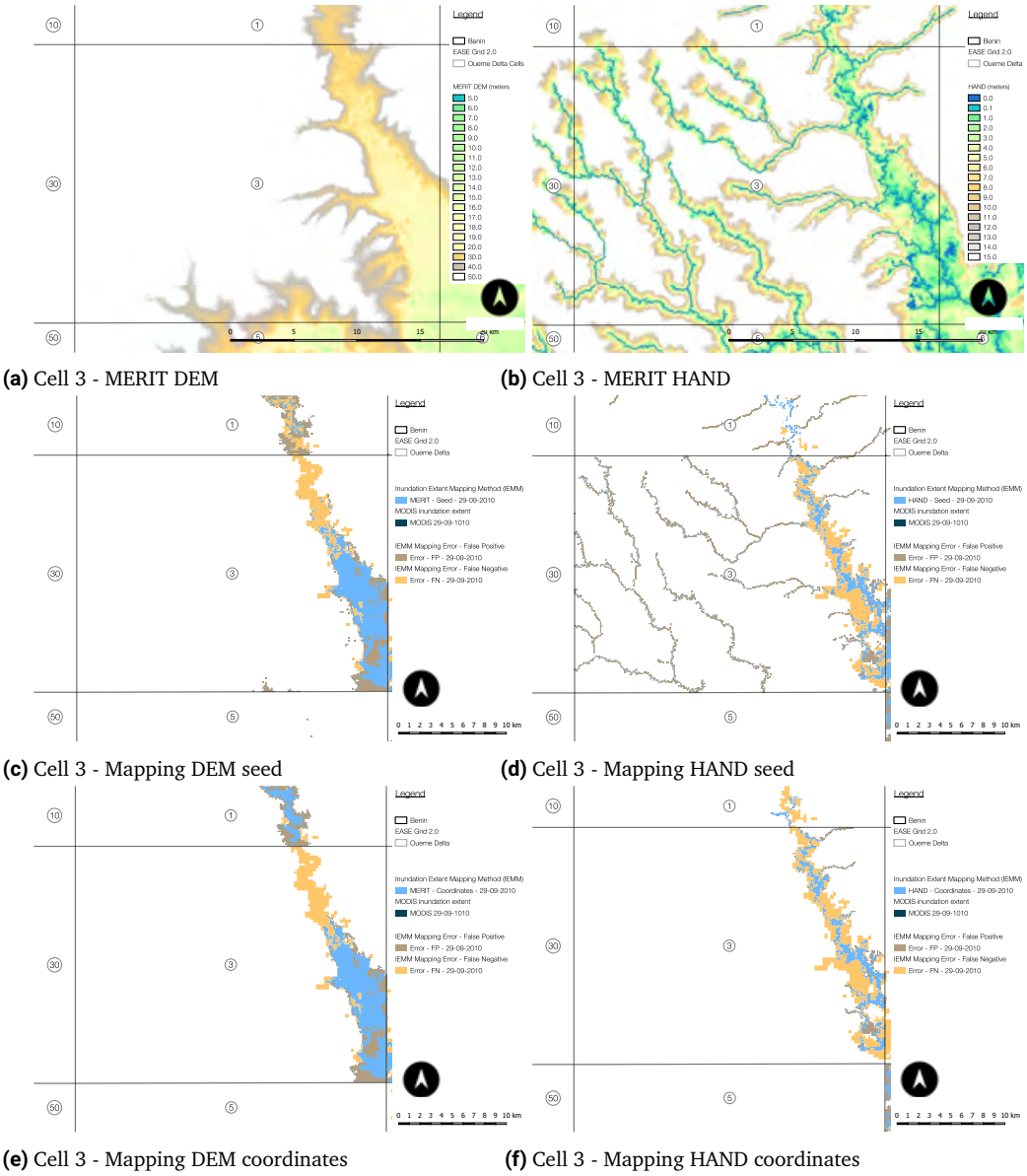

(a) Cell 3 - MERIT DEM

(b) Cell 3 - MERIT HAND

(c) Cell 3 - Mapping DEM seed

(d) Cell 3 - Mapping HAND seed

(e) Cell 3 - Mapping DEM coordinates

(f) Cell 3 - Mapping HAND coordinates

Figure E.3. Measurement cell 3: visualisation of the different mapping methods and the false positive and false negative errors, on two different elevation maps: (a) MERIT DEM and (b) the HAND derived from the MERIT DEM. (c) and (d) show the result without contiguity constraints and (e), (f) depict the result when contiguity constraints based on (manually) given coordinates are included. (own work)

E.4 Measurement Cell 4

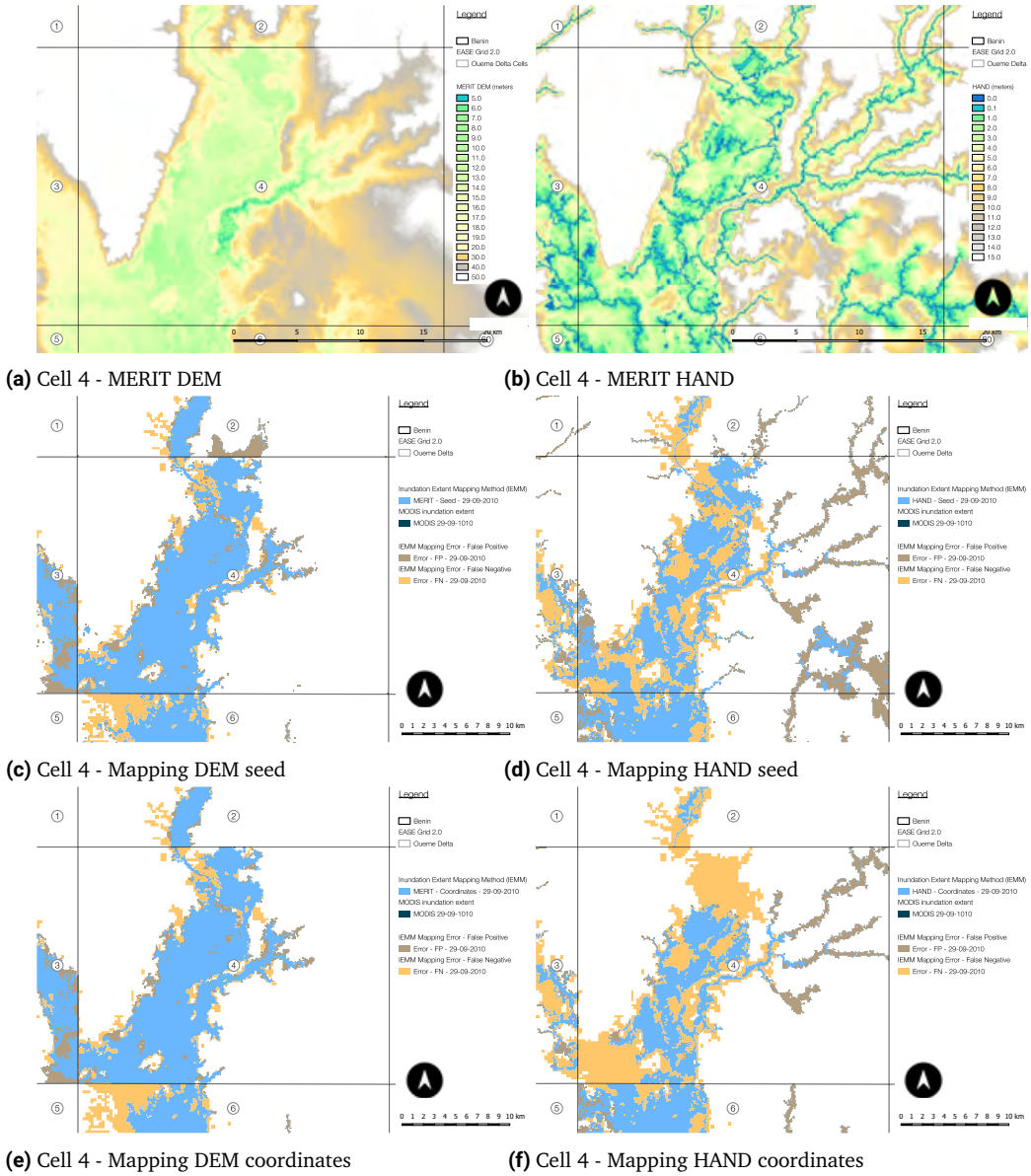

(a) Cell 4 - MERIT DEM

(b) Cell 4 - MERIT HAND

(c) Cell 4 - Mapping DEM seed

(d) Cell 4 - Mapping HAND seed

(e) Cell 4 - Mapping DEM coordinates

(f) Cell 4 - Mapping HAND coordinates

Figure E.4. Measurement cell 4: visualisation of the different mapping methods and the false positive and false negative errors, on two different elevation maps: (a) MERIT DEM and (b) the HAND derived from the MERIT DEM. (c) and (d) show the result without contiguity constraints and (e), (f) depict the result when contiguity constraints based on (manually) given coordinates are included. (own work)

E.5 Measurement Cell 5

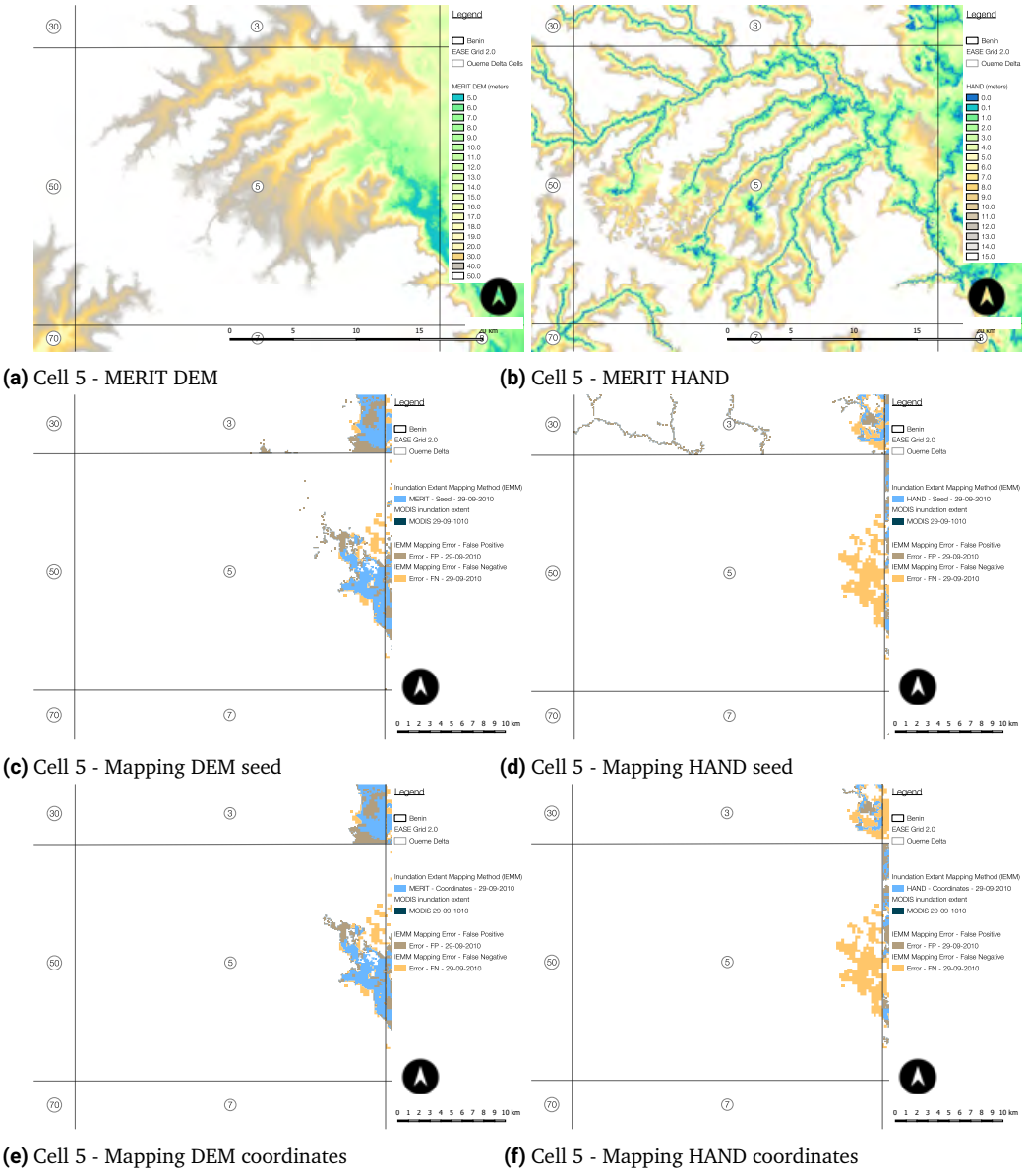

(a) Cell 5 - MERIT DEM

(b) Cell 5 - MERIT HAND

(c) Cell 5 - Mapping DEM seed

(d) Cell 5 - Mapping HAND seed

(e) Cell 5 - Mapping DEM coordinates

(f) Cell 5 - Mapping HAND coordinates

Figure E.5. Measurement cell 5: visualisation of the different mapping methods and the false positive and false negative errors, on two different elevation maps: (a) MERIT DEM and (b) the HAND derived from the MERIT DEM. (c) and (d) show the result without contiguity constraints and (e), (f) depict the result when contiguity constraints based on (manually) given coordinates are included. (own work)

E.6 Measurement Cell 6

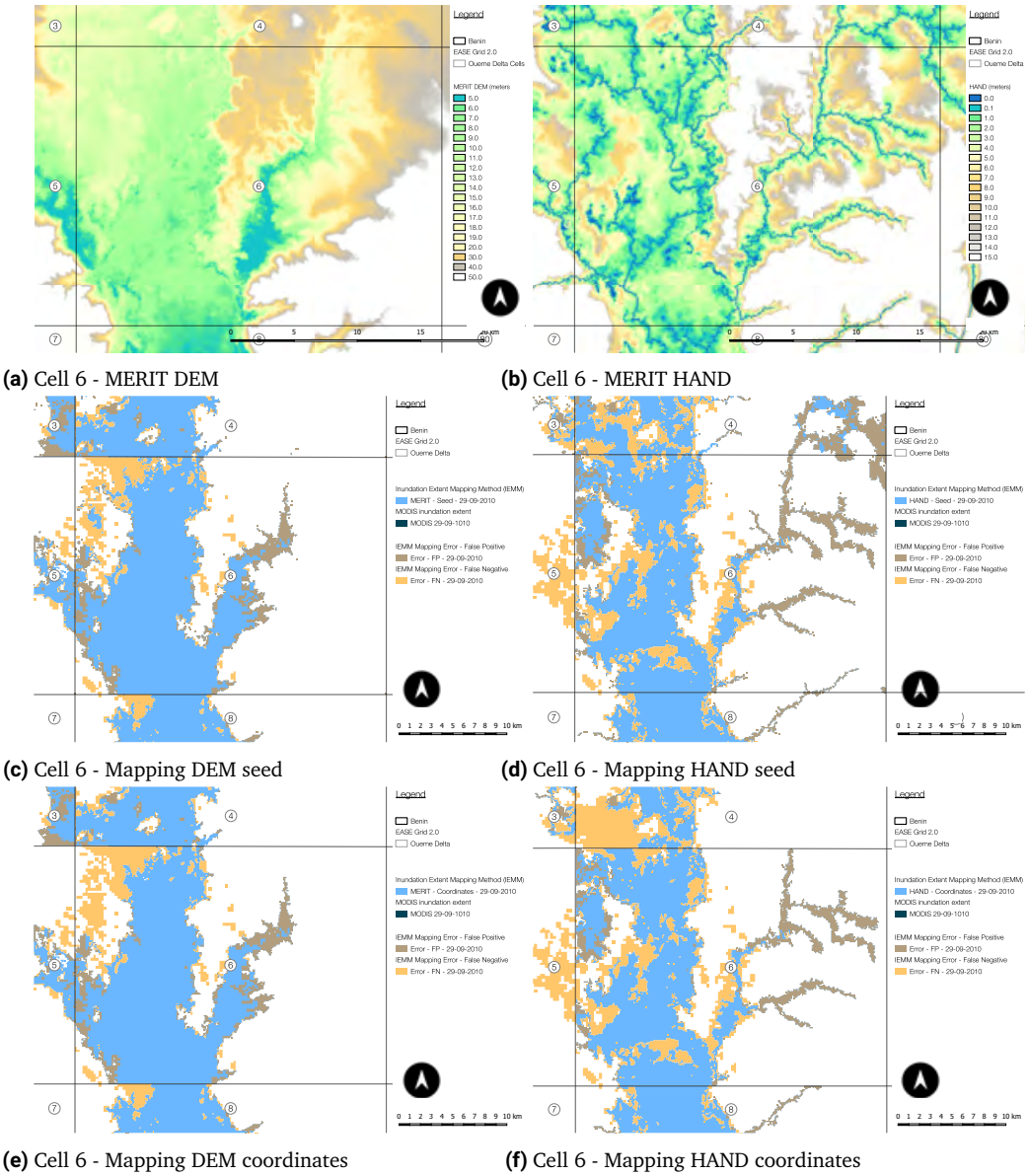

(a) Cell 6 - MERIT DEM

(b) Cell 6 - MERIT HAND

(c) Cell 6 - Mapping DEM seed

(d) Cell 6 - Mapping HAND seed

(e) Cell 6 - Mapping DEM coordinates

(f) Cell 6 - Mapping HAND coordinates

Figure E.6. Measurement cell 6: visualisation of the different mapping methods and the false positive and false negative errors, on two different elevation maps: (a) MERIT DEM and (b) the HAND derived from the MERIT DEM. (c) and (d) show the result without contiguity constraints and (e), (f) depict the result when contiguity constraints based on (manually) given coordinates are included. (own work)

E.7 Measurement Cell 8

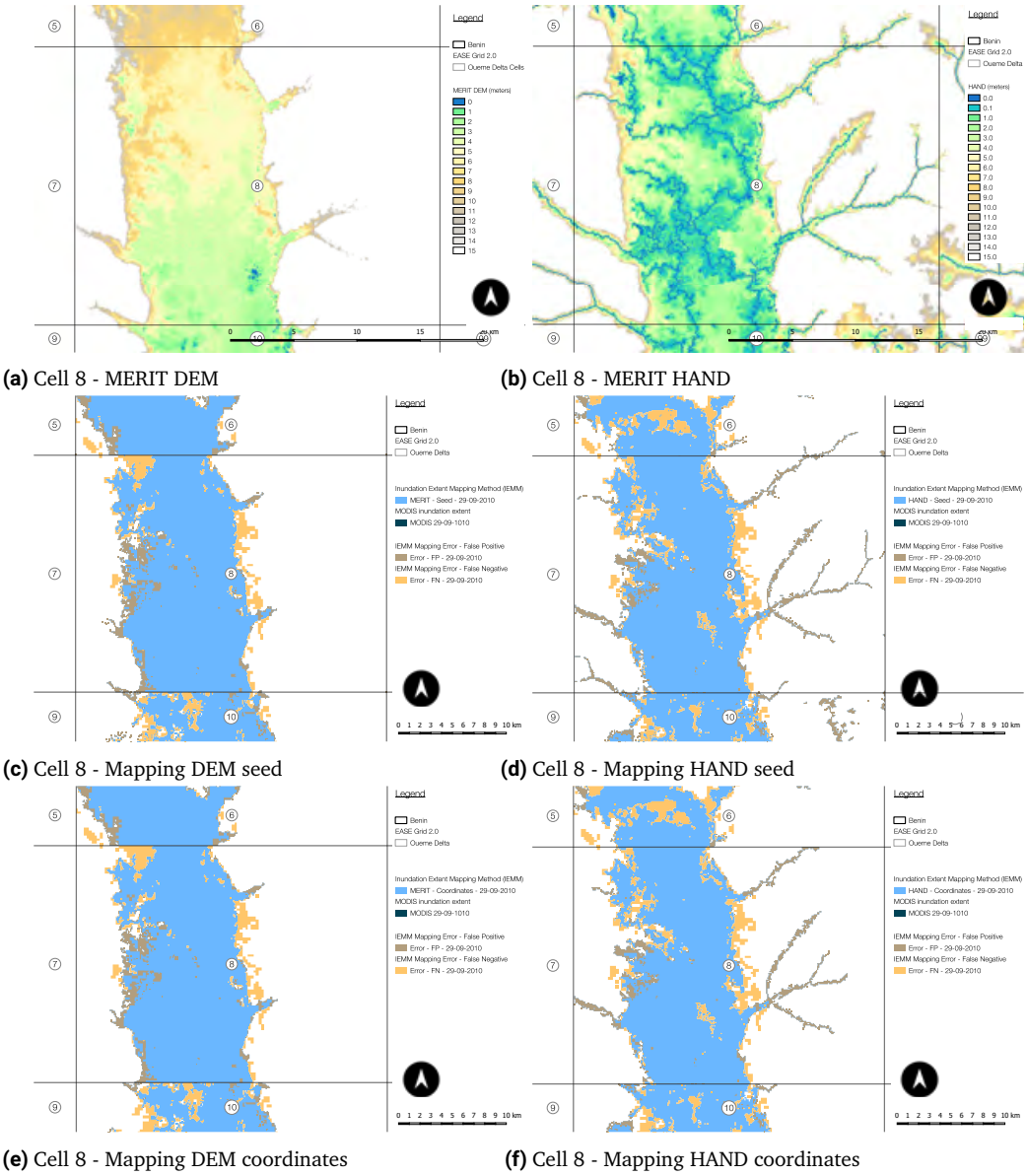

(a) Cell 8 - MERIT DEM **(b)** Cell 8 - MERIT HAND

(c) Cell 8 - Mapping DEM seed **(d)** Cell 8 - Mapping HAND seed

(e) Cell 8 - Mapping DEM coordinates **(f)** Cell 8 - Mapping HAND coordinates

Figure E.7. Measurement cell 8: visualisation of the different mapping methods and the false positive and false negative errors, on two different elevation maps: (a) MERIT DEM and (b) the HAND derived from the MERIT DEM. (c) and (d) show the result without contiguity constraints and (e), (f) depict the result when contiguity constraints based on (manually) given coordinates are included. (own work)

E.8 Measurement Cell 10

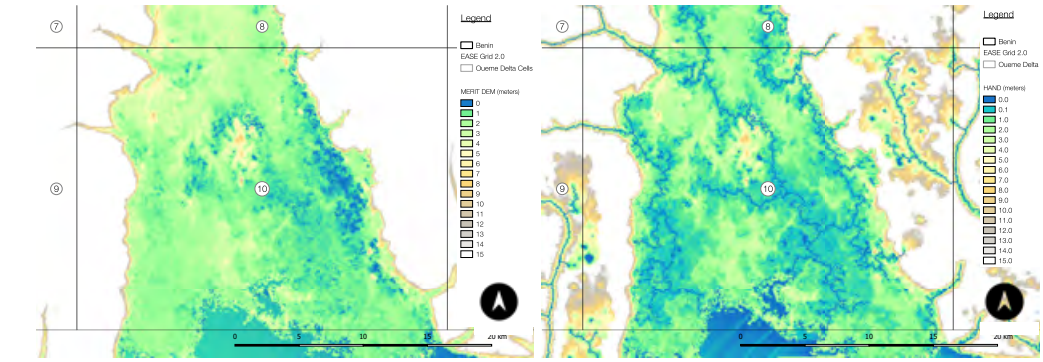

(a) Cell 10 - MERIT DEM

(b) Cell 10 - MERIT HAND

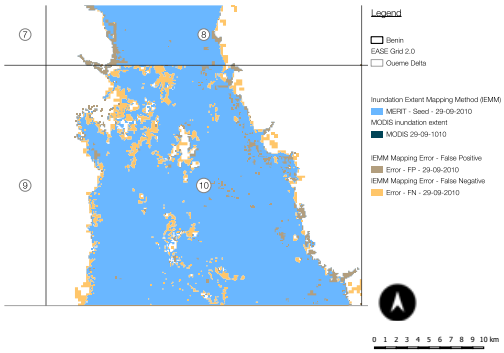

(c) Cell 10 - Mapping DEM seed

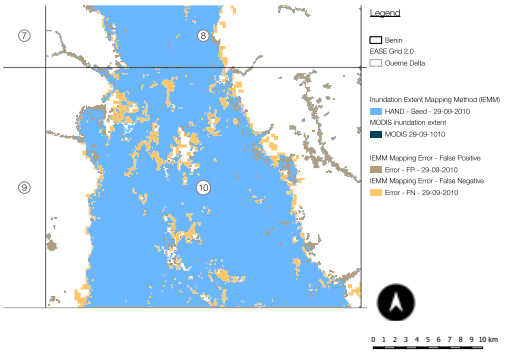

(d) Cell 10 - Mapping HAND seed

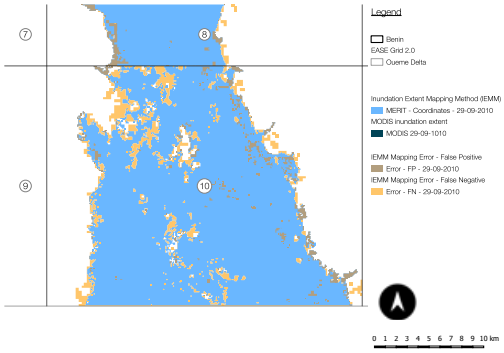

(e) Cell 10 - Mapping DEM coordinates

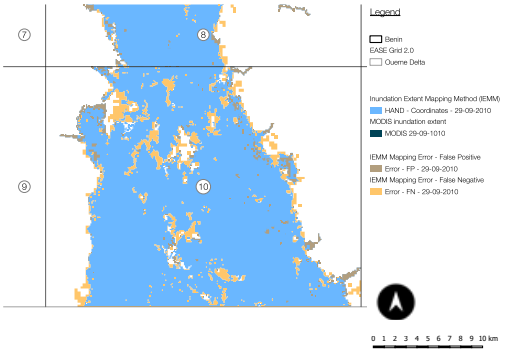

(f) Cell 10 - Mapping HAND coordinates

Figure E.8. Measurement cell 10: visualisation of the different mapping methods and the false positive and false negative errors, on two different elevation maps: (a) MERIT DEM and (b) the HAND derived from the MERIT DEM. (c) and (d) show the result without contiguity constraints and (e), (f) depict the result when contiguity constraints based on (manually) given coordinates are included. (own work)

E.9 Mapping Errors relative to Grid Cell (EASE)

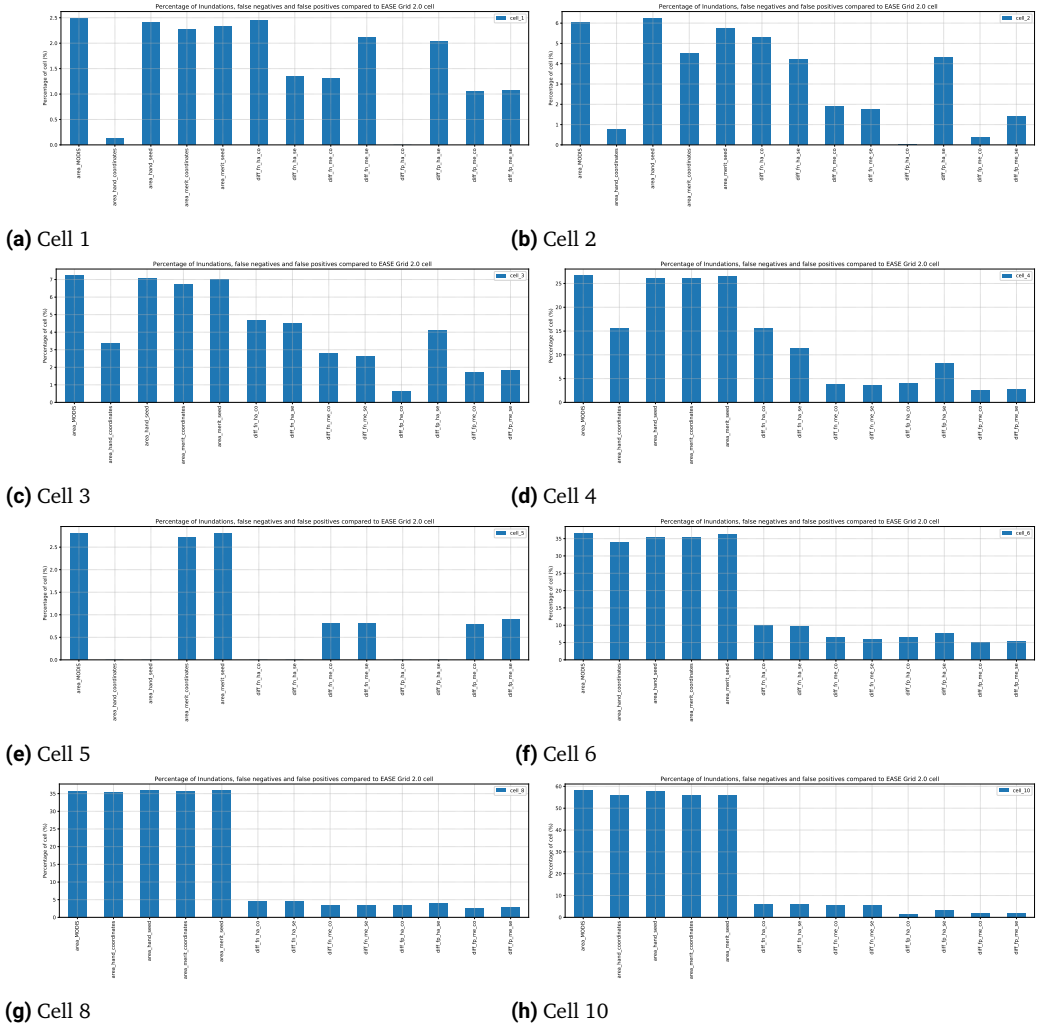

(a) Cell 1 **(b)** Cell 2

(c) Cell 3 **(d)** Cell 4

(e) Cell 5 **(f)** Cell 6

(g) Cell 8 **(h)** Cell 10

Figure E.9. Mapping errors relative to the EASE Grid 2.0 (own work)

E.10 Mapping Errors relative to MODIS validation

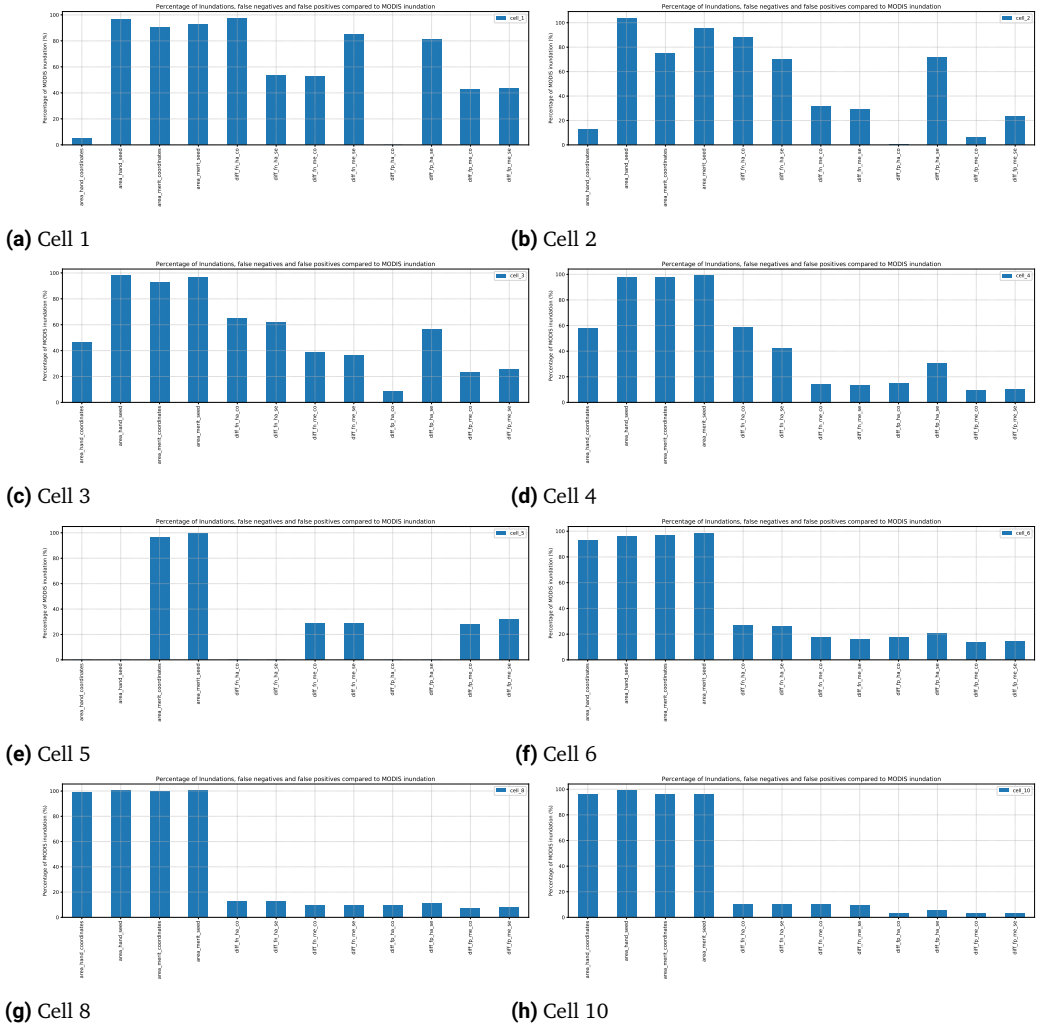

(a) Cell 1 **(b)** Cell 2

(c) Cell 3 **(d)** Cell 4

(e) Cell 5 **(f)** Cell 6

(g) Cell 8 **(h)** Cell 10

Figure E.10. Mapping errors relative to MODIS optical imagery (own work)

Impact

F

F.1 EM-DAT Flood Record

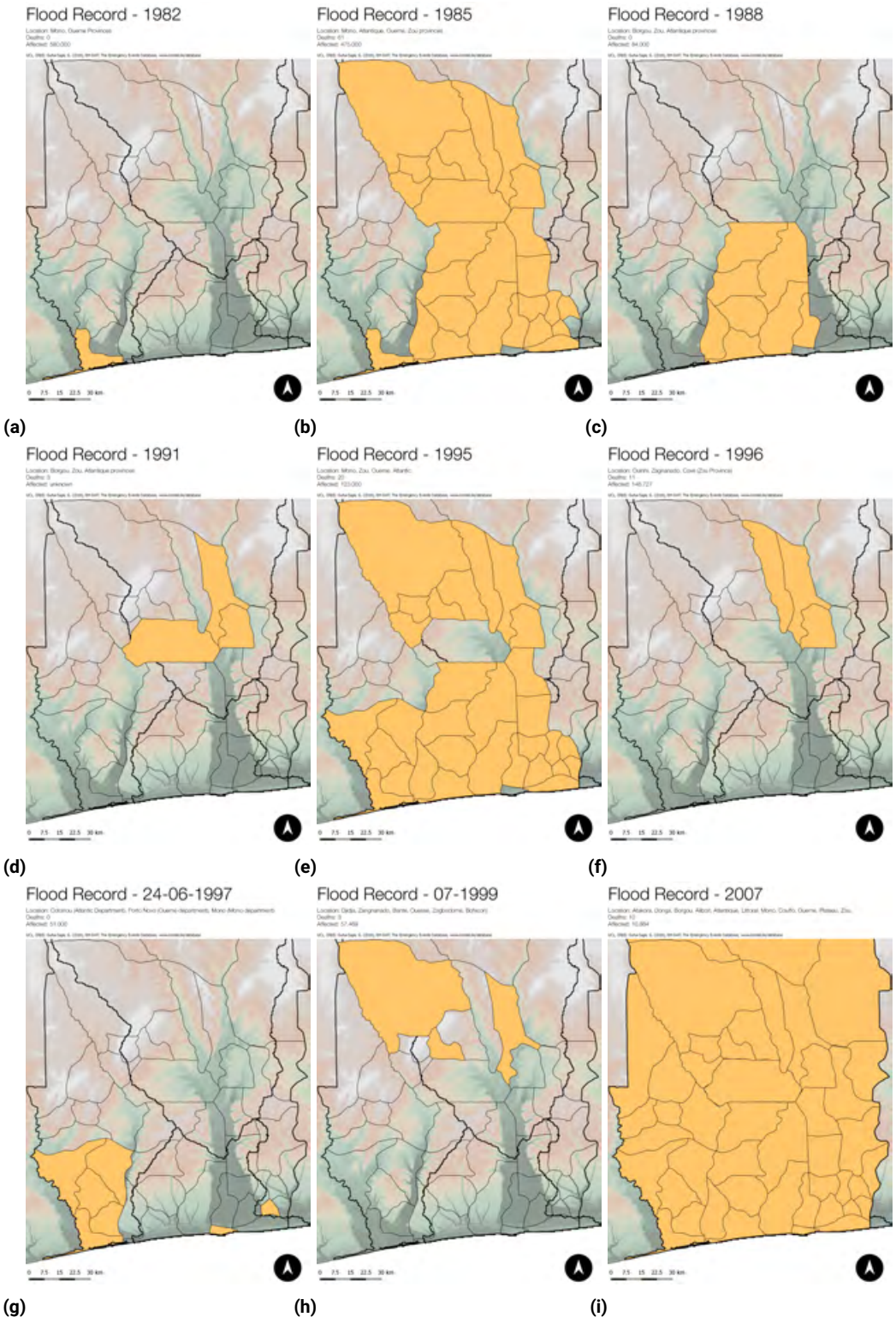

Figure F.1. Visualisation of EM-DAT registered flood events since 1970 Universite catholoique de Louvain (UCL) et al., 2018

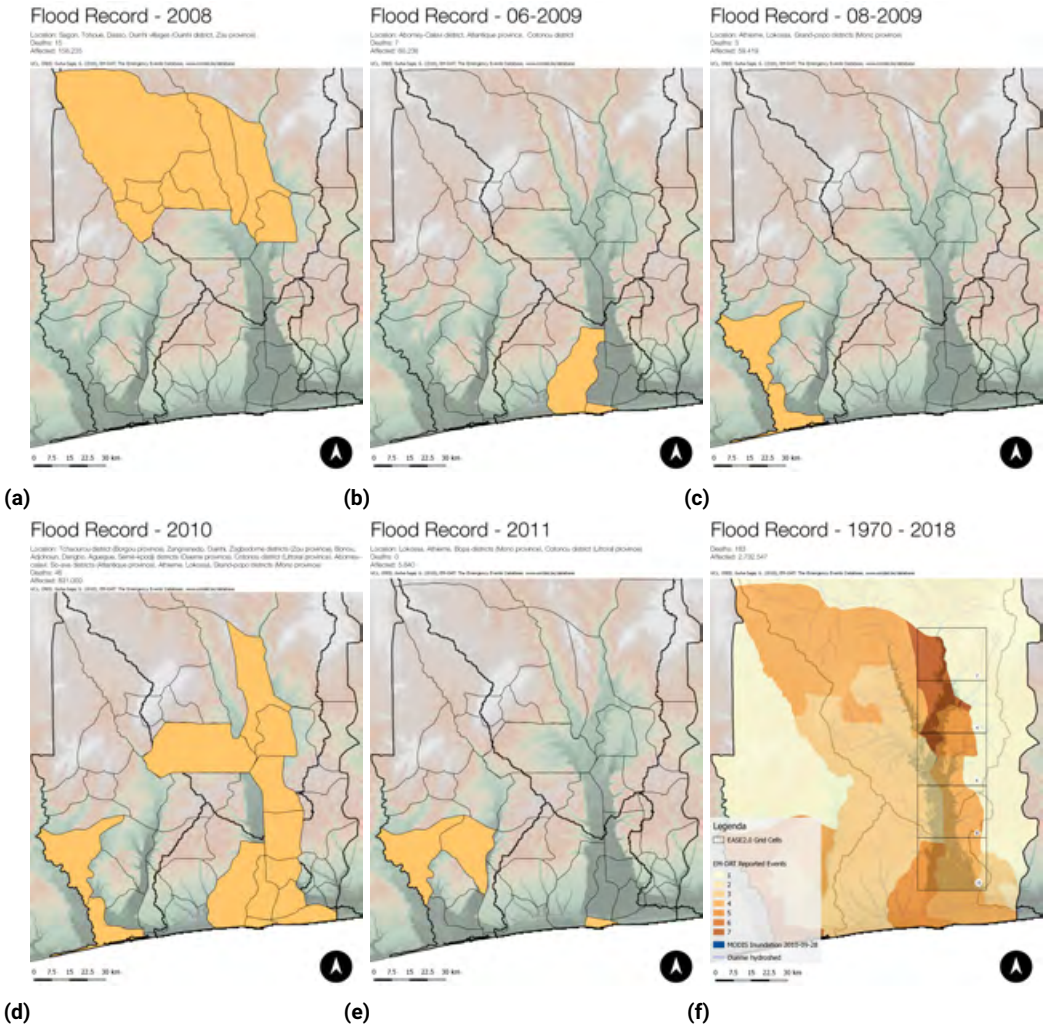

Figure F.2. Visualisation of EM-DAT registered flood events since 1970 Universite catholoique de Louvain (UCL) et al., 2018

F.2 Impact 2010 Flood

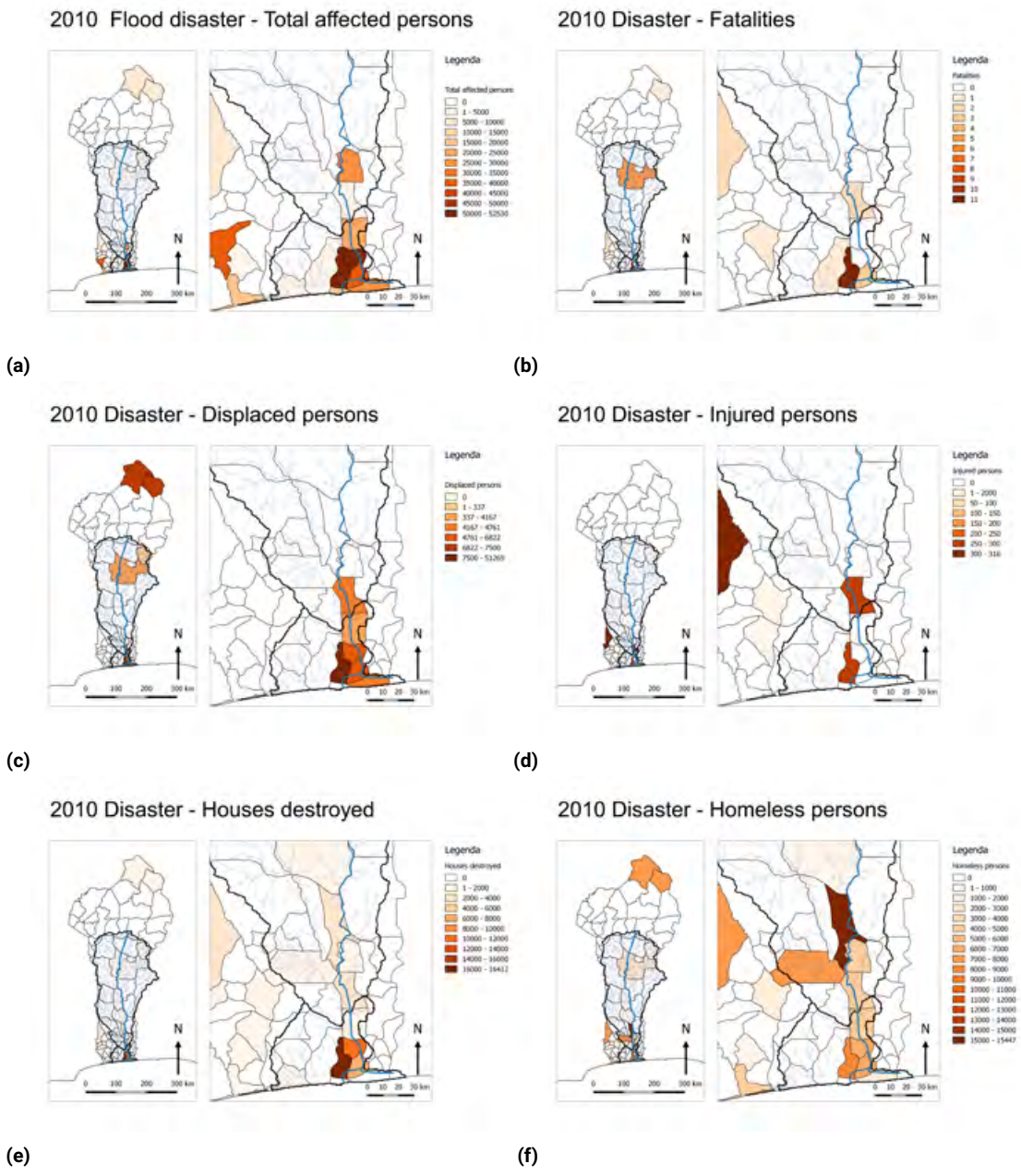

Figure F.3. Spatial visualisation of the reported impact for the 2010 disaster Universite catholoique de Louvain (UCL) et al., 2018

W.W.J. Neisingh
20-12-2018